

AD-A239 928



WRDC-TR-90-2121
Volume I



Thermal Energy Storage and
Heat Transfer Support Program

TASK-1 HEAT TRANSPORT SYSTEM STUDY
COPPER-WATER AND STEEL-SODIUM DWAHP

R. Ponnappan

UES, Inc.
4401 Dayton-Xenia Road
Dayton, Ohio 45432-1894

1 March 1991

Final Report for period June 1987 - September 1990

Approved for Public Release; Distribution Unlimited.

DTIC
SELECTED
AUG 29 1991
S B D

Aero Propulsion and Power Laboratory
Wright Laboratory
Air Force Systems Command
Wright-Patterson AFB, OH 45433-6563

91-08990



91

21

NOTICE

WHEN GOVERNMENT DRAWINGS, SPECIFICATIONS, OR OTHER DATA ARE USED FOR ANY PURPOSE OTHER THAN IN CONNECTION WITH A DEFINITELY GOVERNMENT-RELATED PROCUREMENT, THE UNITED STATES GOVERNMENT INCURS NO RESPONSIBILITY OR ANY OBLIGATION WHATSOEVER. THE FACT THAT THE GOVERNMENT MAY HAVE FORMULATED OR IN ANY WAY SUPPLIED THE SAID DRAWINGS, SPECIFICATIONS, OR OTHER DATA, IS NOT TO BE REGARDED BY IMPLICATION, OR OTHERWISE IN ANY MANNER CONSTRUED, AS LICENSING THE HOLDER, OR ANY OTHER PERSON OR CORPORATION; OR AS CONVEYING ANY RIGHTS OR PERMISSION TO MANUFACTURE, USE, OR SELL ANY PATENTED INVENTION THAT MAY IN ANY WAY BE RELATED THERETO.

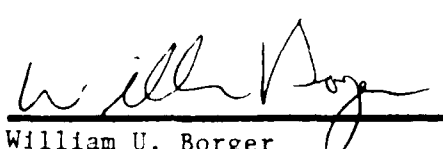
THIS REPORT HAS BEEN REVIEWED BY THE OFFICE OF PUBLIC AFFAIRS (ASD/PA) AND IS RELEASABLE TO THE NATIONAL TECHNICAL INFORMATION SERVICE (NTIS). AT NTIS IT WILL BE AVAILABLE TO THE GENERAL PUBLIC INCLUDING FOREIGN NATIONS.

THIS TECHNICAL REPORT HAS BEEN REVIEWED AND IS APPROVED FOR PUBLICATION.


ANGEL S. REYES
Power Technology Branch
Aerospace Power Division
Aero Propulsion and Power Directorate

FOR THE COMMANDER


JERRY E. BEAM
Power Technology Branch
Aerospace Power Division
Aero Propulsion and Power Directorate


William U. Borger
Chief, Aerospace Power Division
Aero Propulsion and Power Directorate

IF YOUR ADDRESS HAS CHANGED, IF YOU WISH TO BE REMOVED FROM OUR MAILING LIST, OR IF THE ADDRESSEE IS NO LONGER EMPLOYED BY YOUR ORGANIZATION PLEASE NOTIFY WL/POQS-3, WRIGHT-PATTERSON AFB, OH 45433-6563 TO HELP MAINTAIN A CURRENT MAILING LIST.

COPIES OF THIS REPORT SHOULD NOT BE RETURNED UNLESS RETURN IS REQUIRED BY SECURITY CONSIDERATIONS, CONTRACTUAL OBLIGATIONS, OR NOTICE ON A SPECIFIC DOCUMENT.

UNCLASSIFIED

SECURITY CLASSIFICATION OF THIS PAGE

REPORT DOCUMENTATION PAGE

1a. REPORT SECURITY CLASSIFICATION UNCLASSIFIED		1b. RESTRICTIVE MARKINGS N/A	
2a. SECURITY CLASSIFICATION AUTHORITY N/A		3. DISTRIBUTION / AVAILABILITY OF REPORT Approved for public release; Distribution is unlimited	
2b. DECLASSIFICATION / DOWNGRADING SCHEDULE			
4. PERFORMING ORGANIZATION REPORT NUMBER(S) UES-799-TR-90-001		5. MONITORING ORGANIZATION REPORT NUMBER(S) WRDC-TR-90-2121 Volume I	
6a. NAME OF PERFORMING ORGANIZATION UES, Inc.	6b. OFFICE SYMBOL (if applicable) SSED	7a. NAME OF MONITORING ORGANIZATION Aero Propulsion & Power Lab (WL/POOS) Wright Laboratory	
6c. ADDRESS (City, State, and ZIP Code) 4401 Dayton-Xenia Road Dayton, OH 45432-1894		7b. ADDRESS (City, State, and ZIP Code) Wright-Patterson AFB, OH 45433-6563	
8a. NAME OF FUNDING / SPONSORING ORGANIZATION	8b. OFFICE SYMBOL (if applicable)	9. PROCUREMENT INSTRUMENT IDENTIFICATION NUMBER F33615-87-C-2738	
8c. ADDRESS (City, State, and ZIP Code)		10. SOURCE OF FUNDING NUMBERS	
		PROGRAM ELEMENT NO 62203F	PROJECT NO. 3145
		TASK NO. 20	WORK UNIT ACCESSION NO 51
11. TITLE (Include Security Classification) Thermal Energy Storage and Heat Transfer Support Program Vol. I: Task - 1 Heat Transport System Study Copper-Water and Steel-Sodium DWAHP			
12. PERSONAL AUTHOR(S) Rengasamy Ponnappan			
13a. TYPE OF REPORT Final	13b. TIME COVERED FROM 29 Jun 87 TO 30 Sep 90	14. DATE OF REPORT (Year, Month, Day) 1991 March 1	15. PAGE COUNT 138
16. SUPPLEMENTARY NOTATION This document supplements WRDC-TR-89-2046 June 1989			
17. COSATI CODES		18. SUBJECT TERMS (Continue on reverse if necessary and identify by block number)	
FIELD	GROUP	Critical Heat Flux, Double Wall Artery, Effective Thermal Conductivity, Film Boiling, Heat Choke, Ethylene Glycol Cooling Sodium, High Temperature, Frozen Startup, Gas-loaded	
		Mode, Graphite Heater, Vacuum Chamber.	
19. ABSTRACT (Continue on reverse if necessary and identify by block number)			
<p>This report covers the test results of some extended research conducted on both 2m copper-water double wall artery heat pipe and 2m stainless steel-sodium heat pipe. The experimental results of the effective thermal conductivity of the wick agree with the predicted results. It is shown that the double wall wick is a "boiling-tolerant" wick and it can support high radial heat flux.</p> <p>The 2m sodium-SS 304 heat pipe was successfully tested using a pyrolytic graphite heater after facing several failures with nichrome and cartridge type heaters. Inert gas-filled mode and conventional mode startup tests were conducted. The startup from frozen state was smooth in gas-filled mode whereas similar startup attempt was rough in the conventional mode. Calorimetric measurement of heat losses and tilt test results are also presented.</p>			
20. DISTRIBUTION / AVAILABILITY OF ABSTRACT <input checked="" type="checkbox"/> UNCLASSIFIED/UNLIMITED <input type="checkbox"/> SAME AS RPT. <input type="checkbox"/> DTIC USERS		21. ABSTRACT SECURITY CLASSIFICATION UNCLASSIFIED	
22a. NAME OF RESPONSIBLE INDIVIDUAL Angel S. Reyes		22b. TELEPHONE (Include Area Code) 513-255-2922	22c. OFFICE SYMBOL WL/POOS-3

TABLE OF CONTENTS

<u>SECTION</u>	<u>TITLE</u>	<u>PAGE</u>
I.	INTRODUCTION	1
1.1	Development of Copper-Water DWAHP	2
1.2	Startup Problems in Sodium DWAHP	2
II.	COPPER-WATER DWAHP: STUDY OF CRITICAL HEAT FLUX IN THE DWAHP EVAPORATOR	5
2.1	Problem Identification and Scope of the Study	5
2.2	An Analysis of the Evaporator Parameters	8
2.3	Experimental Work	19
2.4	Results and Discussion	24
2.5	Usefulness and Practical Significance	32
2.6	Conclusions and Recommendations	35
III.	LIQUID METAL DWAHP: ADDITIONAL TEST RESULTS OF GAS AND VACUUM MODE STARTUPS	38
3.1	Potential Use and the Problem Area	38
3.2	Theoretical Considerations on Gas Filling Limits	39
3.3	Experimental Work	40
3.4	Results and Discussions	51
	3.4.1 Transport Capacity	51
	3.4.2 Inactive Condenser Length	53
	3.4.3 Axial Temperature Profile	53

TABLE OF CONTENTS

<u>SECTION</u>	<u>TITLE</u>	<u>PAGE</u>
3.4.4	Temperature Gradient	57
3.4.5	Frozen Startup Behavior	59
3.4.6	Liquid Startup Behavior	80
3.4.7	Startup Failure	80
3.4.8	Transient Input Power and Evaporator Temperature Variation	80
3.4.9	Calorimetric Data	86
3.4.10	Tilt Test Results	100
3.4.11	Gas Calculation Data	100
3.5	Conclusions	104
IV.	CONCLUDING REMARKS AND FUTURE DIRECTIONS ..	106
	REFERENCES	108
	APPENDICES	
	A. Determination of the Pressure at the Closed End of a Long Tube When the Other End is Connected to a Vacuum Pump	A-1
	B. High Temperature Heater Details	B-1
	C. Zirconia Insulating Cylinders	C-1
	D. Program <u>Gas</u> Listing	D-1

DTIC
COPY
SPECIFIED
5

Accession For	
NTIS GRA&I	<input checked="" type="checkbox"/>
DTIC TAB	<input type="checkbox"/>
Unannounced	<input type="checkbox"/>
Justification	
By	
Distribution	
Availability Codes	
Dist	Avail and/or Special
A-1	

LIST OF FIGURES

<u>FIGURE</u>	<u>TITLE</u>	<u>PAGE</u>
1	Cross Section Indicating the Evaporator Geometry for the DWAHP	7
2	Evaporator Section Liquid/Vapor Flow Model	9
3	Heat Transfer at the Evaporator Exit in the DWAHP	13
4	Various Heater Configurations and Corresponding Maximum Heat Fluxes	21
5	Thermocouple Locations and Corresponding Temperatures on the Circumference of the Heat Pipe for the 1800-W Steady-State Test	23
6	Axial Temperature Profiles for the Lean Wick Characterization	25
7	Axial Temperature Profiles for the 2-m DWAHP with a Direct Contact 0.127-m Heater	26
8	Axial Temperature Profiles for the 2-m DWAHP with a 0.254-m Heater on a 0.254-m Heat Choke	27
9	Axial Temperature Profiles for the 2-m DWAHP with a 0.127-m Heater on a 0.254-m Heat Choke	28
10	Transient Temperature Profiles Characterizing Dryout with a Direct Contact Heater	30
11	Transient Temperature Profiles Characterizing Dryout with an Indirect Contact Heater	31
12	Variation of Average Effective Wick Thermal Conductivity with Heat Input for Two Heater Configurations	33
13(a)	Gas-Blocked Length as a Function of Initial Gas Charge Pressure for Potassium Heat Pipes	41

LIST OF FIGURES

<u>FIGURE</u>	<u>TITLE</u>	<u>PAGE</u>
13(b)	Gas-Blocked Length as a Function of Initial Gas Charge Pressure for Sodium Heat Pipes	42
13(c)	Gas-Blocked Length as a Function of Initial Gas Charge Pressure for Lithium Heat Pipes	43
14	Cross-Section View of the Liquid Metal DWAHP	44
15	Longitudinal Section View of the Liquid Metal DWAHP	45
16	Noncondensable Gas Charging and Pressure Measurement Schematic Diagram	47
17	Radiation Shield and Thermocouple Location Details	49
18	High Temperature "Run-Away" Protection Circuit	50
19	Predicted and Experimental Performances (Q_o vs T_H)	52
20	Steady-State Inactive Condenser Length for Different Test Conditions	54
21	Steady-State Axial Temperature Profile (Vacuum Mode)	55
22	Steady-State Axial Temperature Profile (Gas-Filled Mode)	56
23	Average Hot Zone Temperature and Temperature Gradient	58
24	Axial Temperature Profile at Specified Time from 0-150 Minutes After Power Input ($Q_i = 600$ W; Vacuum Mode)	60
25	Transient Temperature Profile at Specified Axial Locations ($Q_i = 600$ W; Vacuum Mode)	61
26	Axial Temperature Profile at Specified Time from 0-150 Minutes After Power Input ($Q_i = 600$ W; Gas-Filled Mode)	62

LIST OF FIGURES

<u>FIGURE</u>	<u>TITLE</u>	<u>PAGE</u>
27	Transient Temperature Profile at Specified Axial Locations ($Q_i = 600$ W; Gas-Filled Mode)	63
28	Axial Temperature Profile at Specified Time from 0-150 Minutes After Power Input ($Q_i = 700$ W; Vacuum Mode)	64
29	Transient Temperature Profile at Specified Axial Locations ($Q_i = 700$ W; Vacuum Mode)	65
30	Axial Temperature Profile at Specified Time from 0-150 Minutes After Power Input ($Q_i = 700$ W; Gas-Filled Mode)	66
31	Transient Temperature Profile at Specified Axial Locations ($Q_i = 700$ W; Gas-Filled Mode)	67
32	Axial Temperature Profile at Specified Time from 0-150 Minutes After Power Input ($Q_i = 800$ W; Vacuum Mode)	68
33	Transient Temperature Profile at Specified Axial Locations ($Q_i = 800$ W; Vacuum Mode)	69
34	Axial Temperature Profile at Specified Time from 0-150 Minutes After Power Input ($Q_i = 800$ W; Gas-Filled Mode)	70
35	Transient Temperature Profile at Specified Axial Locations ($Q_i = 800$ W; Gas-Filled Mode)	71
36	Axial Temperature Profile at Specified Time from 0-150 Minutes After Power Input ($Q_i = 900$ W; Vacuum Mode)	72
37	Transient Temperature Profile at Specified Axial Locations ($Q_i = 900$ W; Vacuum Mode)	73
38	Axial Temperature Profile at Specified Time from 0-150 Minutes After Power Input ($Q_i = 900$ W; Gas-Filled Mode)	74
39	Transient Temperature Profile at Specified Axial Locations ($Q_i = 900$ W; Gas-Filled Mode)	75

LIST OF FIGURES

<u>FIGURE</u>	<u>TITLE</u>	<u>PAGE</u>
40	Axial Temperature Profile at Specified Time from 0-150 Minutes After Power Input ($Q_i = 1000$ W; Vacuum Mode) . . .	76
41	Transient Temperature Profile at Specified Axial Locations ($Q_i = 1000$ W; Vacuum Mode)	77
42	Axial Temperature Profile at Specified Time from 0-150 Minutes After Power Input ($Q_i = 1000$ W; Gas-Filled Mode) .	78
43	Transient Temperature Profile at Specified Axial Locations ($Q_i = 1000$ W; Gas-Filled Mode)	79
44	Axial Temperature Profile at Specified Time From 0-150 Minutes After Power Input ($Q_i = 1200$ W; Vacuum Mode; Liquid Startup)	81
45	Transient Temperature Profile at Specified Axial Locations ($Q_i = 1200$ W; Vacuum Mode; Liquid Startup)	82
46	Axial Temperature Profile at Specified Time From 0-150 Minutes After Power Input ($Q_i = 1200$ W; Gas-Filled Mode; Liquid Startup)	83
47	Transient Temperature Profile at Specified Axial Locations ($Q_i = 1200$ W; Gas-Filled Mode; Liquid Startup)	84
48	Evaporator and Heater Temperature "Run-Away" Condition During 1200-W Input (Vacuum and Gas-Filled Modes)	85
49	Transient Input Power and Evaporator Temperature Variations ($Q_i = 600$ W; Vacuum Mode)	89
50	Transient Input Power and Evaporator Temperature Variations ($Q_i = 600$ W; Gas-Filled Mode)	90
51	Transient Input Power and Evaporator Temperature Variations ($Q_i = 700$ W; Vacuum Mode)	91

LIST OF FIGURES

<u>FIGURE</u>	<u>TITLE</u>	<u>PAGE</u>
52	Transient Input Power and Evaporator Temperature Variations ($Q_i = 700$ W; Gas-Filled Mode)	92
53	Transient Input Power and Evaporator Temperature Variations ($Q_i = 800$ W; Vacuum Mode)	93
54	Transient Input Power and Evaporator Temperature Variations ($Q_i = 800$ W; Gas-Filled Mode)	94
55	Transient Input Power and Evaporator Temperature Variations ($Q_i = 900$ W; Vacuum Mode)	95
56	Transient Input Power and Evaporator Temperature Variations ($Q_i = 900$ W; Gas-Filled Mode)	96
57	Transient Input Power and Evaporator Temperature Variations ($Q_i = 1000$ W; Vacuum Mode)	97
58	Transient Input Power and Evaporator Temperature Variations ($Q_i = 1000$ W; Gas-Filled Mode)	98
59	Steady-State Calorimetric Test Data	99
60	Adverse Tilt Test Results	103

LIST OF TABLES

<u>TABLE</u>	<u>TITLE</u>	<u>PAGE</u>
1	Identification and Utilization Summary of the Copper-Water DWAHPs	4
2	Details of the Various Terms in the Equation for Capillary Wicking Limit Evaluation	18
3	Critical Heat Input Based on Capillary Limitation and Porosity for Liquid Flow	20
4	Vacuum-Mode Steady-State Test Results	87
5	Steady-State Test Results (Gas Loaded Mode $P_1 = 2.00$ torr Argon) Reprocessed Pipe	88
6	Steady-State Tilt Test Results (2.0 Torr Gas Filled Mode)	101
7	Gas Inventory in LMFP as Computed by Program GAS	102

FOREWORD

This final technical report was prepared as part of the contract deliverables under the "Thermal Energy Storage and Heat Transfer Support Program," contract F33615-87-C-2738. This contract was administered by the Aero Propulsion and Power Laboratory (APPL) of Wright Research and Development Center (WRDC) (now Wright Laboratory (WL)) and co-sponsored by the Strategic Defense Initiative Organization (SDIO). Dr. J. E. Bean, Ms. J. E. Johnson, Mr. M. Morgan, and Mr. A. S. Reyes were the Air Force Technical Monitors at various stages of this program.

The present report outlines the research effort performed under Task-1 Heat Transport System Study covering the specific work done on copper water and stainless steel-sodium double wall artery heat pipes. The other tasks of this program, namely, Task-2 Thermal Energy Storage Study, Task-3 Innovative Radiator Study, Task-4 Thermionics Study, and Task-5 Heat Pipe Life Test Study are covered under separate documents.

The entire work described here was performed on-site at the Thermal Laboratory (WL/POOS-3) by UES, INC., Dayton, Ohio with Dr. R. Ponnappan as the Task Principal Investigator and Program Manager. Messrs. J. Tennant (UES), M. D. Ryan (UES), and D. Reinmuller (WL) provided the technical support. UES Scientific and Engineering Services Division and Drafting Group provided documentation services.

List of Applicable Documents

The following research publications and technical reports were generated just prior to or during the course of the present research effort. The materials contained in these documents are supplemental to the present report and are to be referred as necessary.

1. R.Ponnappan and M.L. Ramalingam, Two Meter Modified Double Wall Artery Heat Pipe, Final Report for Period October 1983 - September 1986, UES-727-TR-87-001, June 1987.
2. R.Ponnappan, M.L. Ramalingam, J.E. Johnson, and E.T. Mahefkey, "Evaporator Critical Heat Flux in the Double Wall Artery Heat Pipe," Experimental Thermal and Fluid Science, Intl. J. of Experimental Heat Transfer, Thermodynamics and Fluid Mechanics, Vol. 2, No. 4, October 1989, pp. 450-464.
3. R.Ponnappan, Studies on the Startup Transients and Performance of a Gas Loaded Sodium Heat Pipe, Technical Report for Period June 1987 - November 1988, WRDC-TR-89-2046, June 1989.
4. R.Ponnappan, General Test Plan and Procedure for the 2m Sodium-Stainless Steel DWAHP, UES-TR-88-001, August 1988.

NOMENCLATURE

A	Surface area	m^2
B	Thickness of wick across the direction of fluid flow	m
d	Diameter	m
F_p, F_v	Friction factors; as defined by Chi [5]	$N/m^2 / (W m)$
g	Gravitational acceleration	m/s^2
H	Capillary height	m
k	Thermal conductivity	$W/(m K)$
K	Permeability of wick	m^2
L	Length	m
L_g	Noncondensable gas-blocked length of the pipe	m
L_p	Total length of the heat pipe	m
P	Pressure	Pa
P_i	Initial gas charge pressure	N/m^2
P_v	Vapor pressure of working fluid	N/m^2
q	Heat flux	W/m^2
Q, Q_i, Q_{in}	Evaporator heat input (electric heater)	W
Q_o, Q_{out}	Condenser heat output (calorimeter)	W
r	Radius	m
R	Resistance to fluid flow	$N/(W m)$
T	Temperature	K
T_1	Reference temperature	K
T_c	Room temperature at the time of gas loading	K
T_H	Hot zone temperature	K
T_{H}	Average hot zone temperature	K
T_s	Sink temperature	K
ΔT_{EA}	Evaporator end (T.C. #3) to adiabatic (T.C. #7) temperature difference	K
v	Specific volume	m^3 / kg

Greek Symbols

α	Empirical exponent	Unitless
ϵ	Porosity (Section II)	Unitless
ϵ	Emissivity of condenser external surface (Section III)	Unitless
θ	Angle of inclination	radians
λ	Latent heat	J/kg
μ	Dynamic viscosity	N.s/m ²
ρ	Density	kg/m ³
σ	Surface tension	N/m

Subscripts

a,A	Adiabatic
ax	Axial
b	Boiling
c,C	Condenser
ca	Capillary
cm	Maximum capillary
crit	Critical
cu	Copper
e,E	Evaporator
eff	Effective
g	Groove
i	Inner
I	Inserts
k	Thermal conduction
l	Liquid
m	Mean
n	Nucleation
o	Outer

p	Wick pore
⊥	Perpendicular to pipe axis
pm	Maximum pumping
r	Radial
R	Reservoir
s	Solid
sat	Saturation
v	Vapor

SECTION I

INTRODUCTION

The double wall artery heat pipe (DWAHP) concept was invented in 1982 as a method of improving the transport capacity of heat pipes.¹ Initially the new wick design was evaluated by testing a 1.2m long copper-water proof-of-the-concept heat pipe. This heat pipe, with six layers of screen mesh wick sandwiched between the outer tube and the grooved and vented inner tube, transported 1600 Wm. This transport capacity was higher than the demonstrated capacities of other comparable wick designs such as slab, pedestal, tunnel, and spiral artery.¹⁻³ Even though the fabrication procedure for this double wall heat pipe was fairly simple and straightforward, the wrapping and insertion of the screen wick was slightly complicated. An improved version of the double wall wick was developed subsequently. The improved design eliminated the screen wick in the transport and condenser sections in order to reduce the liquid flow resistance. In addition, the inner tube had larger groove width for the transport length which in essence helped to increase the effective length of the heat pipe. A 2m long copper-water system of the improved design was fabricated and tested. Several unique performance improvement ideas such as capillary inserts, vented and unheated versions of the artery grooves, glass enveloped version, condenser external heat chokes, ethylene-glycol cooled condenser cooling blocks, unheated evaporator-end length, and evaporator external heat choke were investigated in three stages of this study.⁴⁻¹¹ The last item of the study, namely the evaporator characterization is described in Section II of this report.

Subsequent to the copper-water system study, the double wall heat pipe concept was extended to the liquid metal regime in order to exploit the advantages of entrainment-free transport section and subcooled evaporator artery. A 2m stainless-steel sodium heat pipe was designed, fabricated and tested. Initially, the gas-loaded mode frozen state startup was verified and a computer code (SODART) was validated. Additional tests were conducted to compare the frozen state startup of the gas loaded and the conventional modes. Section III of this report describes these additional test results.

1.1 DEVELOPMENT OF COPPER-WATER DWAHP

Every stage of the DWAHP development was challenging and intriguing. While the lean-evaporator behavior and the higher than the state-of-the-art transport capacity of the DWAHP were encouraging, the unattainability of the theoretical design maximum transport capacity was discouraging. Finding a suitable answer to the shortcoming of the experimental performance to that of the predicted still remains as an active area of research. But, however, a lot of improvements were done to the copper-water DWAHP system during various stages of this research. Table 1 shows the identification and utilization summary of the various DWAHP units built and tested. For example, the 2m version was created to increase the transport length, the glass enveloped version helped to identify the vapor back flow into the adiabatic artery and thereby the introduction of capillary inserts, and the ethylene-glycol coolant blocks eliminated the problem of condenser quenching due to water spray cooling.

Excepting the microgravity testing and life testing of the DWAHP copper-water system, a comprehensive research study has been accomplished. Eleven conference paper presentations, of which three were published as archival journal papers, and three final technical reports were generated.¹⁻¹⁶ The heat pump augmented water heat pipe space radiator and pulse power thermal management applications could use this technology in some form or the other.

1.2 STARTUP PROBLEMS IN SODIUM DWAHP

When starting up a heat pipe from a state with frozen working fluid and heat supplied only in the heating zone, destruction of the operation of the pipe can occur due to freezing out of the fluid from the evaporation zone to the condensation zone. The probability of freezing out of the working fluid increases for pipes with intense heat removal and also for pipes with a large ratio of length of condenser to heating zone. An increase in the intensity of heat removal has a negative influence on the startup process, while introduction of a small quantity of non-condensable gases has a positive effect. Also, it was noted that stepwise heating, supplying

power and then shutting it off with gradual increase in power and many repetition of these operations, could appreciably facilitate the startup. (Ivanovskii, Sorokin and Yagodkin [26] page 182)

The problem of startup from frozen state is compounded in the sodium DWAHP due to the long, and noncommunicating transport zone wick structure. The vapor and liquid flow passages are physically separated and the condensing vapor can flow into the artery only after the hot front moves to the entrance of the condenser section.

A separate technical report has been written on the theoretical model development for a gas-loaded liquid metal heat pipe (LMHP) and the experimental verification of the startup parameters. (Applicable documents No.3)

TABLE I

Identification and Utilization Summary of the Copper-Water DWAHPs
Built at the Thermal Laboratory, WRDC

Hardware Identification and Description	Test History	Disposition/Status
1 DWAHP 30cm Trial Sample with Pinched Fill Tube	<ul style="list-style-type: none"> • Wick Cleaning and Assembly Practice • End Cap Welding and Filling Demonstration Model • No Functional Test Done 	<ul style="list-style-type: none"> • Display Item • Can be used as a Demo
2 DWAHP 1.2m #1 First Functional Model of the New Concept of Wick Structure	<ul style="list-style-type: none"> • Complete Performance Tested at WRDC • 1600 Wm Transport • Sent to Washington State University and later to University of Dayton for Additional Testing 	<ul style="list-style-type: none"> • Slightly Damaged • Fill Valve Opened Accidentally • Can be used after Reprocessing
3 DWAHP 1.2m #2 Second Improved Unit Similar to #1	<ul style="list-style-type: none"> • Complete Performance Mapping at WRDC • 1653 Wm Transport • Wright State University Tested this with Finned Condenser 	<ul style="list-style-type: none"> • In Good Condition • Can be Used as is • No Apparent Problems
4 DWAHP 2m #1 Improved Design; Screenless Vented Transport Section	<ul style="list-style-type: none"> • All Performance Tests • 2100 Wm Transport 	<ul style="list-style-type: none"> • In Good Condition • Can be Used as is
5 Glass Enveloped Heat Pipe Inner Tubes of DWAHP 2m #2	<ul style="list-style-type: none"> • Flow Visualization Study • Helped to Observe Vapor Backflow into Artery • Capillary Insert Idea was Evolved 	<ul style="list-style-type: none"> • Dismantled and Inner Tube Used for Making DWAHP 2m #2
6 DWAHP 2m #2 Screenless Unvented Transport Section; Priming Enhancements Installed	<ul style="list-style-type: none"> • All Performance Tests • Ethylene Glycol Cooled External Condenser was Used • 2800 Wm Transport 	<ul style="list-style-type: none"> • Evaporator Burn-out • Totally Damaged • Adiabatic and Condenser Sections of Inner Tube may be Salvaged

SECTION II

COPPER-WATER DWAHP: STUDY OF CRITICAL HEAT FLUX IN THE DWAHP EVAPORATOR

2.1 PROBLEM IDENTIFICATION AND SCOPE OF THE STUDY

The fact that heat is transferred into a heat pipe through the liquid saturated evaporator wick gives rise to the so-called "boiling limit" on the heat pipe capacity. The composite nature of the Double Wall Artery Heat Pipe (DWAHP) wick structure makes the prediction of the evaporator superheat (ΔT_{crit}) and the critical radial heat flux (q_r) very difficult. The effective thermal conductivity of the wick, effective radius of critical nucleation cavity and the nucleation superheat which are important parameters for the double wall wick evaporator heat transfer, have been evaluated based on the available theoretical models. Empirical correlations are used to corroborate the experimental results of the 2 m DWAHP. A heat choke mounted on the evaporator made it possible to measure the evaporator external temperatures which were not measured in the previous tests. The high values of the measured evaporator wall temperatures are explainable with the assumption of a thin layer of vapor blanket at the inner heating surface. It has been observed that partial saturation of the wick (lean evaporator) causes the capillary limit to drop even though it may be good for efficient convective heat transfer through the wick. The 2-m-long copper-water heat pipe had a peak performance of 1850 W at $\sim 23 \text{ W/cm}^2$ with a horizontal orientation.

The Double Wall Artery Heat Pipe (DWAHP) is a high capacity design intended to transport large amounts of heat at near isothermal conditions. While heat transport through a long adiabatic length is not a major problem, it is very difficult to transfer heat energy across the walls of the heat pipe at the evaporator and condenser without substantial penalty of temperature drops. The problem is compounded due to the phase change occurring within the porous wick and the complex nature of liquid-vapor flow controlled by the capillary forces. The effectiveness of the evaporator wick design depends on the largest radial heat flux it can handle with the

smallest temperature drop. The double wall wick shown in Fig. 1 is noted for its counter current liquid-vapor flow model and the subcooled liquid channel design at the evaporator.¹² Two 1.2-m and three 2-m-long DWHP's were tested with essentially similar evaporator construction.^{7,13,15} The evaporators were heated by direct contact electrical resistance coil heating. Attempts to measure evaporator wall temperature failed since the heater always influenced the measurement.

Generally boiling is not tolerated in conventional heat pipe evaporator wicks because it leads to evaporator dry out. If the wick is designed to eliminate boiling, it will severely restrict the transport capacity of the heat pipe. The boiling limit (or the critical heat flux applied to the evaporator without causing boiling) depends on the radial effective thermal conductivity (k_{eff}) of the wick structure and the evaporator critical superheat (ΔT_{crit}). The latter is calculated to a reasonable accuracy from the knowledge of nucleation boiling theory. But a precise determination of k_{eff} is difficult which is further complicated by the high capacity wick designs (such as the present DWHP) wherein a composite wick of screen and groove with partial saturation is to be considered. In situ measurement of k_{eff} is very difficult because it requires mounting of thermocouples inside the hermetically sealed heat pipe. The available k_{eff} equations do not account for the effects of vapor generation within the wick and partial saturation.

The scope of the present work was to measure the evaporator temperature externally at various input heat fluxes and determine the k_{eff} indirectly and verify with empirical correlations available in the literature. Also it was the aim to determine the effect of partial saturation on the critical heat flux. The approach was to use one version of the 2m copper-water DWHP test setup for the experimental measurement and compare the results with those of the available theoretical or empirical relations. A heat choke was mounted externally on the evaporator to help evaporator temperature measurement. The radial heat flux was doubled (11.5 to 23 W/cm²) by reducing the heat input area by one-half.

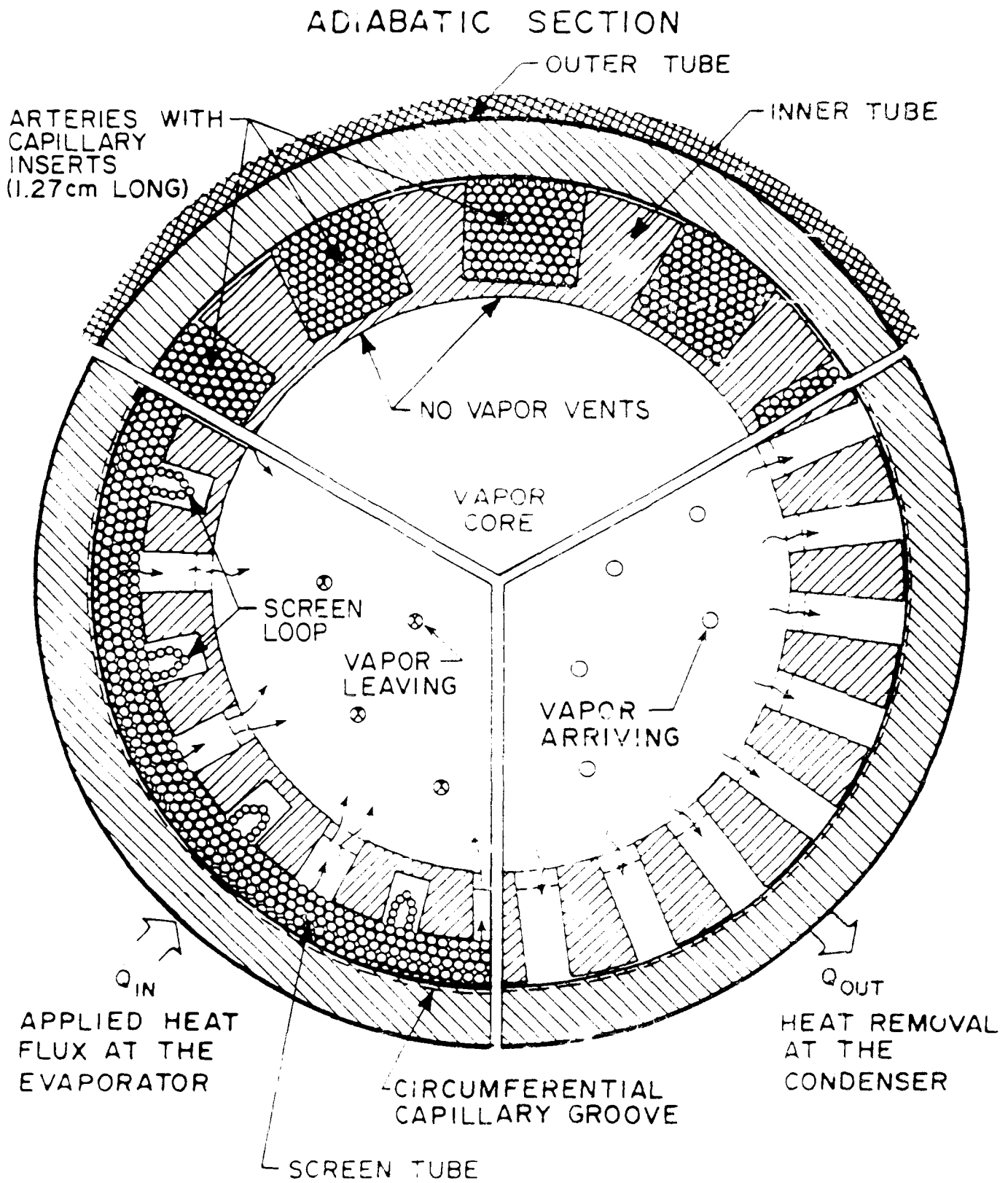


Figure 1. Cross Section Indicating the Evaporator Geometry for the DWHP.

2.2 ANALYSIS OF THE EVAPORATOR PARAMETERS

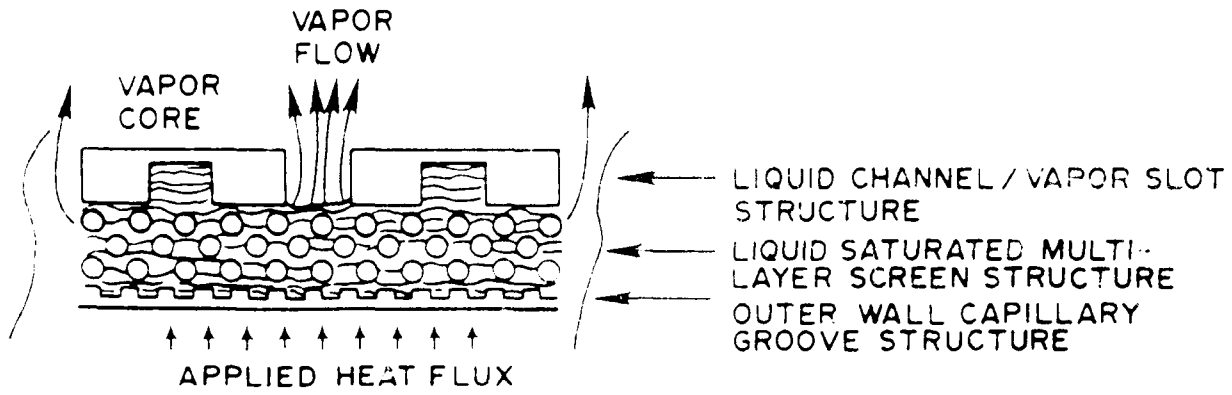
1. Evaporator Liquid/Vapor Flow Model: The evaporator liquid/vapor flow model of the DWHP is shown in Fig. 2. At low power inputs, surface evaporation without boiling occurs as in Fig. 2(A). When the heat input is increased, nucleation boiling starts at the heat pipe wall and the vapor flows through the unwetted screen making it partially saturated. This condition is shown in Fig. 2(B) and (C). The formation and motion of the vapor within the wick create the convective effects which form the dominant mechanism of heat transfer at the evaporator.

2. Effective Thermal Conductivity of the Wick (k_{eff}): The series-parallel model given in Chi¹⁷ for the thermal conductivity of fluid saturated porous metallic wick as given in Eq. (1) underpredicts the values for k_{eff} .

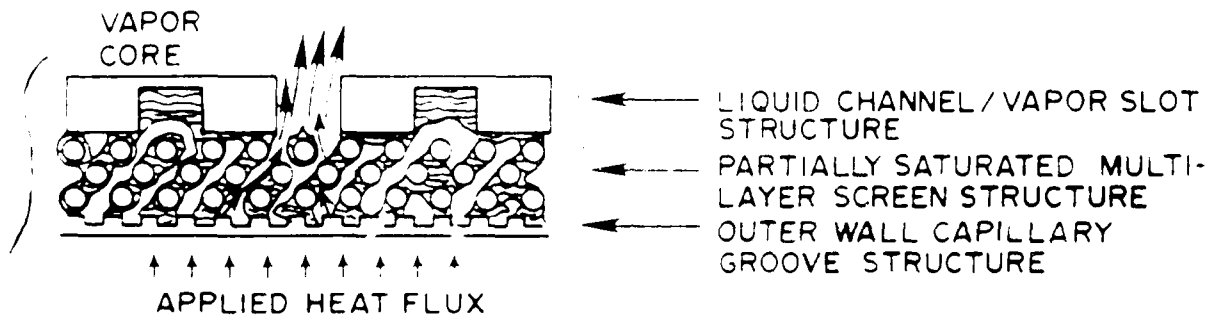
$$k_{eff} = \frac{k_f[(k_f + k_s) - (1 - \epsilon)(k_f - k_s)]}{[(k_f + k_s) + (1 - \epsilon)(k_f - k_s)]} \quad (1)$$

For water saturated copper screen of 40x40 cm⁻¹ mesh with wire diameter of 0.1143 mm, $k_f = 0.68$ W/m K, $k_s = 394.68$ W/m K and porosity of 62.89%, $k_{eff} = 1.477$ W/m K at 160°C. This low value of k_{eff} does not explain the relatively high experimental radial heat flux of 23 W/cm² demonstrated in the DWHP tests.

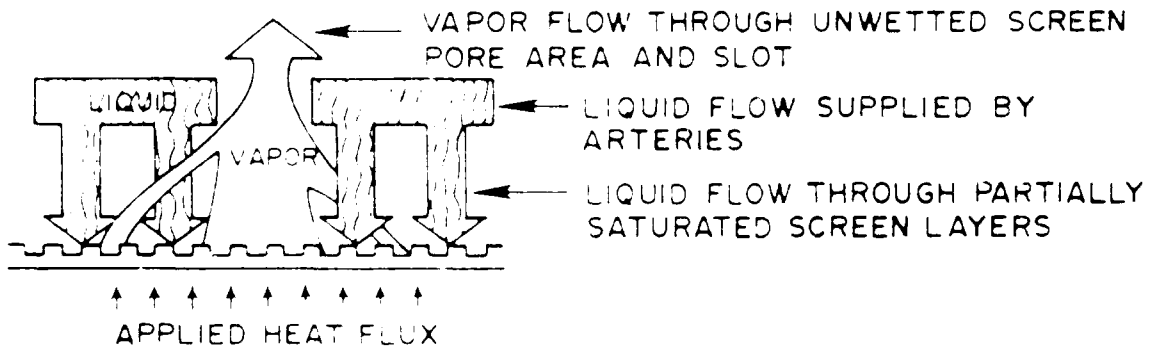
Phillips, et al.¹⁸ proposed a new model called "mean gap model" which accounts for three-dimensional effects and layer-to-layer contact. For the above wick assuming a packing number of 1.0, this model predicts $k_{eff} = 1.673$ W/m K which is only 13 percent more than the series-parallel model. Both series-parallel and mean gap models are applicable only to the 100% saturated wick shown in Fig. 2(A).



A. SATURATED WICK-ARTERY MODEL SCHEMATIC



B. LEAN WICK MODEL SCHEMATIC



C. COUNTER CURRENT LIQUID-VAPOR FLOW

Figure 2. Evaporator Section Liquid/Vapor Flow Model.

Alexander¹⁹ proposes an empirical relation based on the experimental data for water saturated metallic wicks in the form of Eq. (2). There is no physical rationale available for this relation except the fact that it has the wick/fluid conductivity ratio and porosity factors.

$$k_{eff} = k_f \left[\frac{k_s}{k_f} \right]^{(1-\epsilon)^\alpha} \quad (2)$$

The exponent α is an empirical constant obtained by Alexander as 0.59 for layered cloth wicks. For the present wick, this model predicts $k_{eff} = 23.55$ W/m K at 160°C and does not change with temperature significantly. This is a surprisingly high value and deserved attention in the present analysis of the DWHP wick. Furthermore, it is based on experimental results.

Peterson and Fletcher²⁰ report experimental k_{eff} values of 40 and 55 W/m K in the range of 20-100°C for dry and wet 59 percent porous sintered copper powder wicks, respectively. These results cannot be compared with screen wick data since sintering improves the metallic contact which is expected to improve k_{eff} .

No other thermal conductivity model is available in the literature which includes the vapor generation and dynamics within the wick. Also important are the factors such as packing, saturation, and contact pressure to be built in k_{eff} .

3. Nucleation Radius (r_n): From the nucleation theory of Rohsenow and Bergles,²¹ the nucleation radius, r_n is given by

$$r_n = \left[\frac{2\sigma T_{sat} k_f (v_v - v_l)}{\lambda q_r} \right]^{0.5} \quad (3)$$

The DWAHP test results have shown q_e values from 0 to 23 W/cm² without wick dryout. Two representative cases of long and short evaporator heating arrangements which lead to a uniform heat flux of 11.22 W/cm² and a concentrated flux of 23.76 W/cm², respectively, are used here to obtain r_n at the corresponding operating temperature of 200°C.

$$r_n = 3.72 \times 10^{-6} \text{ m at } 11.22 \text{ W/cm}^2$$

$$r_n = 2.556 \times 10^{-6} \text{ m at } 23.76 \text{ W/cm}^2$$

These values are very small compared to the wick pore radius (r_p) of 1.27×10^{-4} m which will be the limiting r_n in case Eq. (3) predicted values larger than r_p .

4. Nucleation Superheat: Marcus²² has shown that the critical evaporator superheat (ΔT across the wick) is given by

$$\Delta T_{crit} = \frac{T_{sat}}{\lambda \rho_v} \left[\frac{2\sigma}{r_n} - \Delta P_{ca}^* \right] \quad (4)$$

where ΔP_{ca}^* is the maximum value of capillary head along the evaporator. Substituting the r_n values and the other property values, one obtains,

$$\Delta T_{crit} = 0.62 \text{ K for low heat flux}$$

$$\Delta T_{crit} = 0.91 \text{ K for high heat flux}$$

5. Critical Heat Flux: The nucleation superheat predicted above represents the maximum temperature difference sustainable across the evaporator wick without nucleate boiling within the wick. In certain composite wicks such as annular arteries and screen covered grooves, wick boiling clearly renders the heat pipe inoperative since the vapor cannot escape the wick.²² The boiling limit for such cases becomes the limit of conduction flux into the evaporator and is given for cylindrical heat pipes as

$$Q_b = \frac{2\pi L_e k_{eff} \Delta T_{crit}}{\ln(r_o/r_i)} \quad (5)$$

These Q_b limits are very low values and are over-conservative when compared to the present experimental result (1800 W). This means that the double wall wick does not dry out with the incipiency of boiling. Due to the provision of clear vapor venting arrangement and liquid feeding from inner side, boiling is tolerated within the screen layers.

6. Film Boiling: In order to verify the effect of vapor accumulation within the wick, a thin uniform layer of vapor blanket equal to a height of half screen wire diameter ($0.5 d_{wire}$) is assumed at the heating surface. The effective thermal conductivity of vapor and screen is found to be $k_{eff} = 0.0566$ W/m K using Eq. (1). From the experimental values of steady-state tests at 1700 W, a net radial heat rate of 1530 W goes through a vapor layer of 0.05715 mm over the evaporator length of 25.4 cm. These values are plugged into Eq. (5) and a radial temperature drop across the film is obtained as $\Delta T_{radial} = 103$ K. This clearly explains the very high evaporator average measured ΔT (of the order of 100 to 150 K as seen in the axial temperature profiles) at high heat inputs.

7. Axial Versus Radial Heat Conduction at the Evaporator Exit: Axial heat conduction through the wall and wick at the evaporator exit region where the capillary inserts are installed affects the vapor bubble generation, growth, and venting at the evaporator exit. The axial conduction together with the preheating of the return liquid by the counter-flowing vapor at the region where the artery channel interfaces (Fig. 3) with the evaporator determines whether the return liquid is subcooled or superheated. If superheating occurs, then bubble generation in the inserts is imminent.

The simple conduction relation given by Eq. (6) is used to calculate the heat flow through the insert lengths of 1.27 cm.

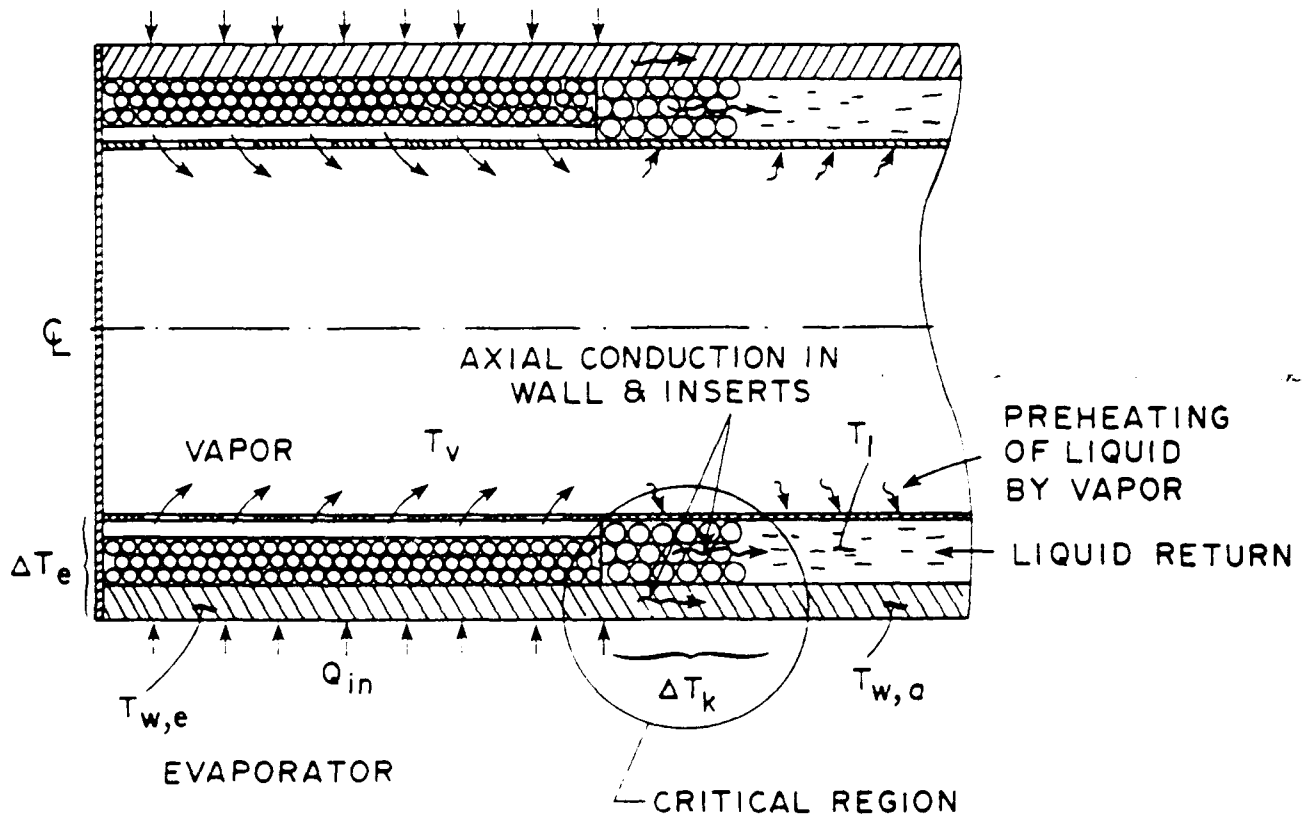


Figure 3. Heat Transfer at the Evaporator in the DWHP.

$$Q_{k,ax} = k_{eff,I} A_{ax} \left[\frac{\Delta T_{k,ax}}{\Delta L} \right] \quad (6)$$

The effective thermal conductivity of the wall at the liquid saturated inserts, $k_{eff,I}$ is computed based on the fact that the wall material and the inserts are in parallel.

$$k_{eff,I} = \epsilon_l k_l + (1 - \epsilon_l) k_{cu} \quad (7)$$

The liquid saturated screen conductivity k_l has been computed as 1.673 W/m K by the mean gap model.¹⁸ Substituting $k_{cu} = 304.08$ W/m K and $\epsilon_l = 26.04\%$ (porosity for liquid flow in the grooves at the insert region computed as A_g/A_d) $k_{eff,I}$ has been obtained as 292.33 W/m K. Now $Q_{k,ax}$ is obtained in terms of $\Delta T_{k,ax}$ as in Eq. (8),

$$Q_{k,ax} = 6.014 [\Delta T_{k,ax}] \quad (8)$$

$Q_{k,ax}$ cannot be computed without knowing $\Delta T_{k,ax}$. Experimental measurements are used to obtain this. A typical steady-state test temperature data showed a $\Delta T_{k,ax}$ of 3.3 K across the insert length at 1850 W input. Therefore, $Q_{k,ax}$ is only 1.2 percent of the axial heat transport rate through the vapor core. Another set of steady state data at 500 W revealed that the $\Delta T_{k,ax}$ was 1.4 K for the average operating temperature varying from 100 to 200°C and accounted for only ~2 percent of axial conduction.

On similar lines, the radial heat conduction, $Q_{k,r}$ can be obtained in terms of radial temperature difference across the wall and wick at the insert region, $\Delta T_{k,r}$, as given in Eq. (9) for comparison with $Q_{k,ax}$

$$Q_{k,r} = 42.76 [\Delta T_{k,r}] \quad (9)$$

It is evident from Eqs. (8) and (9) that the axial conduction is not significant compared to radial conduction. However, the radial conduction is also minimized by the adiabatic insulation. In actual heat pipe tests, it has been observed that the adiabatic vapor core and external wall temperatures are almost the same. $\Delta T_{k,r}$ is very small and it depends upon the small amount of heat loss through the insulation.

Hence, it can be concluded that neither the axial conduction nor the radial conduction at the evaporator exit (region of the inserts) poses a real threat of superheating the return liquid. However, it should be noted that the return liquid must be always subcooled. The minimum available temperature difference (subcooling) between the vapor core and the liquid channel for the present heat pipe is given in the next section.

8. Artery Subcooling: Since the liquid leaves the condenser at a subcooled temperature relative to the main vapor core temperature, the saturation pressure within the artery channel is less than the pressure in the vapor core. The pressure difference can be expressed by the Clausius-Clapeyron equation (Eq. (10)) which relates the temperature and pressure along the saturation line.²³

$$\Delta P = \frac{P_v \lambda}{RT_v^2} \Delta T \quad (10)$$

Here, R is the gas constant for water. This ΔP is equated to the capillary pressure head available for the given pumping wick of the water heat pipe and the corresponding ΔT are obtained at various vapor temperatures as listed below:

$T_v(^{\circ}\text{C})$:	20	60	100	127	160	200	254
$\Delta T(\text{K})$:	9.44	1.12	0.26	0.107	0.048	0.0198	0.0073

In an operating heat pipe, if the subcooling temperature differences (ΔT) are lower than the values given above, there will be a likelihood of bubble generation in the liquid channel. This

bubble may grow and eventually cause artery depriming. Therefore, it is re-emphasized that the return liquid to the evaporator must be in subcooled condition throughout the entire length of flow.

In the present experimental studies of the double wall artery heat pipe, these measurements could not be made as there were no internal thermocouples.

9. Partial Saturation in the Wick: The capillary wicking limit of planar heat pipe wicks as derived by Alexander¹⁹ is given by

$$q_{crit} = (Q/A)_{crit} = \frac{\frac{g}{g_c} \left[H_{ca}(T_1) \frac{\sigma}{\sigma(T_1)} \rho_l(T_1) - \rho_l L \sin(\theta) \right]}{\frac{L_e \mu_l}{\rho_l K_e \lambda B} \left[\frac{L_e}{2} + L_a \right]} \quad (11)$$

This expression does not account for the frictional pressure drop for vapor flow in the wick and assumes that the entire wick cross section is available for liquid flow. Actually, in our concept of a lean wick, there is certainly the possibility of vapor flow through the wick when it is partially saturated, giving rise to vapor friction forces that offer additional flow resistance consequently reducing the overpredicted values of critical heat flux.

Ferrel and Johnson²⁴ developed a better version of the equation by incorporating the resistance to vapor flow and modifying it to

$$q_{crit} = \frac{\frac{g}{g_c} \left[H_{ca}(T_1) \frac{\sigma}{\sigma(T_1)} \rho_l(T_1) - \rho_l (L_a + L_e) \sin(\theta) \right]}{L_e \left[\frac{\mu_l L_e}{2K_e \rho_l e_l B \lambda} + \frac{\mu_l L_a}{K_a \rho_l B \lambda} + \frac{\mu_v B}{K_e \rho_v (e - e_l) L_e \lambda} \right]} \quad (12)$$

In this equation, ϵ_l represents the porosity for liquid flow, that can be arbitrarily varied from zero to a maximum value equal to ϵ , the wick porosity. The portion of the wick volume, not occupied by liquid, is assumed to be filled with vapor. Here the wick is considered to have the same configuration along its length, and the condenser region is part of a liquid reservoir, unlike that of the DWHP where the wick structure is complicated by the composite nature of the double wall and the condenser is not exactly a part of any liquid reservoir.

A similar equation has been developed for the DWHP where all the resistances to liquid as well as vapor flow in the entire heat pipe have been considered while incorporating the concept of ϵ_l . In this equation, Q_{crit} is determined by an iterative method as the friction factor for vapor flow is expressed as a function of Q_{crit} . The revised equation for q_{crit} is written as

$$q_{crit} = \frac{(p_{pm}/2\pi L_e r_m)}{F_l L_{eff} + F_v L_{eff}} \quad (13)$$

where

$$P_{pm} = P_{cm} - \Delta P_l - \Delta P_{ax} \quad (14)$$

$$F_l L_{eff} = R_{l,s} + R_{v,s} + R_{l,g} + R_{l,l} + R_{l,a} + R_{l,c} \quad (15)$$

$$F_v L_{eff} = f(Q_{crit}) \quad (16)$$

F_l and F_v represent frictional factors for liquid flow and vapor flow respectively as explained in the heat pipe text.¹⁷

The expanded relations of each of these terms in Eq. (15) as functions of the geometry, the fluid/vapor properties, and the respective porosities are provided in Table 2.

TABLE 2. Details of the Various Terms in the Equation for Capillary Wicking Limit Evaluation

Term	Representation	Expanded Relation
1	P_{cm}	$(g/g_c) \rho_l H_{ca}(T)$
2	ΔP_{\perp}	$(g/g_c) \rho_l d_w \cos\theta$
3	ΔP_{ax}	$(g/g_c) \rho_l d_w \sin\theta$
4	R_{te}	$\frac{L_e}{4\pi r_m K_e B_e \epsilon_l} \frac{\mu_l}{\lambda \rho_v}$
5	$R_{v,e}$	$\frac{B_e}{2\pi r_m K_e L_e \epsilon_v} \frac{\mu_v}{\lambda \rho_v}$
6	$R_{t,B}$	$\frac{L_e}{4\pi r_m K_{eg} B_{eg}} \frac{\mu_l}{\lambda \rho_l}$
7	$R_{t,I}$	$\frac{L_l}{2\pi r_m K_l B_l} \frac{\mu_l}{\lambda \rho_l}$
8	$R_{t,a}$	$\frac{L_a}{2\pi r_m K_a B_a} \frac{\mu_l}{\lambda \rho_l}$

The critical heat input based on capillary limitation and porosities for liquid and vapor flow were evaluated according to Eq. (13) for various temperatures ranging from 20°C to 254°C. The resulting values are given in Table 3. The calculation details for the vapor friction factor, F_v , are explained in Reference [17]. When $\epsilon_1 = \epsilon$ (100% wick saturation), Eq. (15) is not used to calculate Q_{crit} since $R_{v,e}$ is not definable. Since no vapor is present, $R_{v,e}$ is assumed zero and Q_{crit} is calculated taking into account other R values. It should be noted from Table 3 that the Q_{crit} values decrease with the decrease in saturation ratios, and the present experimental values of heat input roughly lie in the range $\epsilon_1 = 0.4\epsilon$ to 0.2ϵ .

2.3 EXPERIMENTAL WORK

Double Wall Artery Heat Pipe: As indicated in the cross section of the 2-m copper-water DWAHP in Fig. 1, there were a total of 12 inserts, each 12.7 mm long, 2.38 mm wide, and 2.38 mm deep located at the evaporator, transport transition region. Screen loops 305 mm long were also positioned in the 12 evaporator grooves without vent slots. The inserts were introduced to prevent vapor back flow into the adiabatic arteries while the screen loops ensured radial liquid supply from the arteries to the screen wick in the evaporator section.⁷ The inserts were made from 24x24 cm⁻¹ copper screen and the screen loops in the evaporator grooves were made from 40x40 cm⁻¹ screen strips. There were no vent slots in the adiabatic section as the inserts were expected to eliminate the bubble movement into the adiabatic arteries.

Evaporator Heater Configurations: The DWAHP was tested with four different evaporator heater configurations in order to vary the heat flux and determine the maximum heat flux at which it would operate. As shown in Fig. 4, two of the configurations tested involved heat choke isothermalizers between the heating coil and the evaporator of the heat pipe. The heat choke is made of machined copper semi-cylindrical blocks (6 mm thick) mounted externally on the evaporator section of the heat pipe and bolted together tightly for good thermal contact with the heat pipe. The outer surface of the heat choke has circular grooves to fit the helically coiled heater. The heat choke was introduced with the intention of minimizing hot spots that might be

TABLE 3. Critical Heat Input Based on Capillary Limitation and Porosity for Liquid Flow

Temp. (°C)	Critical Heat Input, Q_{crit} (W)				
	$\epsilon_t = \epsilon$	$\epsilon_t = 0.8\epsilon$	$\epsilon_t = 0.6\epsilon$	$\epsilon_t = 0.4\epsilon$	$\epsilon_t = 0.2\epsilon$
20	737	648	606	525	356
60	2336	1866	1632	1282	741
100	3951	3982	2524	1905	1045
127	4894	3502	2930	2135	1143
160	5464	3762	3067	2215	1167
200	5317	3501	2803	1995	1037
254	4076	2593	2064	1455	751

responsible for the premature dryout of the heat pipe. This apparently minimizes the tendency to deplete certain arteries of the working fluid and also helps direct measurement of the evaporator wall temperature.

There were two configurations with direct contact between the heating coil and the heat pipe envelope material in the evaporator region of the heat pipe. The other two configurations had the heat choke separating the heating coil from the envelope material in the evaporator region of the heat pipe. It was found that even though the introduction of the heat choke did not improve the overall heat transport capability of the heat pipe, it certainly enhanced the tolerable heat flux limitation to 23.76 W/cm^2 . This revealed that the earlier dryout situation occurred for reasons other than heat flux limitations on the heat pipe. The performance results for each of the four configurations tested are also provided in Fig. 4.

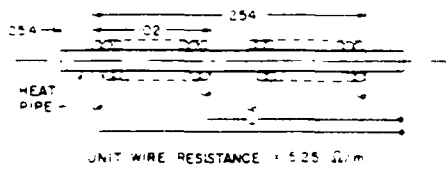
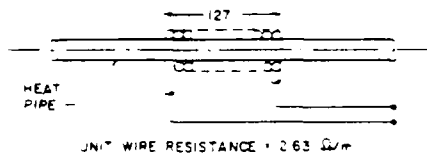
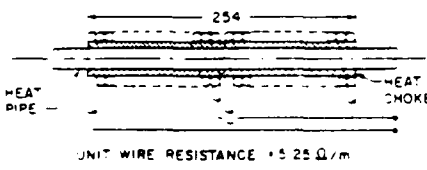
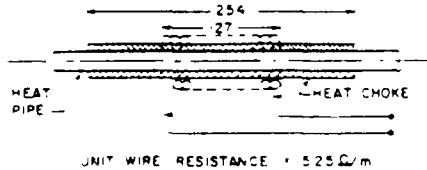
CONFIGURATION	HEATER LENGTH (cms)	MAXIMUM HEAT INPUT (W)	MAXIMUM HEAT FLUX (W/cm ²)
 <p>UNIT WIRE RESISTANCE = 5.25 Ω/m</p>	22.9	1850	13.56
 <p>UNIT WIRE RESISTANCE = 2.63 Ω/m</p>	12.4	1700	22.44
 <p>UNIT WIRE RESISTANCE = 5.25 Ω/m</p>	25.4	1700	11.22
 <p>UNIT WIRE RESISTANCE = 5.25 Ω/m</p>	12.7	1800	23.76

Figure 4. Various Heater Configurations and Corresponding Maximum Heat Fluxes.

Test Instrumentation and Procedure: A description of the various elements constituting the instrumentation of the DWAHP is provided in the paper on condenser quenching studies.²⁵ Several different heating configurations were used for the evaporator, as explained earlier. The calorimetric condenser with copper cooling jackets and Ethylene Glycol circulation was the cooling method used for the heat pipe testing. The heat pipe was mounted on an optical bench with leveling screws that could be adjusted to maintain a horizontal or inclined orientation. The entire heat pipe assembly was insulated with Fiberfrax insulation to minimize heat losses to the atmosphere. A total of thirty copper-constantan thermocouples were mounted all along the heat pipe to monitor the various temperatures. The unique feature of introducing the heat choke in the evaporator was that thermocouples could be mounted on the surface of the heat pipe, without being influenced by the heating coil.

As shown in Fig. 5, a schematic representation of the evaporator with the heat choke and a short heater, there were four peripheral thermocouples at each of the five axial locations. These thermocouples were mounted in this fashion to provide some information on the depletion of arteries at the time of dryout. In addition to these thermocouples, two thermocouples (#2 and #3) at the evaporator were used as sensing devices to shut off the power supply to the heater if the temperatures exceeded 220°C. These two temperatures were constantly monitored by an Apple computer system while the other thermocouples were connected to a datalogger.

Steady state performance tests were conducted with each heater configuration to determine the maximum heat transport capability. For each test, the heat pipe was allowed to warm up gradually by allowing it to attain steady state before increasing the heat input. Each test was initiated at 125 W and continued up to 750 W in incremental steps of 125 W. Thereafter, the steps were changed to 50 W up to 1600 W and eventually reduced to 25 W till dryout occurred.

Experimental Uncertainty: The power and temperature measurements are rather straightforward. Standard calibrated equipment were used for all measurements. The uncertainty in temperature measurement using copper-constantan thermocouples was $\pm 1.0^\circ\text{C}$ or $\pm 0.75\%$.

(whichever is greater) in 0-350°C. The uncertainty in electrical power measurement using analog type volt/ampere meters was $\pm 0.25\%$ in 0-2000 W.

2.4 RESULTS AND DISCUSSION

Figure 6 represents the axial temperature profiles at various operating temperatures for a heat input of 500 W. From the plots, it can be observed that the difference between the peak evaporator temperature and the average operating temperature decreases with increase in the operating temperature. This is typical of the lean evaporator wick where the motions of liquid and vapor are based on a counterflow model. As the operating temperature goes up, heat convection dominates due to the presence of vapor in the partially saturated lean evaporator wick. This tends to increase the overall effective thermal conductivity of the wick, consequently reducing the difference between the peak evaporator temperature and the average operating temperature for the same heat input.

Figures 7, 8, and 9 represent the steady-state axial temperature profiles for three different heater configurations on the evaporator. Comparison of the temperature profiles with and without the heat choke reveals the importance of being able to measure the actual temperature of the heat pipe evaporator without the influence of the heater. It was found that the evaporator temperatures at the center of the heater were as high as 200°C above the average adiabatic temperatures, for heat input values in excess of 1500 W. The reason for these high temperature differences in Figs. 8 and 9 can be explained by the presence of a very thin ($\sim 0.5 d_{wire}$) film of vapor at the envelope/screen wick interface that results as a consequence of film boiling at high values of heat input as illustrated by calculations given in the analysis section. This thin film can reduce the effective thermal conductivity of the vapor/screen combination to very low values (0.0566 W/m K), forcing the heat pipe to operate with large radial temperature gradients in the evaporator as the film thickness increased progressively with heat input.

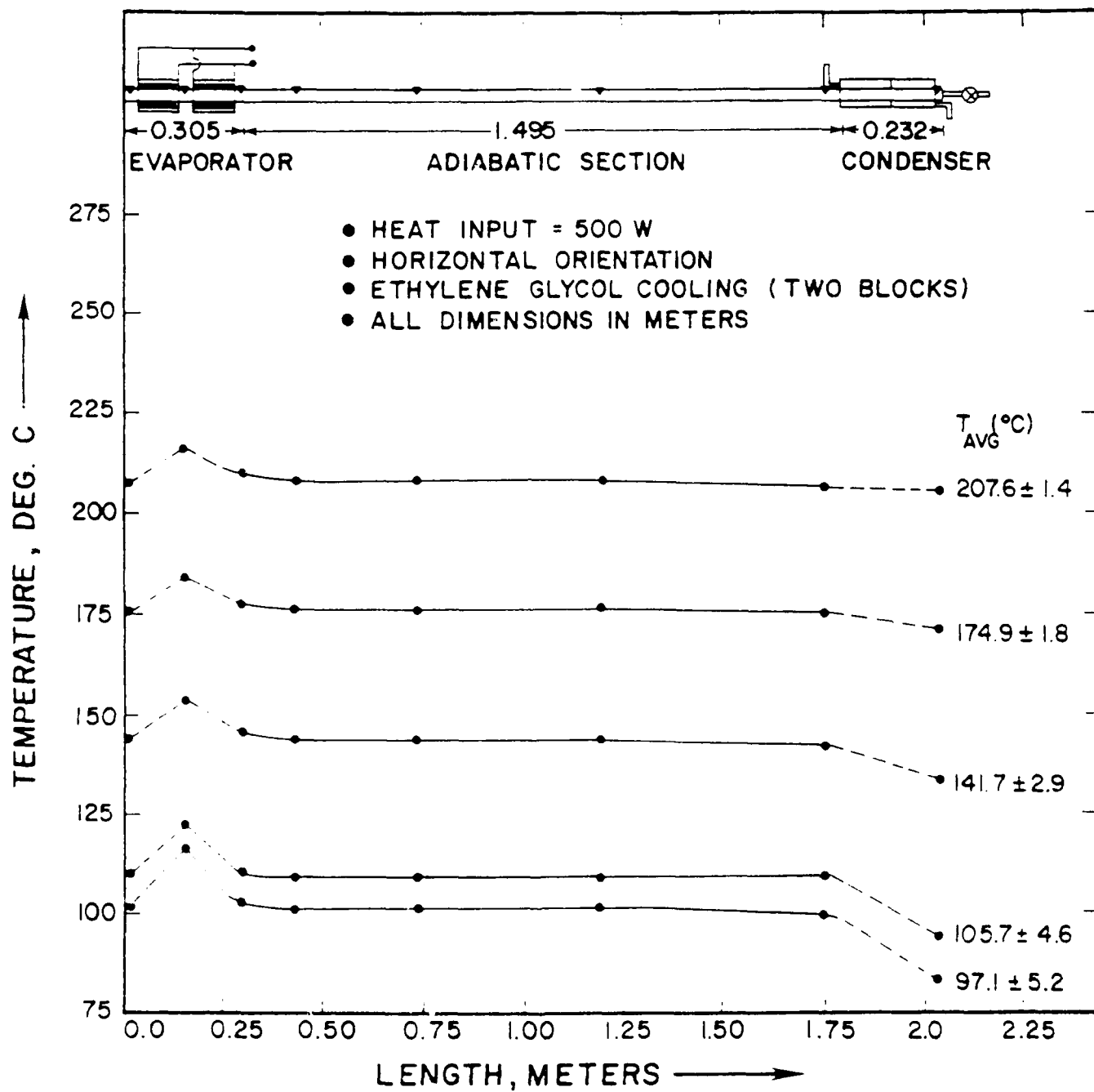


Figure 6. Axial Temperature Profiles for the Lean Wick Characterization.

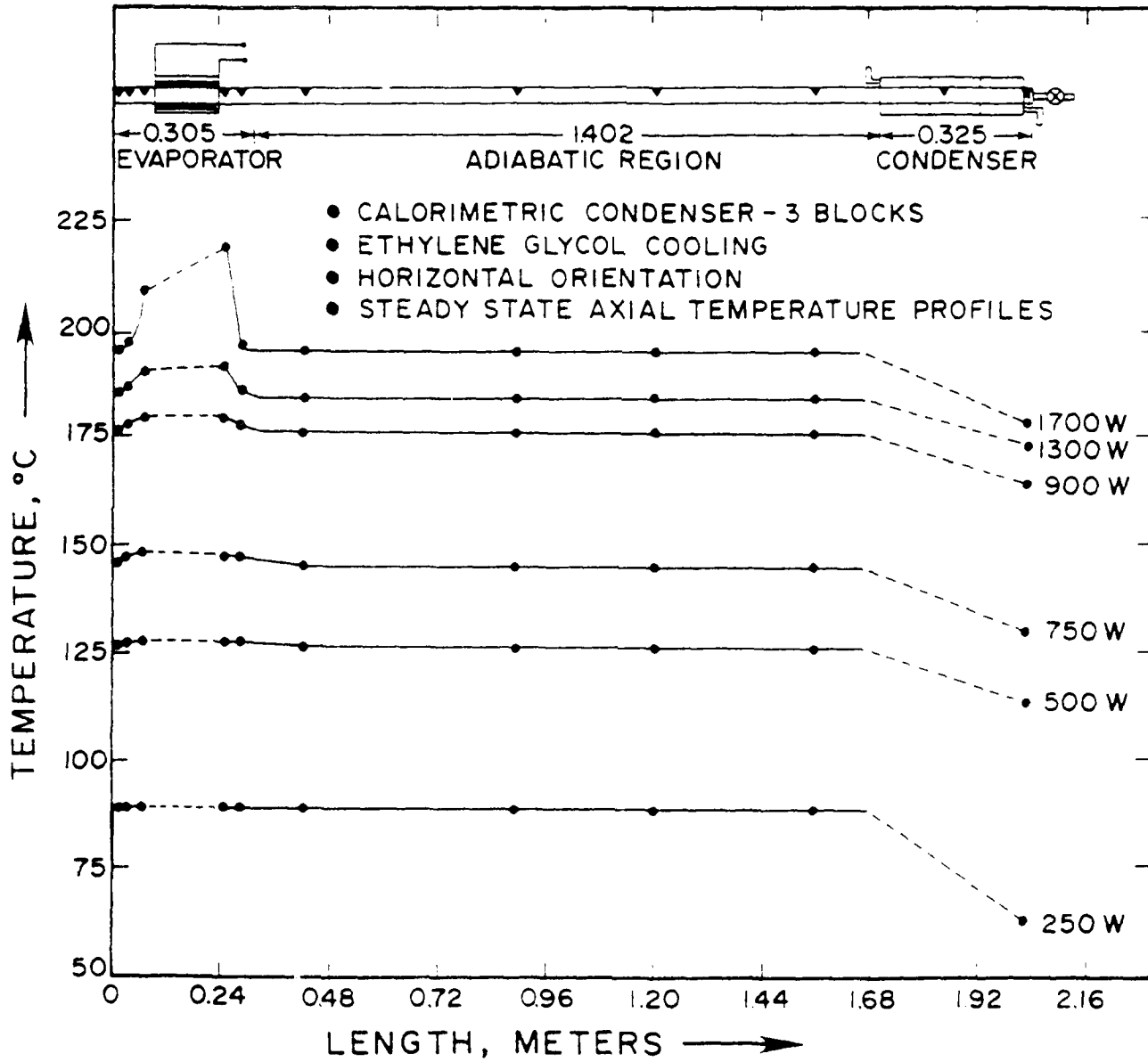


Figure 7. Axial Temperature Profile for the 2-m DWAHP with a Direct Contact 0.127-m Heater.

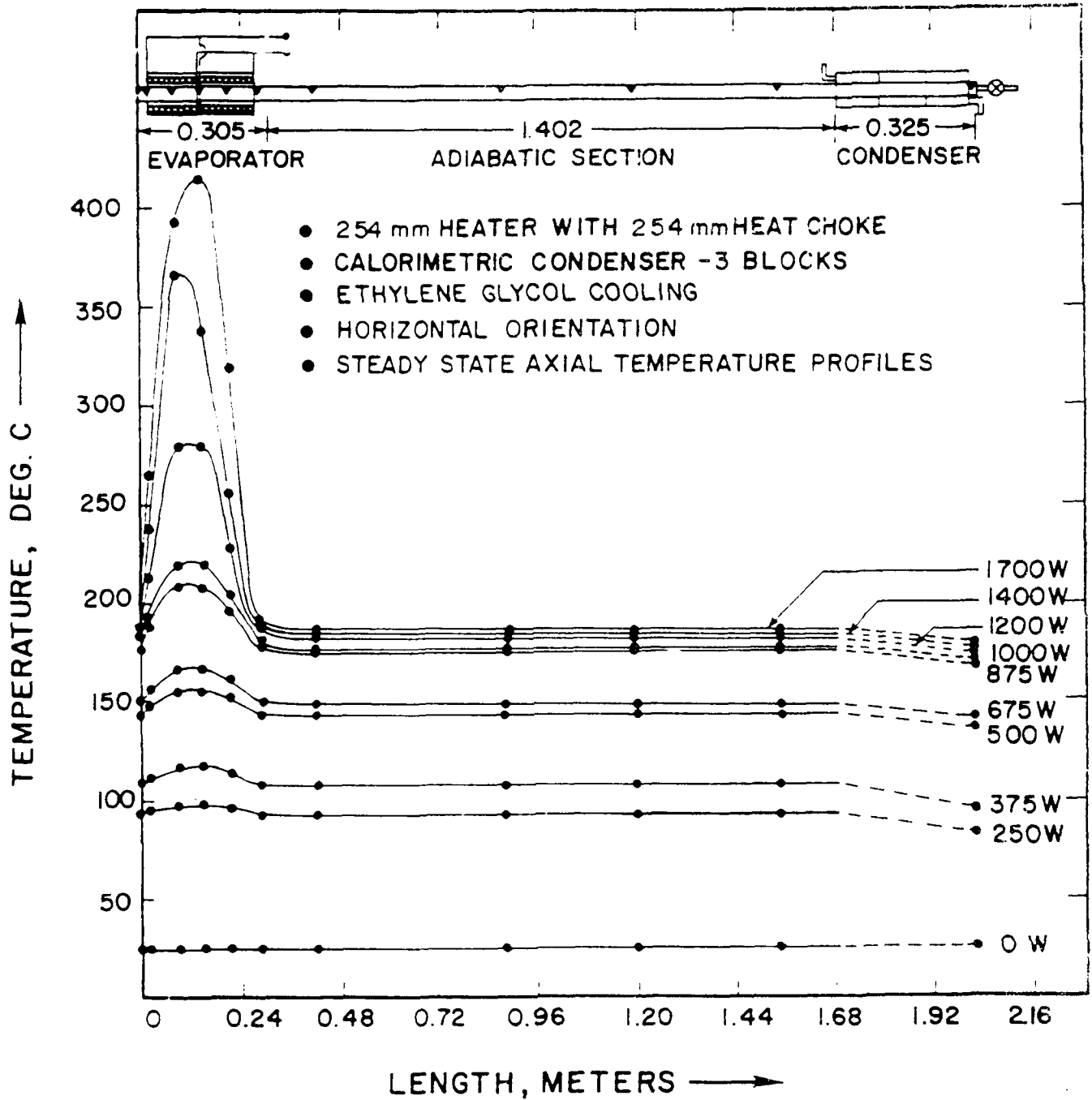


Figure 8. Axial Temperature Profiles for the 2-m DWHP with a 0.254-m Heater on a 0.254-m Heat Choke.

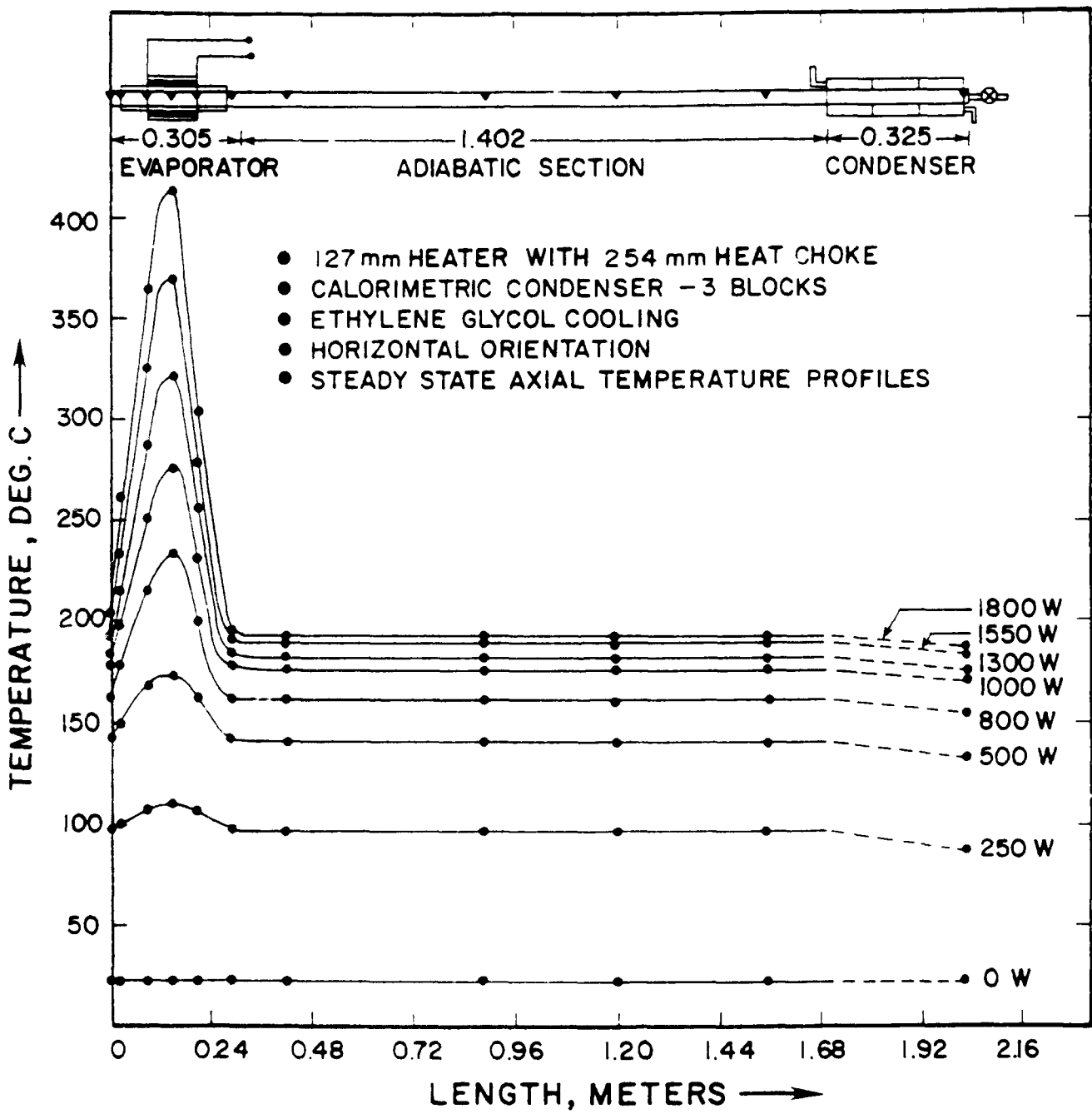


Figure 9. Axial Temperature Profiles for the 2-m DWHP with a 0.127-m Heater on a 0.254-m Heat Choke.

Another important result obtained from the long versus short heater tests (Figs. 8 and 9) is that the evaporator is performing in the same manner under low (11.22 W/cm^2) or high (23.76 W/cm^2) radial heat fluxes. In other words, the present maximum transport limit of 1700 or 1800 W is not limited by the radial heat flux handling capability of the evaporator but due to the capillary or temperature limitations.

Transient Temperatures Characterizing Dryout: A comparison of the transient temperature profiles in the evaporator, for dryout situations with direct contact and indirect contact heaters, is provided in Fig. 10 and Fig. 11. The heat pipe was not instrumented to measure the temperature at the center of the evaporator in Fig. 10, and so the ΔT values appear to be lower than those corresponding to the dryout situation with the heat choke. Actually, the temperature at the beginning of the heater should be compared to determine the highest temperature attained in the evaporator. These values were 430°C for the direct contact heater and 360°C for the indirect contact heater indicating that the presence of the heat choke helped in uniformly distributing the heat input to the evaporator. Further, the temperature rise at dryout was much more rapid in the case of the direct contact heater whereas the indirect contact configuration allowed a gradual dryout. The maximum heat input was 1850 W for the indirect contact heater as against 1700 W for the direct contact heater. Thus the introduction of the heat choke was found to be quite beneficial in many forms.

Figure 11 characterizes a typical dryout situation where the arteries get depleted of the working fluid and the temperatures initially go up rapidly in the evaporator until the input power is shut off by the computer. After this, repriming is initiated and the temperatures along the heat pipe tend to equalize gradually till all the arteries are completely primed. The thermal mass at the evaporator keeps the heat pipe operating at this stage till all the temperatures come down to ambient levels.

Effect of Partial Saturation: Table 3 gives the critical heat input values based on capillary limitation and porosity for liquid flow, as evaluated by Eq. (13). Here the porosity for liquid flow which represents the available fraction of the total void area of the wick was varied

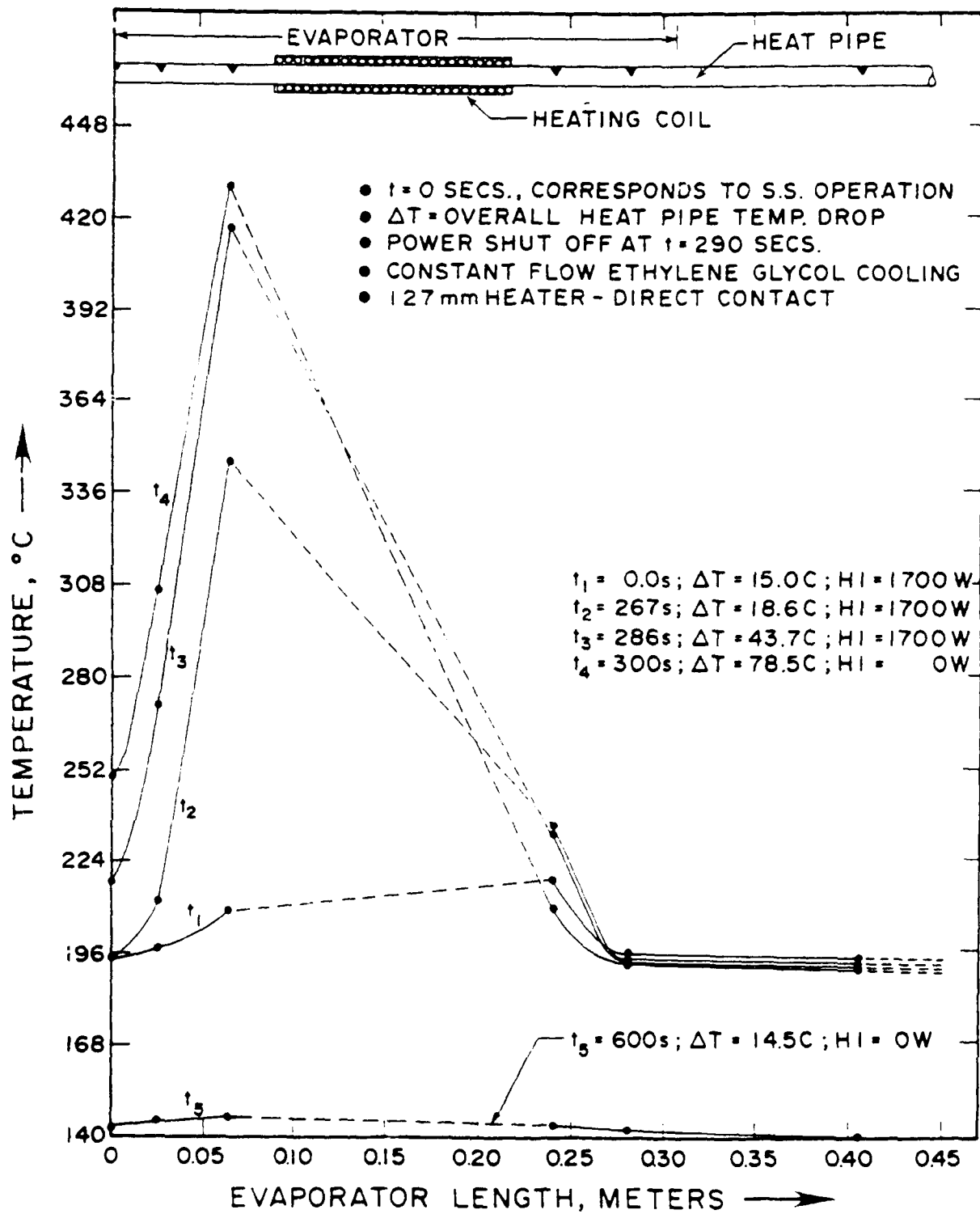


Figure 10. Transient Temperature Profiles Characterizing Dryout with a Direct Contact Heater.

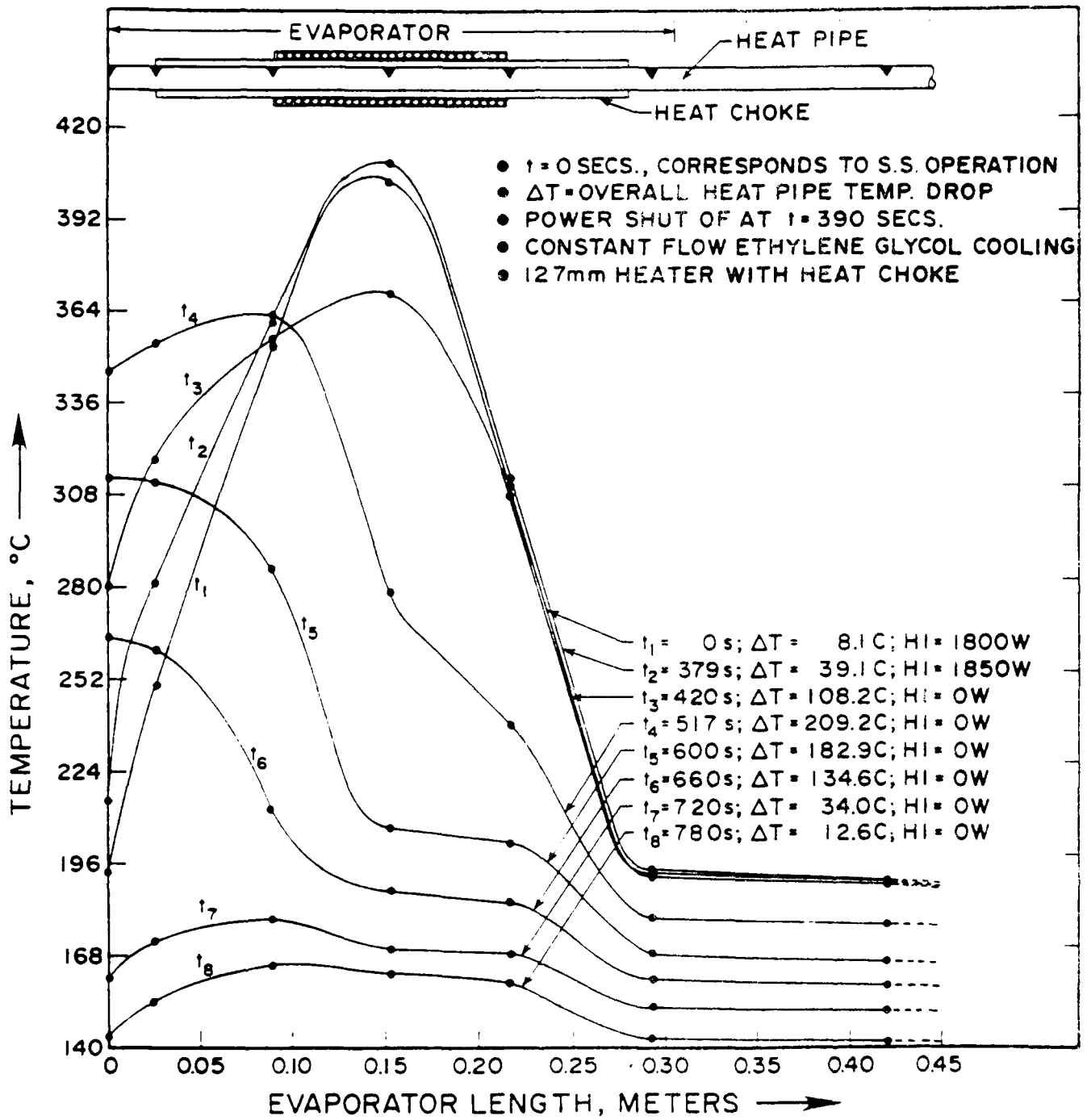


Figure 11. Transient Temperature Profiles Characterizing Dryout with an Indirect Contact Heater.

arbitrarily from a maximum value of β to a minimum value of 0.2ϵ . The values for temperatures ranging from 20°C to 254°C indicate that the critical heat input peaks at around 160°C . As mentioned earlier, this method is invalid for lower values ($\epsilon_l \ll 0.2\epsilon$) of porosity for liquid flow. For all the evaporator heater configurations considered so far, the range of maximum heat input varied from 1700 W to 1850 W indicating that the wick might have had a porosity for liquid flow of $\epsilon_l < 0.4\epsilon$, just before it dried out.

Average Effective Thermal Conductivity: Figure 12 shows the variation of average experimental effective thermal conductivities of the evaporator wick for the short and long heater modes. The experimental k_{eff} values were calculated using Eq. (17) and the average evaporator ΔT along with the net heat inputs where the radius ratio represents that of the heat pipe outer radius and vapor core radius.

$$\overline{k_{\text{eff}}}_{\text{expt.}} = \frac{0.9 Q_{\text{in}} \ln(r_o/r_v)}{2\pi L_e (\overline{T}_e - \overline{T}_o)} \quad (17)$$

At low heat input (≤ 500 W) and low heat flux (≤ 11.22 W/cm²), the experimental k_{eff} (22-25.5 W/m K) matches with that predicted by Eq. (2), (23.55 W/m K). At higher fluxes and power inputs, the experimental k_{eff} drops down. This is apparently due to the effects of vapor film impeding the heat transfer at the wick/inner wall interface. It is becoming clearer that computing k_{eff} for "boiling-tolerant" wicks based on 100% saturation is erroneous. True prediction of k_{eff} for such "boiling-tolerant" wicks should include convective effects in addition to conduction.

2.5 USEFULNESS AND PRACTICAL SIGNIFICANCE

This research was aimed at developing a semi-theoretical explanation for the discrepancy in the performance of the double wall artery heat pipe between the designed heat transport

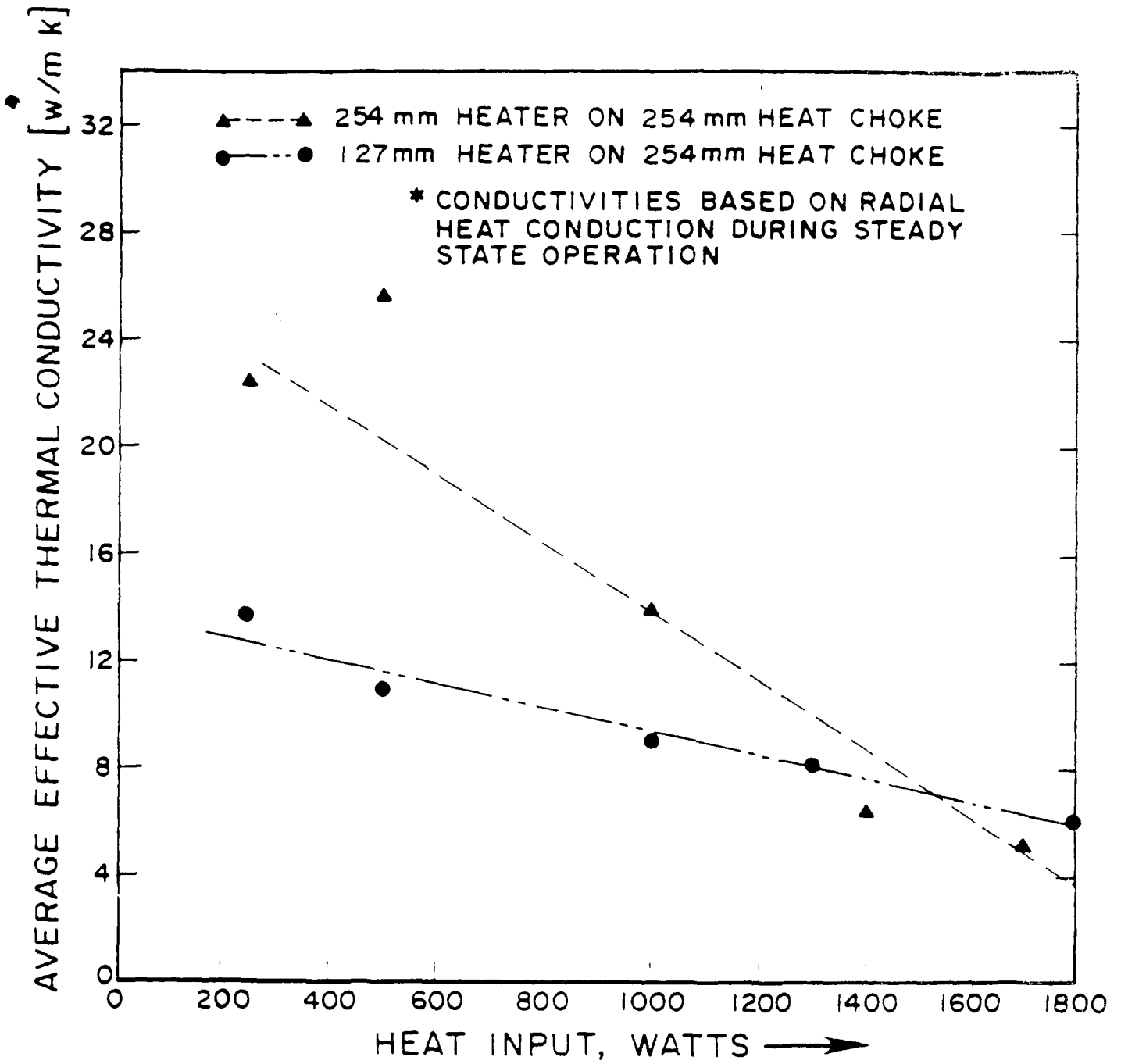


Figure 12. Variation of Average Effective Wick Thermal Conductivity with Heat Input for Two Heater Configurations.

capability and the actual experimental values obtained. An attempt has been made to predict the microscopic heat transfer mechanism and the thermal resistances in the evaporator using only the external temperature measurements and the macroscopic thermal performance without getting involved with internal measurements and the uncertainties accompanying them. This analysis not only adds credibility to relevant earlier investigations but also attempts to bridge the gap between the theoretical and experimental results.

In spite of many years of research publications found in the literature on boiling heat transfer, there is a wide gap between the practical applications such as the heat pipe and the available basic theory. The presence of porous wick structure and the dependence on the wick capillary force for the condensate liquid return flow, complicate the boiling heat transfer problem associated with the heat pipe evaporator. The conventional heat pipes usually depend on conductive evaporation in the evaporator for heat transfer where boiling is not tolerated. Advanced high capacity wick designs, such as the DWAHP, use composite wicks which are "boiling-tolerant." The partial liquid saturation with evenly distributed micro vapor-channels in the wick (Fig. 2(B)) supports high radial heat flux.

The practical significance of this research centers around the capability to accurately predict the critical heat flux of a heat pipe evaporator. The key thermophysical parameter governing this is the effective thermal conductivity (k_{eff}) of the wick. And the present paper contains useful information regarding k_{eff} calculation and shows the limitations of the 'series-parallel model' and the 'mean-gap model'.^{17,18} The authors did not recommend the use of these models for high capacity heat pipe designs. Although insitu measurement of k_{eff} is very difficult, an indirect method of measuring the lumped average effective thermal conductivity has been demonstrated. This method could be used in any heat pipe testing. The present experimental results are expected to help the formulation of new empirical correlations similar to that of Alexander.¹⁹ A theoretical model which can account for the partial saturation and convective effect of the vapor within the wick pores would be an appropriate solution for this problem.

2.6 CONCLUSIONS AND RECOMMENDATIONS

Conclusions:

1. The 2-m copper-water DWAHP evaporator heat transfer and performance characteristics such as boiling limit, ΔT_{crit} , and k_{eff} have been analyzed and compared with experimental results.
2. The wick effective thermal conductivity model based on 100% saturation and the condition of "no-boiling" does not apply to the DWAHP situation. The theoretical k_{eff} value for 63% porous copper screen saturated with water is 1.673 W/m K while the experimental k_{eff} for the DWAHP at low heat input and flux is 22.5 W/m K. This experimental value matches with that predicted (23.55 W/m K) using Alexander's relation.
3. The critical heat rate tolerable at the double wall evaporator without causing boiling in the wick is very low (~200 W).
4. A film boiling situation and the presence of a thin vapor film at the wick/inner wall is theorized to explain the high evaporator ΔT (~100-150 K) and the "boiling-tolerance" of the double wall wick.
5. Axial and radial conduction at the evaporator exit region where the capillary inserts are installed, are not significant. Arteries should be cooled below the saturation level to a ΔT predicted by the Clausius-Clapeyron relation so that bubble generation within the arteries is eliminated.

6. The revised capillary limit calculation based on the partial saturation of the wick puts the experimental results in the range of 20 to 40% of liquid and the remaining 80 to 60% vapor in the wick pores. The inability to measure the wick saturation in actual heat pipe testing makes the comparison of experimental and theoretical results difficult.

Recommendations:

There are several directions in which the DWAHP related research could be augmented or extended. There are also some science issues and new directions to be explored. These are,

1. The physically separated vapor and liquid flows in the DWAHP helps to subcool the artery channels. The effects of subcooling and internal insulation between vapor core and the artery channels to aid Clapeyron priming may be explored.
2. Mechanical vibration is certainly a factor affecting the priming and the overall performance. This aspect should be studied.
3. Through a computerized design, it is very easy to optimize the artery or groove size; smaller artery grooves may be sufficient.
4. In DWAHP 2m #2, the knocking and "water hammer" effect was very severe. The connection between the ventless transport and this phenomenon needs to be investigated in detail.
5. The lower liquid flow friction advantage is not fully realized in 2m design. If this is to be noticed distinctly, at least a 5m long DWAHP must be designed and tested.
6. Although survivability questions are raised in connection with liquid metal heat pipes, it is equally important in water heat pipes also if they are to be used in space radiators.

7. DWAHP design certainly has to be verified in other temperature regimes such as in methanol, freon, liquid metal, and cryogenic heat pipes also.
8. In case the double wall design is considered for future space applications, its working must be verified for zero gravity operation.
9. Existing heat pipe design codes may be adopted or a new design code may be evolved to optimize the DWAHP design.
10. After the inner tube and wick assembly into the outer tube, the pipe could be mechanically swaged to lock the pipes together. This is expected to eliminate the cross communication of fluid between grooves thereby make the theoretical modeling more accurate.
11. Bendability tests may be initiated in order to take care of special applications in space radiators.
12. Life testing of copper-water DWAHP for potential use in special missions such as Mars-Mariner II program or space station.
13. Testing of the 1.2m DWAHP #1 with ethylene glycol cooled saddles for steady and transient performances.
14. Conduct visualization experiments with 2 m DWAHP #1 (with vented arteries) to observe vapor venting process.

SECTION III

LIQUID METAL DWAHP: ADDITIONAL TEST RESULTS OF GAS AND VACUUM MODE STARTUPS

3.1 POTENTIAL USE AND PROBLEM AREA

Liquid Metal Heat Pipes (LMHP) using potassium, sodium and lithium as working fluids have potential application in space power systems such as SP-100, space station, and a variety of military spacecraft. Also, gas-loaded LMHPs are used in terrestrial applications such as isothermal black body standards for sensor calibration and semiconductor single crystal processing.^{27,28} In all these applications of the LMHPs, some of the important performance criteria to be investigated are startup, shutdown, isothermality, and active condenser length regulation. Noncondensable gas (NCG) filling converts a conventional heat pipe into a variable conductance heat pipe (VCHP). Low temperature VCHPs have been extensively researched in the past, and they are used in thermal control application of low power communication satellites. However, only a limited number of research publications are available in the high temperature VCHPs. Also, it is believed in certain sections of the heat pipe research community that LMHPs do not have any startup problems, and any attempt to gas-load a LMHP would adversely affect the priming of arterial type heat pipes.²⁹ In order to understand these problems closely, a 2-m stainless steel - sodium, argon filled, grooved artery heat pipe was designed, fabricated and tested. Experimental results showed successful startup and performance.³⁰⁻³²

It is extremely difficult to fabricate a perfectly gas-free heat pipe in actuality. As the heat pipes are usually long and slender tubes, evacuating them to ultra-high vacuum levels (10^{-8} torr or better) before filling with working fluids is impossible. For a typical heat pipe 2 m long, 2.22 cm vapor core diameter, if the fill tube end is at 10^{-6} torr, the closed end will be at 10^{-4} torr assuming reasonable outgassing rate for the pipe and pumping capacity for the vacuum pump. Hence, there is always a small quantity of residual gas left inside the pipe. The quantity of residual gas (ideal gas) at 10^{-4} torr and 300 K is 13.78×10^{-10} gram-moles for the heat pipe

mentioned above. Appendix A shows the details of this calculation. In addition to the residual gas, there are other sources of gas contributing to the total NCG that may be present within the heat pipe. For example, the internal surfaces of the pipe and wick structure may degas at high operating temperatures due to minute impurities and adsorbed gases which are released on heating.³³ If an LMHP is operating in a moist environment, there is the likelihood of hydrogen permeation into the pipe.²⁹ Hence, in a practical sense, a truly vacuum mode heat pipe is nonexistent. On the other hand, gas-loaded on purpose or already present as residual gas, if it contributes to the easy and rapid startup from frozen state and problem-free shutdown, then this class of heat pipe has to be exploited for practical applications.

The objective of the present study is to obtain the comparative performances of an LMHP in vacuum and gas-filled modes and to verify the smooth and rapid startup of the gas-filled mode from frozen state. The performance characteristics including the frozen state startup of the near-vacuum mode and gas-loaded mode of a particular LMHP are presented. Also, it is shown that gas loading could be predetermined in LMHPs such that the inactive condenser length is kept very small and no gas reservoir is required.

3.2 THEORETICAL CONSIDERATION ON GAS FILLING LIMITS

The operating temperature of the heat pipe and the gas charge pressure will vary depending upon the working fluid used. The gas-blocked length of the condenser can be designed to vary from full length at startup to less than 5% of the full length based on the working fluid and the initial gas charge pressure.

For a cylindrical heat pipe of uniform vapor core cross section, the ratio of gas-blocked length to total pipe length is approximately given in terms of the pressure ratio as in Eq. (18).^{31,34}

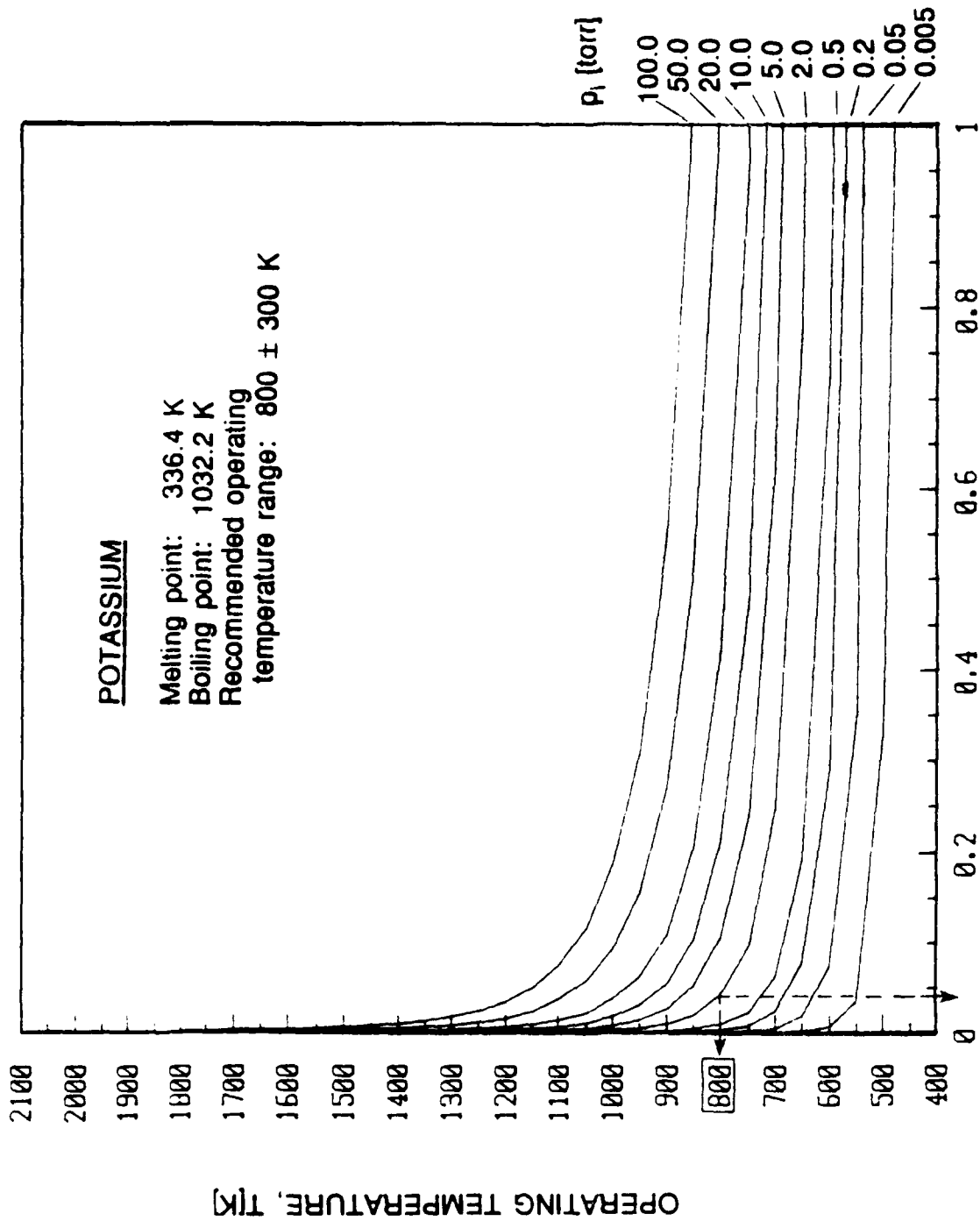
$$\frac{L_g}{L_p} = \frac{P_l(T_c)}{P_v(T)} \quad (18)$$

In deriving Eq. (18), it has been assumed that (1) the noncondensable gas behaves as an ideal gas at the heat pipe operating temperature and pressure; (2) a narrow diffusion region separates the hot vapor zone and the cold gas zone under steady state; (3) axial conduction along the wall and wick is neglected; and (4) the gas is compressed to the pressure of the working fluid vapor at the hot zone temperature.

Figures 13 (a), (b), and (c) show the graphical results of Eq. (18) for potassium, sodium and lithium respectively. The fraction of the heat pipe length blocked by NCG is plotted as a function of temperature for various possible initial gas charge pressures (0.005-100 torr). The recommended nominal operating temperatures based on the optimum liquid transport factor for potassium, sodium and lithium are 800 K, 1000 K and 1300 K, respectively. The operating temperature range for each fluid is normally 300 K below and 300 K above this nominal temperature. The initial gas charge pressure range of 0.005-100 torr is chosen based on this temperature range for each fluid. It is to be noted that a gas-loaded LMHP does not start up until the vapor pressure of the working fluid equals or exceeds the value of the initial gas charge pressure. In Fig. 13, for an initial gas charge pressure of 2.0 torr, the gas-blocked length at the nominal operating temperature is less than 5% of the total length for all fluids.

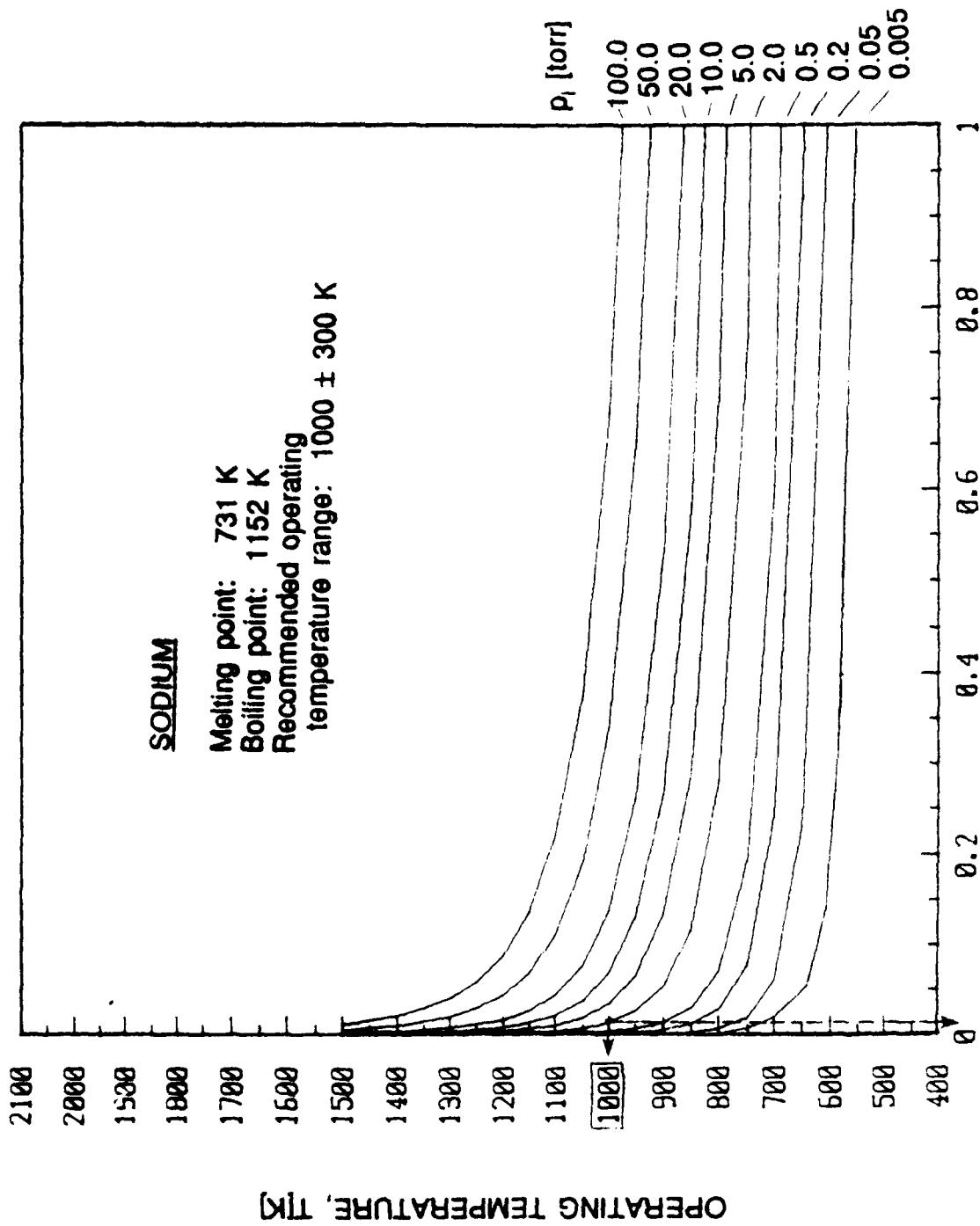
3.3 EXPERIMENTAL WORK

Test Article Description: The experimental LMHP was made of stainless steel material and filled with sodium as the working fluid. The wick structure was of the "double wall artery" design with only one transport artery groove channel. The evaporator and condenser sections had identical grooved inner tube and screen tube wick construction. The cross-sectional and longitudinal sectional views of the heat pipe are shown in Figs. 14 and 15, respectively. The total length was 2.03 m and the diameter was 2.22 cm. Each of the 24 evaporator and condenser grooves was 0.79 mm wide and 1.40 mm deep while the single adiabatic groove was 2.38 mm square. The evaporator, transport and condenser lengths were 33 cm, 79 cm and 91 cm, respectively, and the effective length was 1.388 m. The central line axis along the groove bottom in the transport section was collinear with the corresponding evaporator and condenser grooves



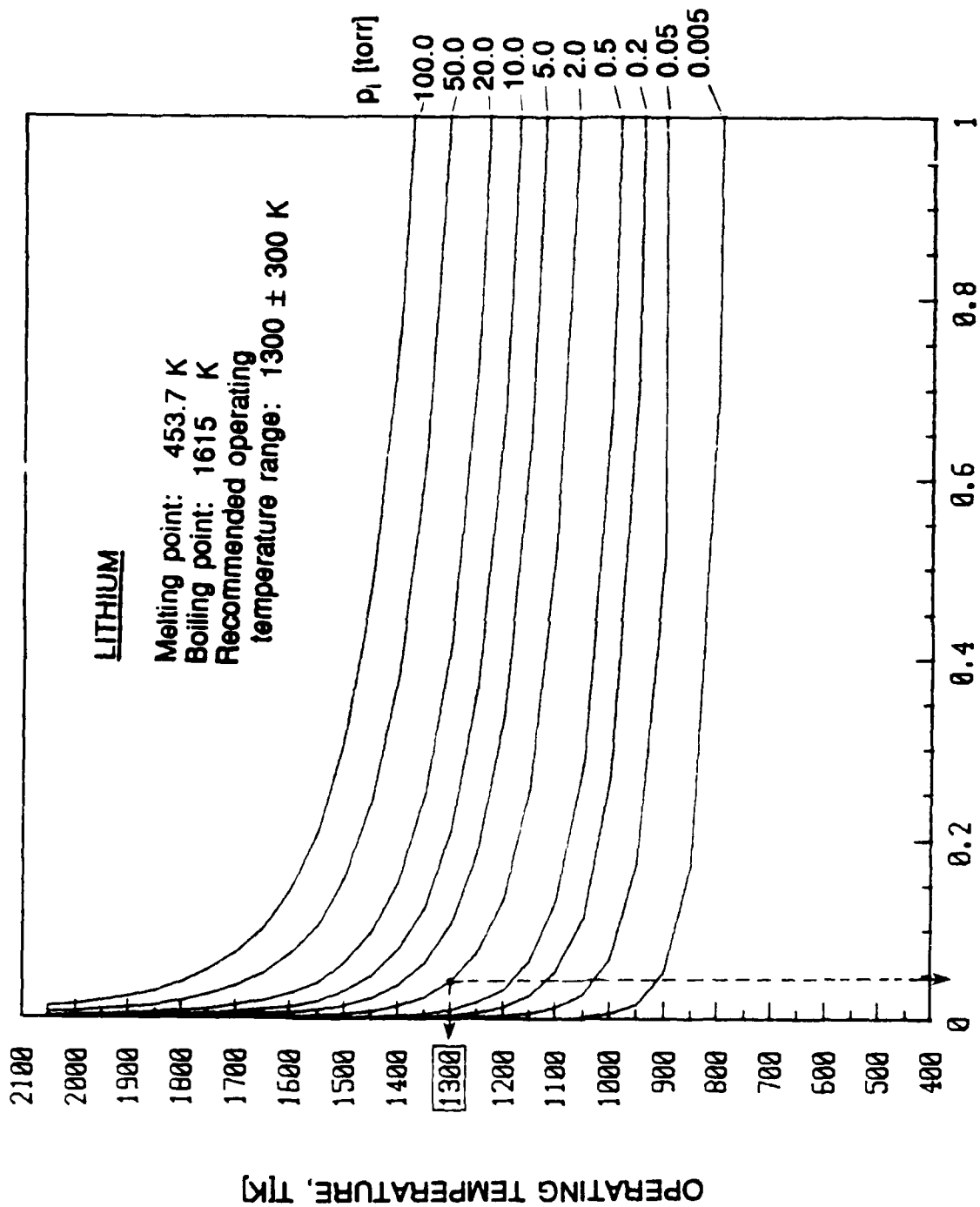
FRACTION OF THE TOTAL LENGTH BLOCKED BY GAS, L_g/L_p [DIMENSIONLESS]

Figure 13(a). Gas-Blocked Length as a Function of Initial Gas Charge Pressure for Potassium Heat Pipes.



FRACTION OF THE TOTAL LENGTH BLOCKED BY GAS, L_g/L_p [DIMENSIONLESS]

Figure 13(b). Gas-Blocked Length as a Function of Initial Gas Charge Pressure for Sodium Heat Pipes.



FRACTION OF THE TOTAL LENGTH BLOCKED BY GAS, L_g/L_p [DIMENSIONLESS]

Figure 13(c). Gas-Blocked Length as a Function of Initial Gas Charge Pressure for Lithium Heat Pipes.

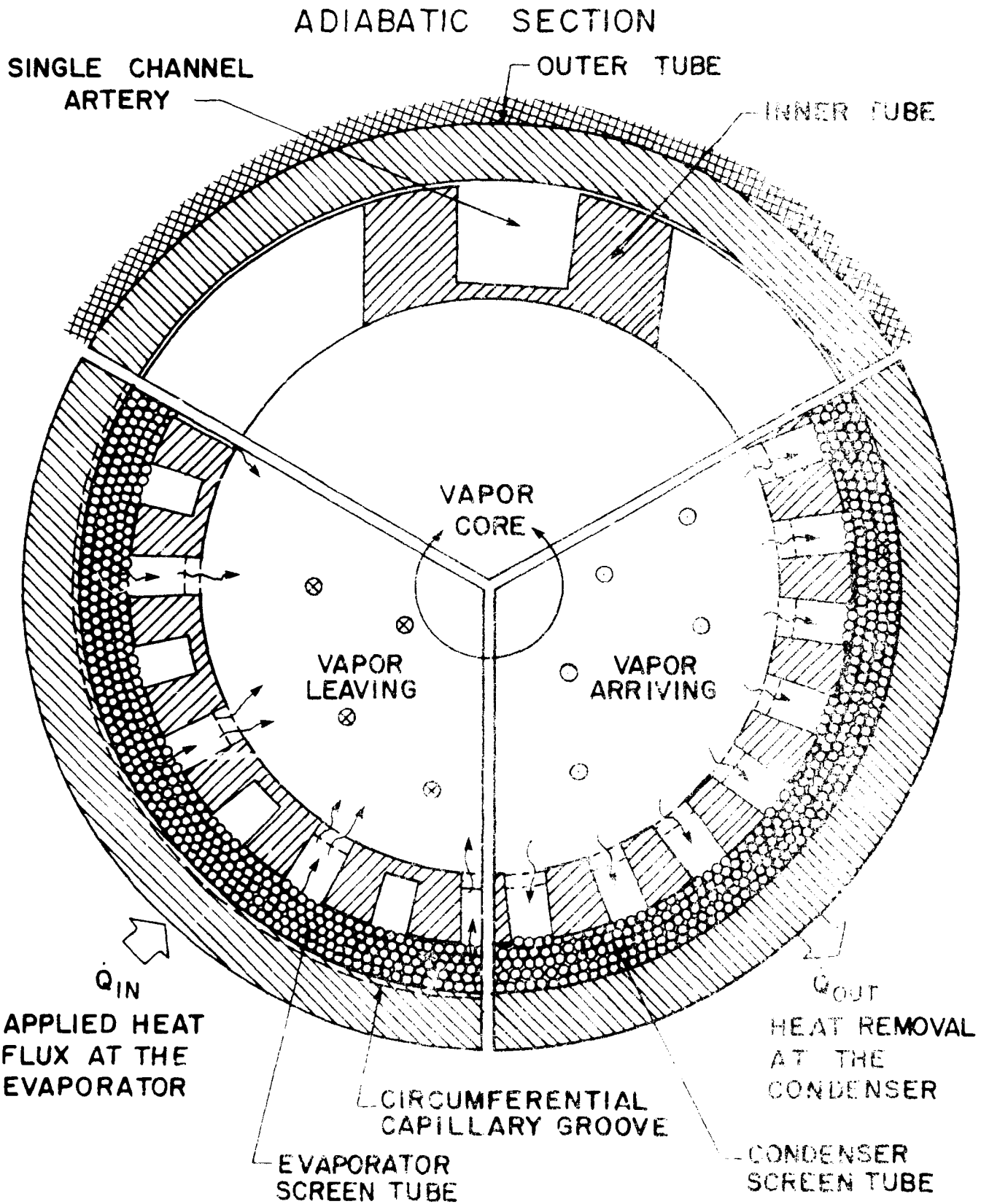


Figure 14. Cross-Section View of the Liquid Metal DWHP.

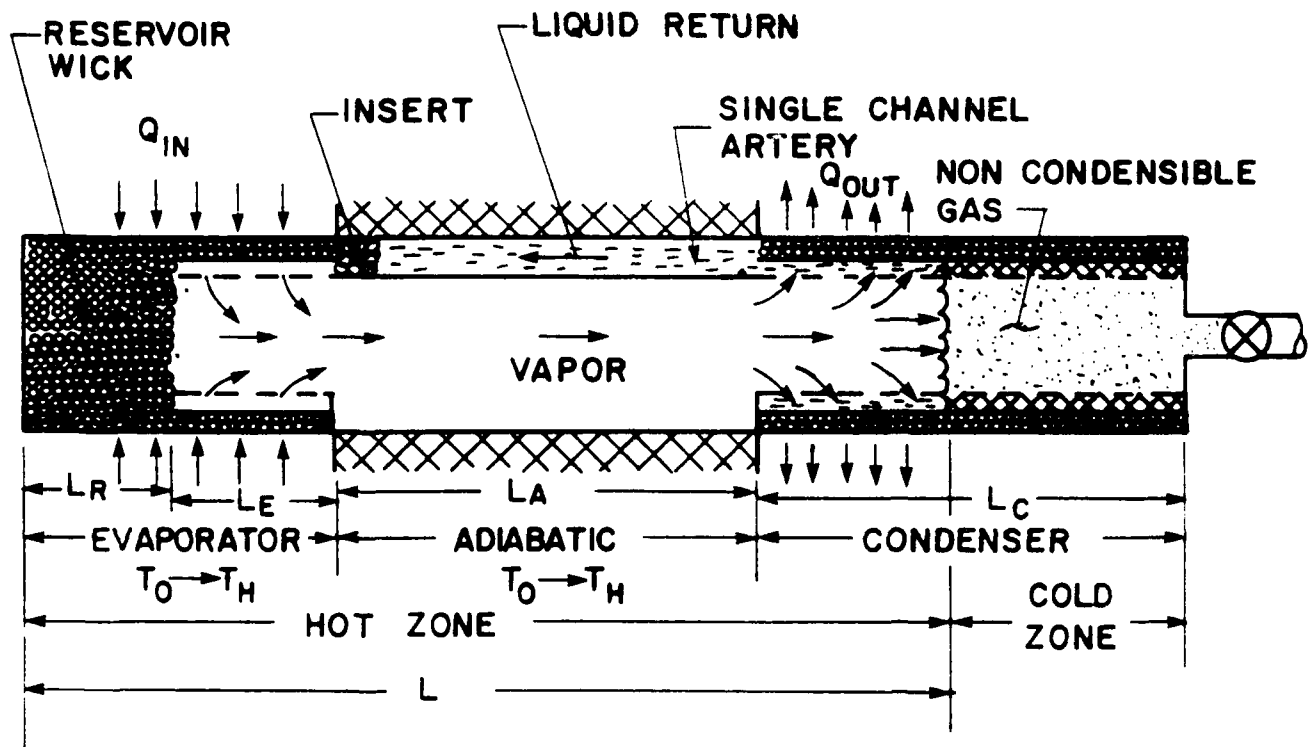


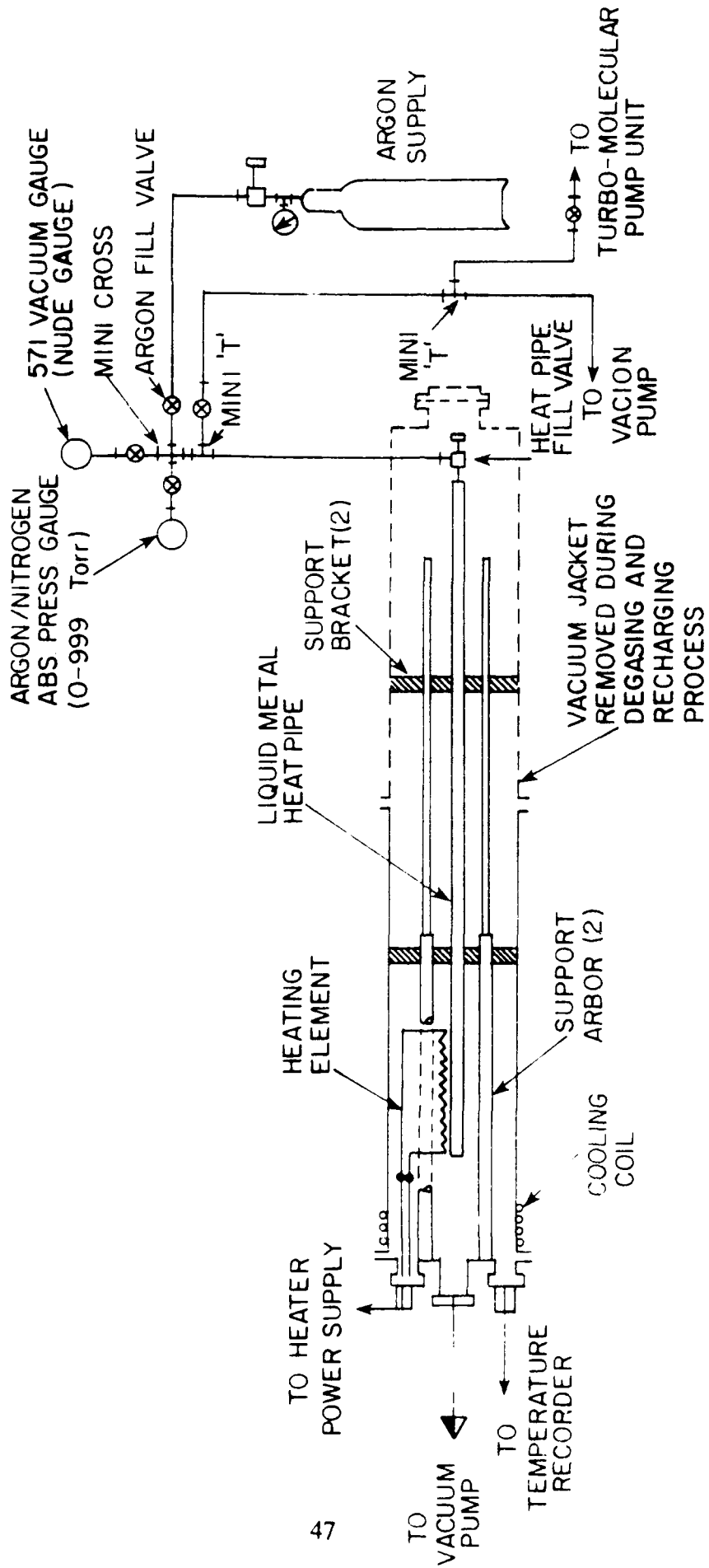
Figure 15. Longitudinal Section View of the Liquid Metal DWHP.

in alignment. The 12.5-cm-long, 1.89-cm-dia, $40 \times 40 \text{ cm}^2$, 75.25% porous reservoir wick was in capillary contact with the $40 \times 40 \text{ cm}^2$, 62.9% porous evaporator screen wick. The pipe was loaded with 92.04 g of pure sodium calculated for optimum fill at 1000 operation. A bellows-type high temperature all metal valve rated good for 649°C at 1700 kPa enabled the processing of sodium or inert gas to or from the pipe. A comprehensive description of the design and processing details can be found in the technical report (Ref. 31).

Test Setup: The LMHP was instrumented with electrical resistance heaters for the evaporator and trace heating and chromel-alumel thermocouples for external wall temperature measurement. The main heater was made of pyrolytic graphite strips coated (CVD) on boron nitride substrate and covered with the same material. This thin walled custom designed tubular heater was capable of operation up to 2000°C in vacuum. The heater assembly and constructional drawings are provided in Appendix B along with the manufacturer's specifications. The heater was radiatively coupled to the heat pipe in order to reduce the evaporator thermal mass. High temperature ceramic insulator and multiple layers of polished stainless-steel radiation shields provided heat insulation to the heat pipe which was mounted concentrically within a 20-cm-dia, 230-cm-long vacuum chamber. Cooling water circulating in coils wrapped around the chamber provided the heat sink and calorimeter for the test. The chamber was pumped down to 10^{-6} torr or better for eliminating convective losses and corrosion of the LMHP. The frame holding the chamber was mounted on a fulcrum support to enable tilting of the heat pipe for force priming in case of a dryout.

A plumbing arrangement as shown in the schematic of Fig. 16 was used whenever the gas pressure inside the heat pipe was to be measured or changed. The vacuum system was capable of 10^{-8} torr holding-vacuum and the argon/nitrogen pressure gauge could measure absolute pressure in $\pm 0.5\%$ increments up to 999 torr.

The heater section was insulated with a combination of zircar high temperature ceramic insulation and stainless steel multilayer radiation shields. Zircar provided a better shielding than the stainless steel shield. A possible disadvantage was the release of trapped moisture during



DEGASING & INERT GAS RECHARGING UNIT

Figure 16. Noncondensable Gas Charging and Pressure Measurement Schematic Diagram.

high temperature and vacuum conditions. It has been reported in the high temperature heat pipe test research literature that the moisture so released could dissociate and let hydrogen into the heat pipe. Figure 17 shows the radiation shield and thermocouple locations. Appendix C gives the manufacturer's specifications of zircar cylinders. Redundant overtemperature protection was provided to safeguard the heat pipe evaporator from burning out in case of wick dryout or erroneous behavior of the heat pipe. This was accomplished by incorporating control thermocouples in the evaporator area and interconnecting them with analog and digital type relay cutouts to switch off power input to the heater. Figure 18 shows the circuit diagram.

Test Procedure: At the beginning of the present round of tests, the LMHP was reprocessed to make up for the sodium lost (about 25% of the inventory) during an earlier gas venting operation in hot condition (500°C). As the refilling process was done under high vacuum conditions, the pipe was considered to be in vacuum mode. Transient and steady-state tests were conducted in this mode in horizontal position with the adiabatic artery at the 3 o'clock orientation. Startup tests from frozen state were usually started in the beginning of the day when the pipe had cooled down to room temperature. In a typical test run, a desired constant power input was applied to the evaporator in one step, and the temperatures along the length of the pipe were recorded at intervals of 1 minute for nearly 3 hours. High temperature alarm limits were set on the heater and evaporator thermocouples to cut off the heater and evaporator thermocouples to cut off the heater power. Transient tests were usually followed by steady-state tests. The condenser shutters were locked in fully closed position. This arrangement prevented the condenser from quenching and at the same time allowing sufficient radiation to pass through. At steady state, power input, axial temperatures, cooling water inlet and outlet temperatures and flow rate were recorded.

After vacuum mode tests, the LMHP was filled with 2.0 torr of argon using the rig shown in Fig. 16. Then the functional tests were repeated in the gas-filled mode in the same manner described above.

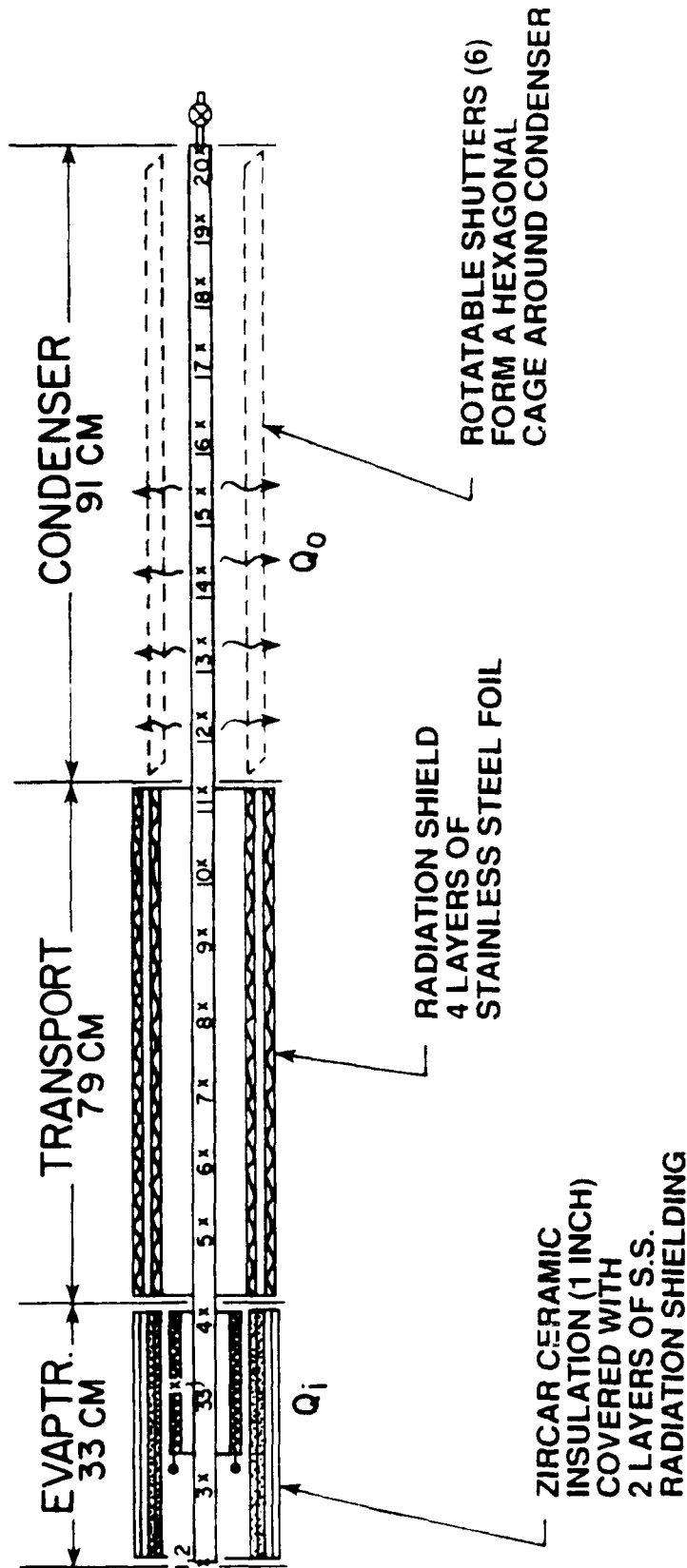
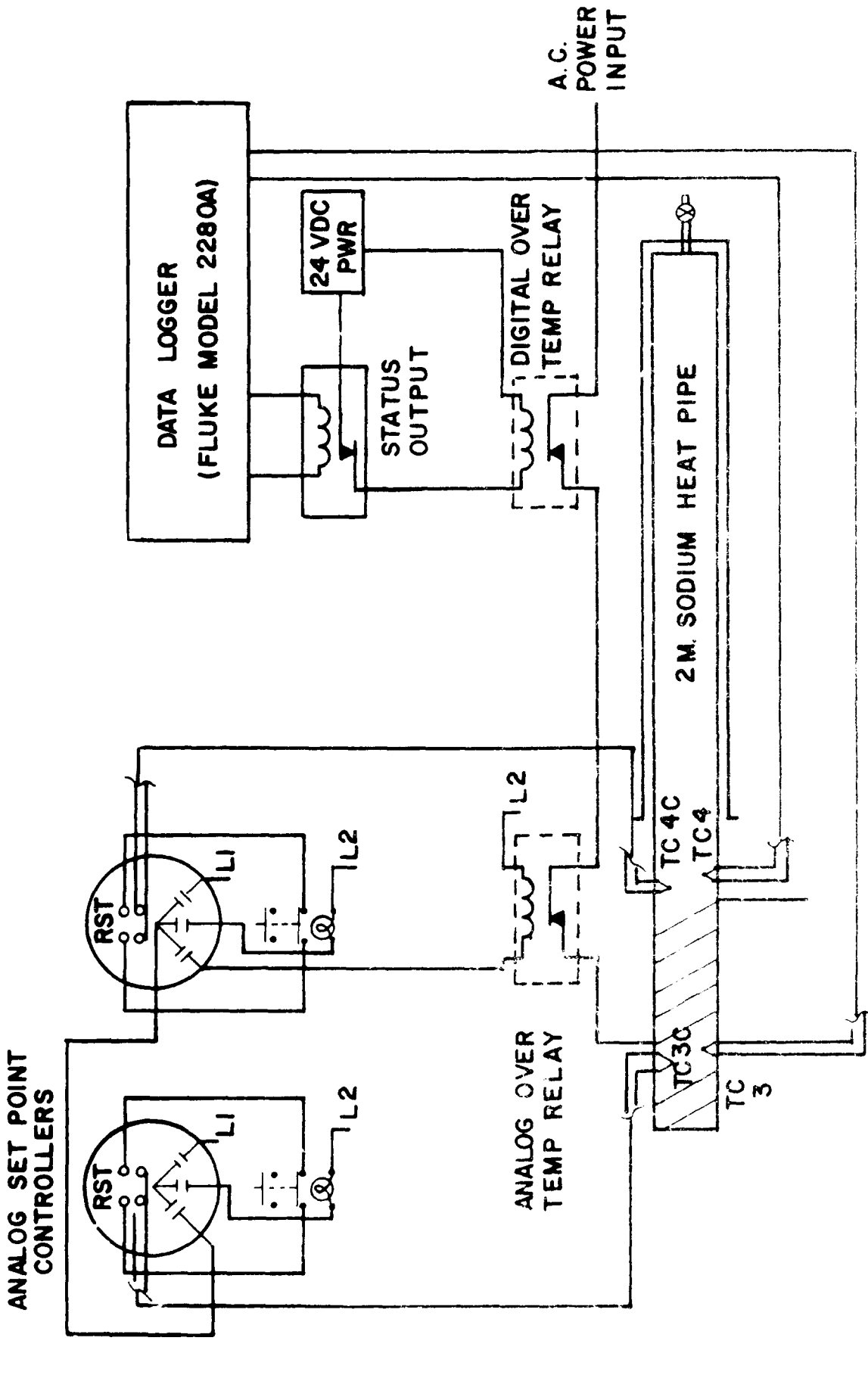


Figure 17. Radiation Shield and Thermocouple Location Details.



LI = 110 V HOT
 L2 = 110 V RETURN
 TC = THERMOCOUPLE NO.

Figure 18. High Temperature "Run-Away" Protection Circuit.

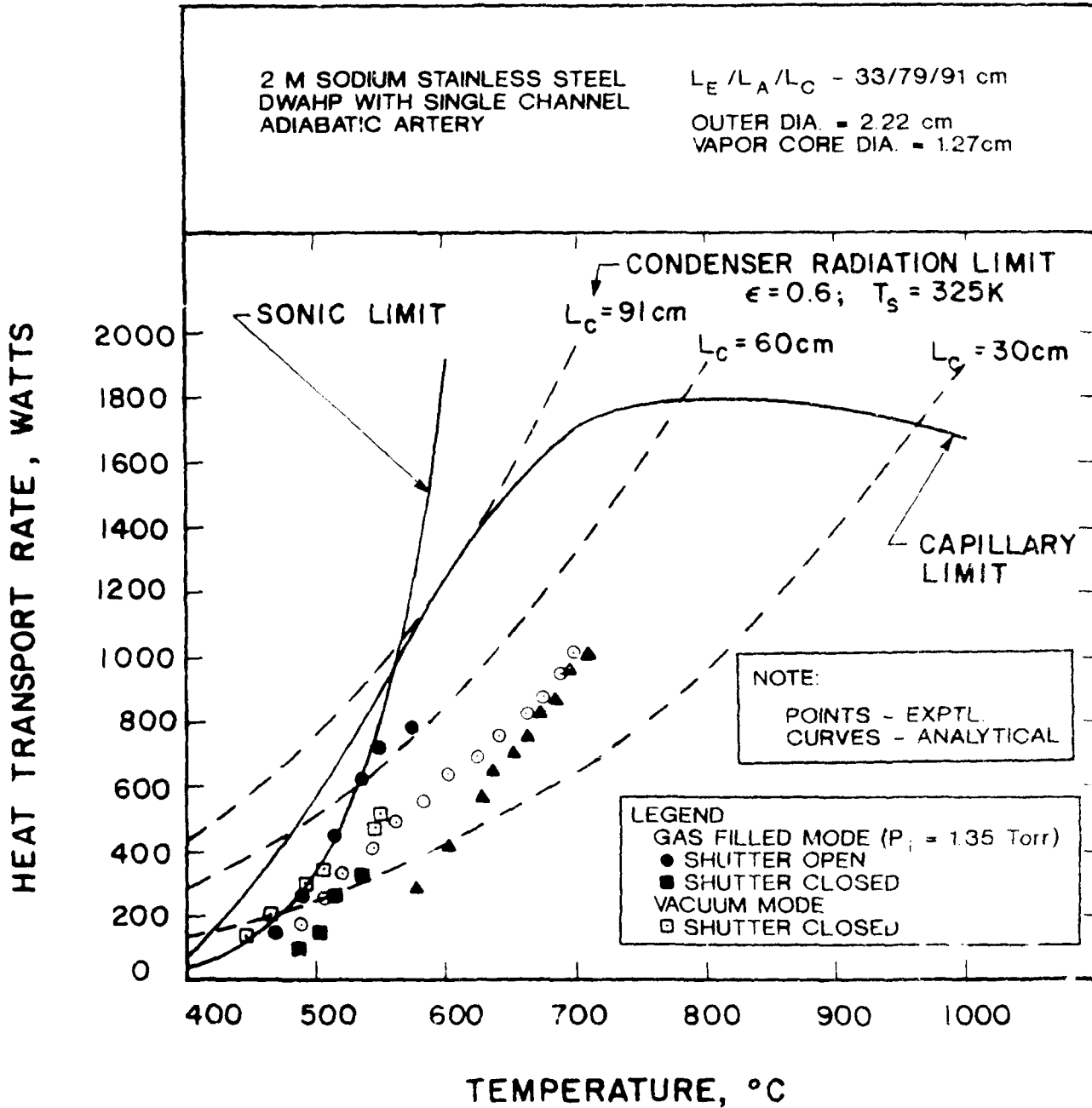
3.4 RESULTS AND DISCUSSIONS

The accuracies of temperature, power and flow measurements were reasonable and the repeatability of test results were good. The output power measured through the calorimetric data was within 5% of the electric power input measured. Mostly, the vacuum and gas-filled mode startup test results of the reprocessed pipe are compared and discussed here. In addition, the transport capacity and inactive condenser length data for all the tests done so far on this LMHP are presented.

3.4.1 Transport Capacity

The experimental transport capacity data are plotted along with the theoretically predicted sonic and capillary limit curves in Fig. 19. The experimental points correspond to the average hot zone temperature T_H and the condenser radiated power, Q_c . It may be noted that with the new graphite heater, the LMHP could be run at 1000 K transporting nearly 1000 W. The new data points lie away from the sonic and capillary limit curves due to the closed shutter condition which made the pipe run at higher temperatures than otherwise. The average operating temperature of the hot zone could have been reduced by opening the condenser shutter. The shutter opening mechanism was broken during these tests. The pipe was not operated near the designed maximum transport limit of 1800 W for safety reasons. The heater was running at 1250°C when the average hot zone was near 800°C. As the temperature of the pipe went up, it became riskier to run the test; more thermocouples broke and the heater got closer to meltdown. Hence, a 1000 K operating temperature limit was set and followed.

The maximum transport capacity attained in both vacuum and gas modes were the same. At low transport rates (<500 W), the pipe operated at lower temperatures (about 50-100 degrees lower) in vacuum mode compared to the gas mode for identical test conditions.



LEGEND (ADDITIONAL TESTS AFTER REPROCESSING)	
○	VACUUM MODE; SHUTTER CLOSED
▲	GAS FILLED ($P_i = 2.0$ Torr); SHUTTER CLOSED

Figure 19. Predicted and Experimental Performances (Q_o vs T_H).

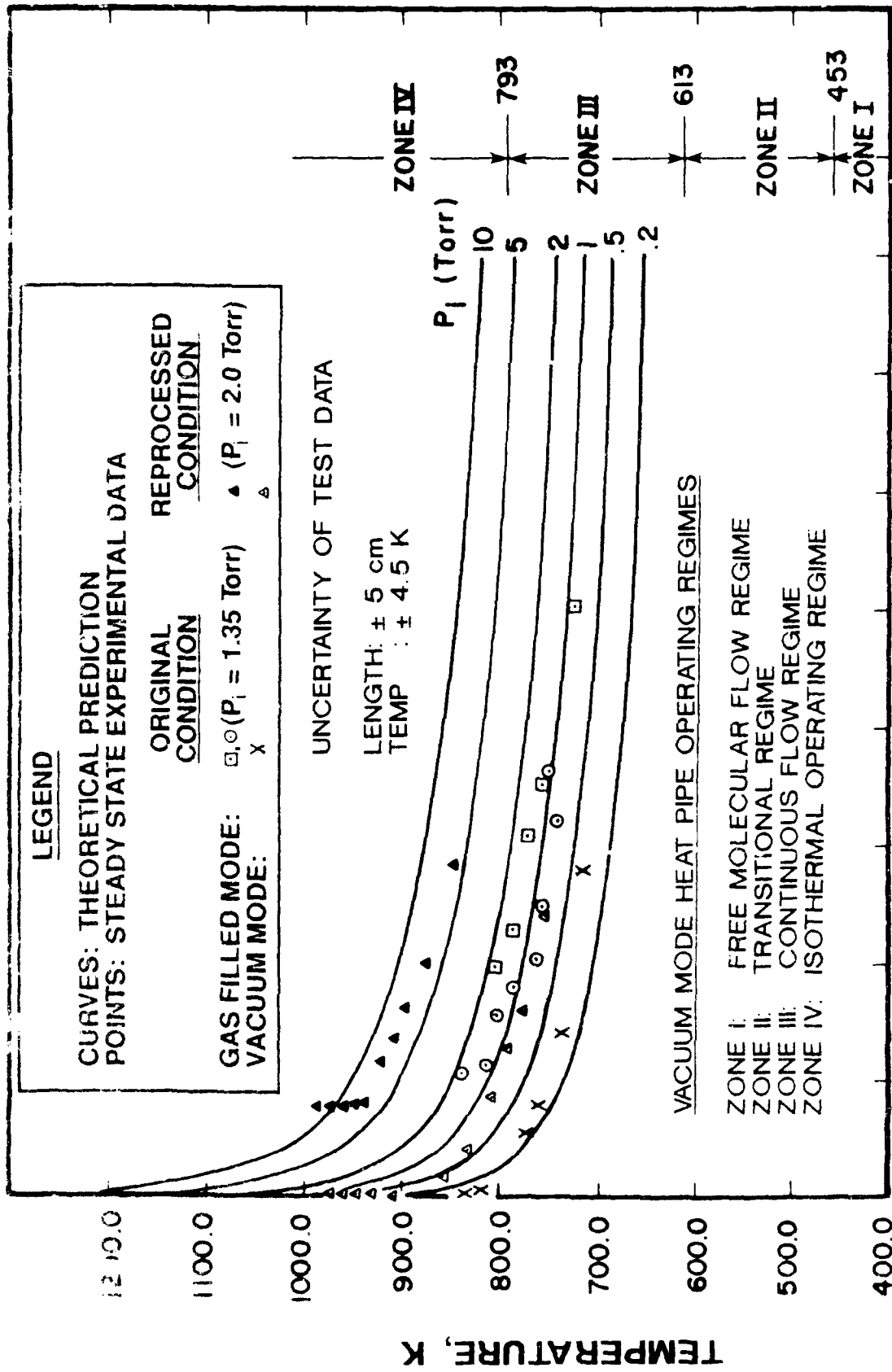
3.4.2 Inactive Condenser Length

Figure 20 shows the inactive condenser length as a function of the operating temperature for various test conditions. From the figure, in vacuum mode tests, there is no inactive condenser with sufficient power input to the pipe. At low power levels, only a fraction of the condenser is needed to dissipate the heat load and hence these points do not represent gas slugged length. In the case of gas-loaded mode, all the data points above 935 K show 18 cm of gas-blocked condenser. The 2.0-torr gas mode experimental data lie along the 510-torr theoretical curves. The reason for the lateral shift is attributed to the heating of the inactive condenser (gas-blocked length) by the reradiation from the closed condenser shutters. This experimental setting happens to be in violation of the assumption that the cold zone is at the sink temperature as described in Eq. (18). If a correction is applied to offset the reheating effects on the gas, the 2.0 torr gas data will match with the theoretical curve. The axial temperature profiles of the gas mode explained in the next section also should be referred to understand this better.

3.4.3 Axial Temperature Profile

The steady-state axial temperature profiles of the LMHP for vacuum and gas modes are given in Figs. 21 and 22, respectively. The test conditions are indicated therein. The thermocouples 1 and 2 were damaged. In both modes, the profiles corresponding to input power range of 600-1600 W are plotted. The condenser power output as measured in the calorimeter is listed under Q_c . The heater temperature varied from 1021 K for the lowest Q_i to 1486 K for the highest Q_i while the hot zone operating temperature varied from 800 to 1000 K in both modes.

As expected, the condenser section profiles are distinctly different for vacuum and gas modes while the evaporator and transport profiles are similar. In the vacuum mode, the pipe is near-isothermal from end-to-end for Q_i greater than 800 W. A small drop in condenser-end



INACTIVE CONDENSER LENGTH ($L_p - L$) cm

Figure 20. Steady-State Inactive Condenser Length for Different Test Conditions.

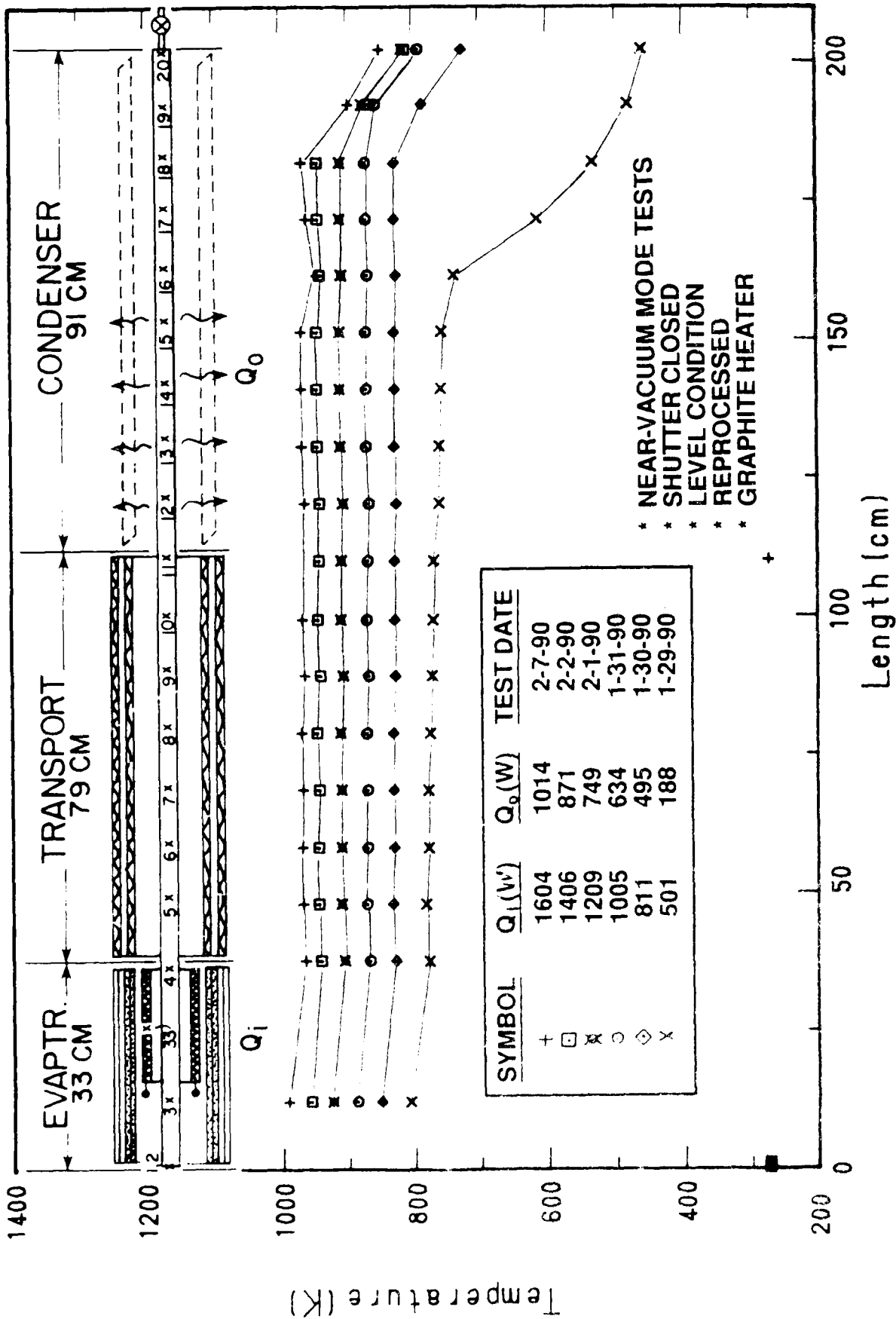


Figure 21. Steady-State Axial Temperature Profile (Vacuum Mode).

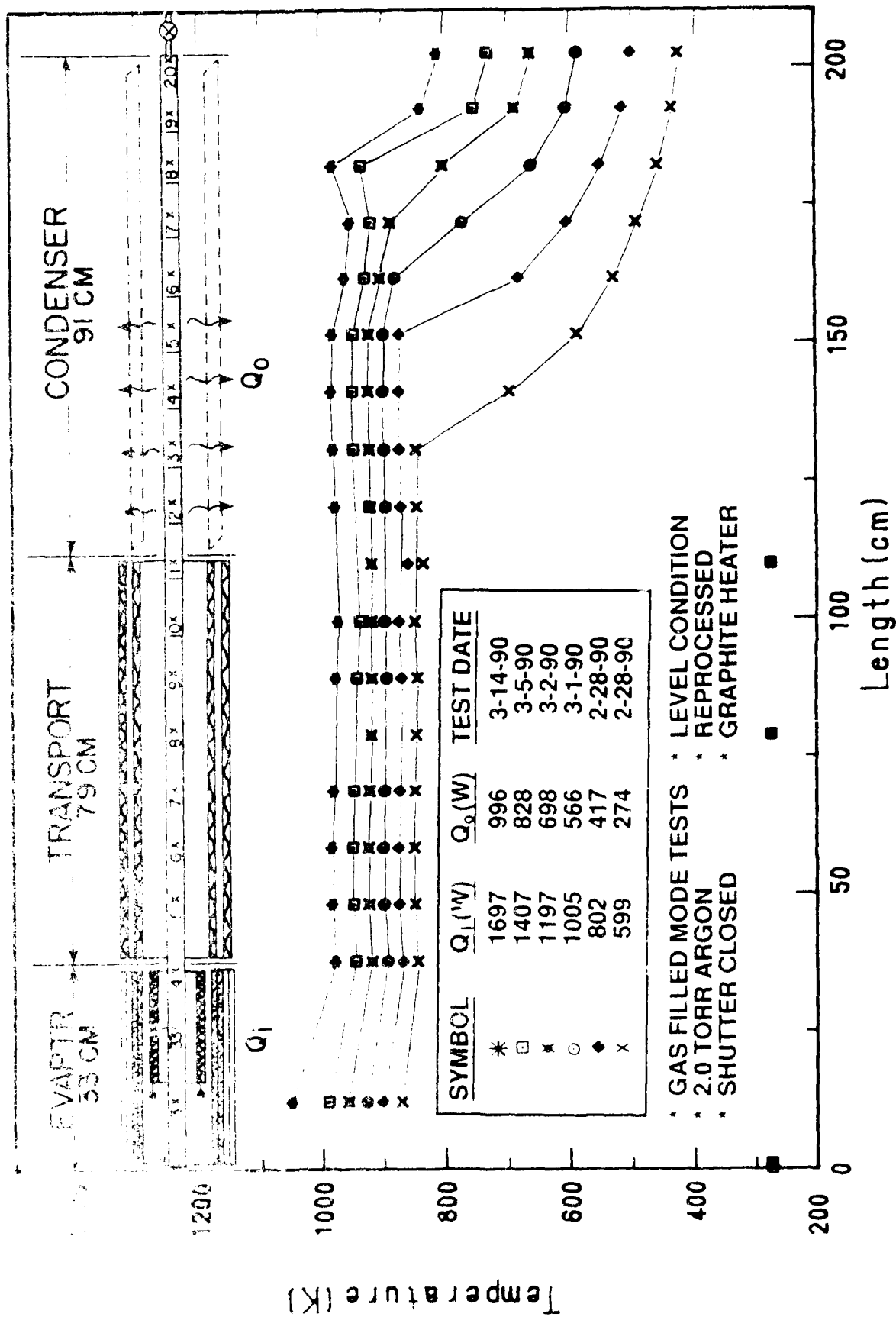


Figure 22. Steady-State Axial Temperature Profile (Gas-Filled Mode).

temperature is indicative of the presence of trace amounts of noncondensable gas or excess fluid. In the gas mode, the gas-blocked section is closely noticeable at all power levels. In normal circumstances, the condenser-end temperature should be close to the cold sink temperature. However, here it is seen to increase with the power input. The reason for this behavior is attributed to the closed condenser shutter which reradiated and heated the condenser end. The profiles for partially open shutter condition where the end temperatures were near 400 K had been reported in Ref. 30.

3.4.4 Temperature Gradient

The average hot zone temperature and the evaporator to adiabatic temperature gradient for both modes of the LMHP are plotted in Fig. 23. The points in this graph represent experimental data while the lines represent intuitive curve fit for the data. T_H for both modes vary linearly with transported power whereas ΔT_{EA} data vary nonlinearly. For the gas mode, the range of T_H is narrower than that for the vacuum mode and this is the expected behavior for a variable conductance heat pipe (VCHP) known for closer temperature control. The ΔT_{EA} behavior for the two modes in comparison is interesting to observe. The vacuum mode ΔT_{EA} curve is typical of the lean evaporator behavior, characteristic of the double wall wick wherein the temperature gradient decreases with increase in power. On the other hand, in the gas mode, the ΔT_{EA} increases with power which means that the evaporator wall superheat is increasing with temperature. The latter behavior is akin to the classical nucleate boiling phenomenon in the presence of noncondensable gas. The high ΔT_{EA} at higher Q_o in the gas mode is symptomatic of an impending evaporator dryout. The trend of the ΔT_{EA} curve indicates that a gas-loaded pipe might fail at lower power levels than a conventional pipe. However, the influence of the gas on the evaporator dryout has to be studied thoroughly before any quantitative conclusion can be reached.

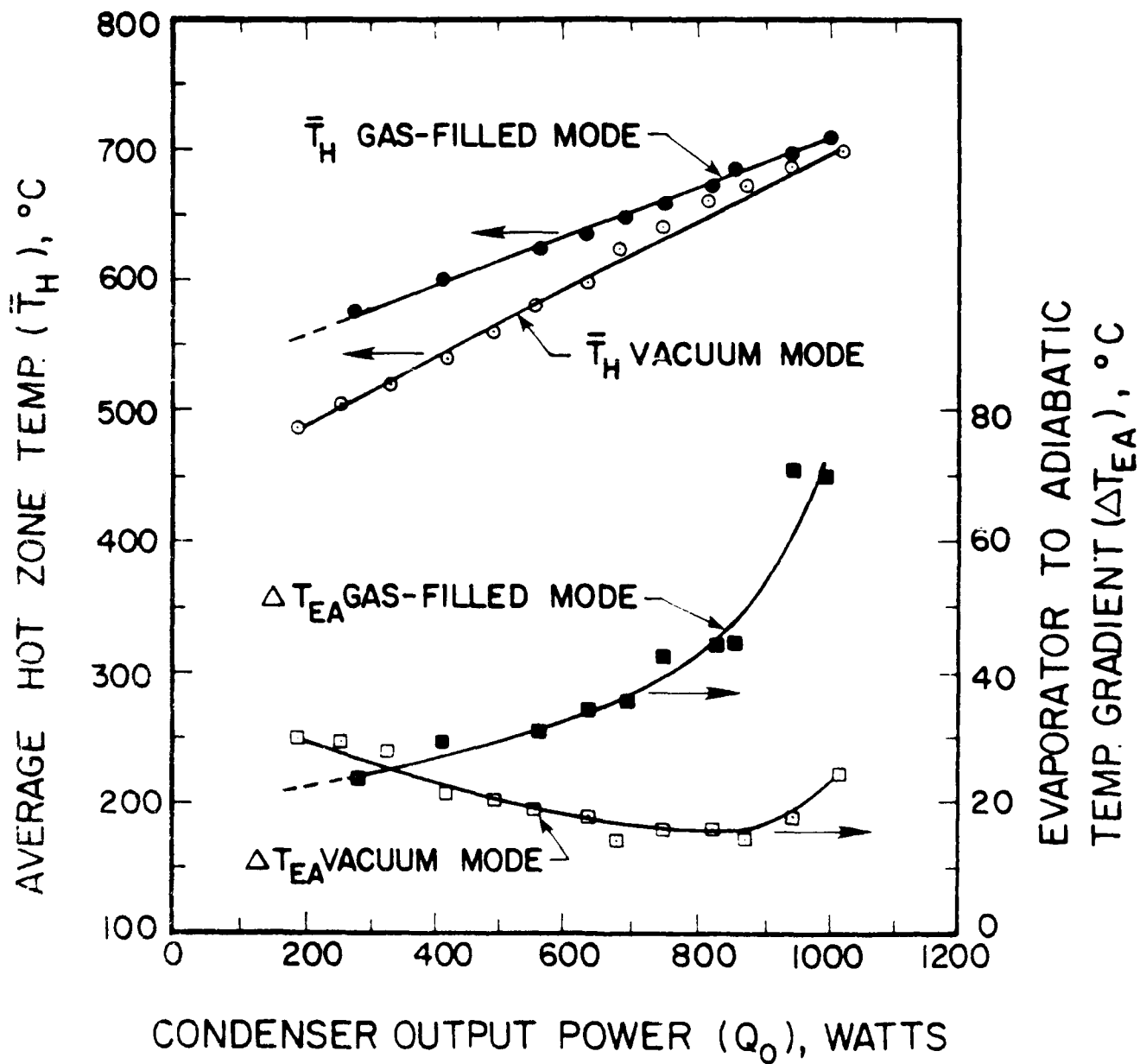


Figure 23. Average Hot Zone Temperature and Temperature Gradient.

3.4.5 Frozen Startup Behavior

Successful Startup: The LMHP was tested under identical test configuration and test procedure for both vacuum and gas modes. The vacuum mode tests preceded the gas mode. The startup tests from frozen state were started when the pipe was at room temperature (20°C) by suddenly applying the desired power to the evaporator heater and maintaining it at the same level throughout the test duration (about 2 to 3 hours). The transient behavior of the pipe was monitored by recording the temperature at all the axial locations for every minute.

The results are presented in the form of axial and transient temperature profiles. Tests were done at 100-W power increments, from 600 W to 1200 W of suddenly applied evaporator power input. Figures 24 and 25 show the 600 W vacuum mode plots in the forms of axial temperature profile for specified time and transient temperature profile at specified axial location, respectively. Figures 26 and 27 show the corresponding 600-W gas-filled mode behavior. As seen from Figs. 24 and 26, in 20 minutes the hot vapor front has propagated to the condenser region in vacuum mode while the front has crossed only the mid-section of the adiabatic in gas mode. At 150 minutes, the hot front has moved to 170 cm in vacuum mode while it has moved to 130 cm in gas mode. It is clear from Fig. 25 that the startup was not smooth in vacuum mode since T.C. (thermocouples (#3 and #33 (heater))) experienced sudden high temperature spikes at 2000 sec after power-on. This is a temporary crisis of wall superheat at the evaporator end, if not self-corrected, could lead to evaporator burnout. In contrast, the gas mode startup was smooth (Fig. 27) since T.C. #3 and #33 did not experience any surge.

Similarly, the results of the frozen startup tests with 700, 800, 900, and 1000 W input for vacuum and gas modes are presented in Figs. 28 through 43. As in 600 W case, the startup in the vacuum mode was rough while that in the gas mode was smooth for all the cases. However, a small hump is noticeable in Fig. 43 for T.C. #33 at 900 sec indicating a temporary crisis. For 1100 W input case (plot not shown), T.C. #3 also showed a 100 K spike which forewarned a startup trouble even for the gas-filled mode.

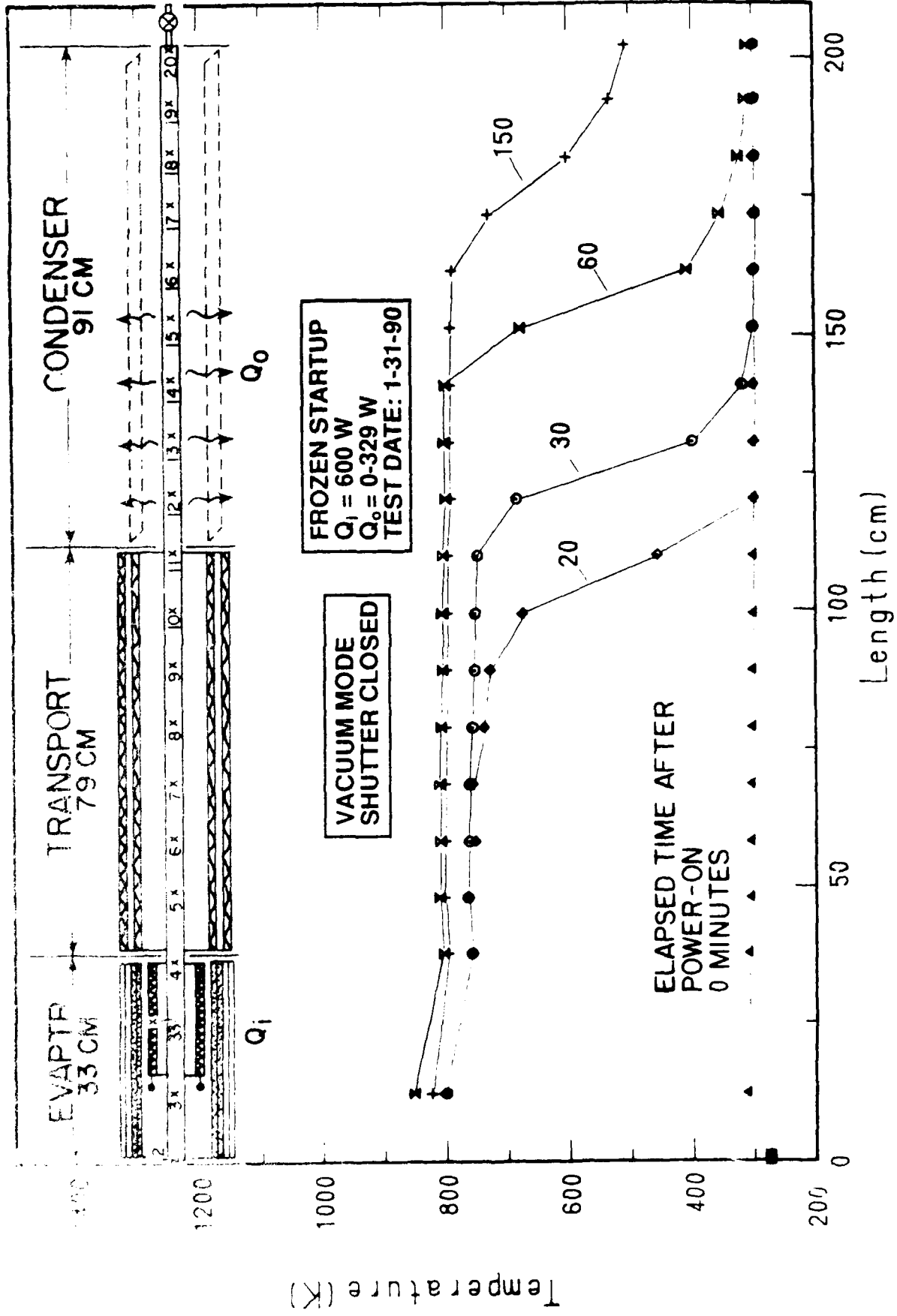


Figure 24. Axial Temperature Profile at Specified Time from 0-150 Minutes After Power Input ($Q_1 = 600$ W; Vacuum Mode).

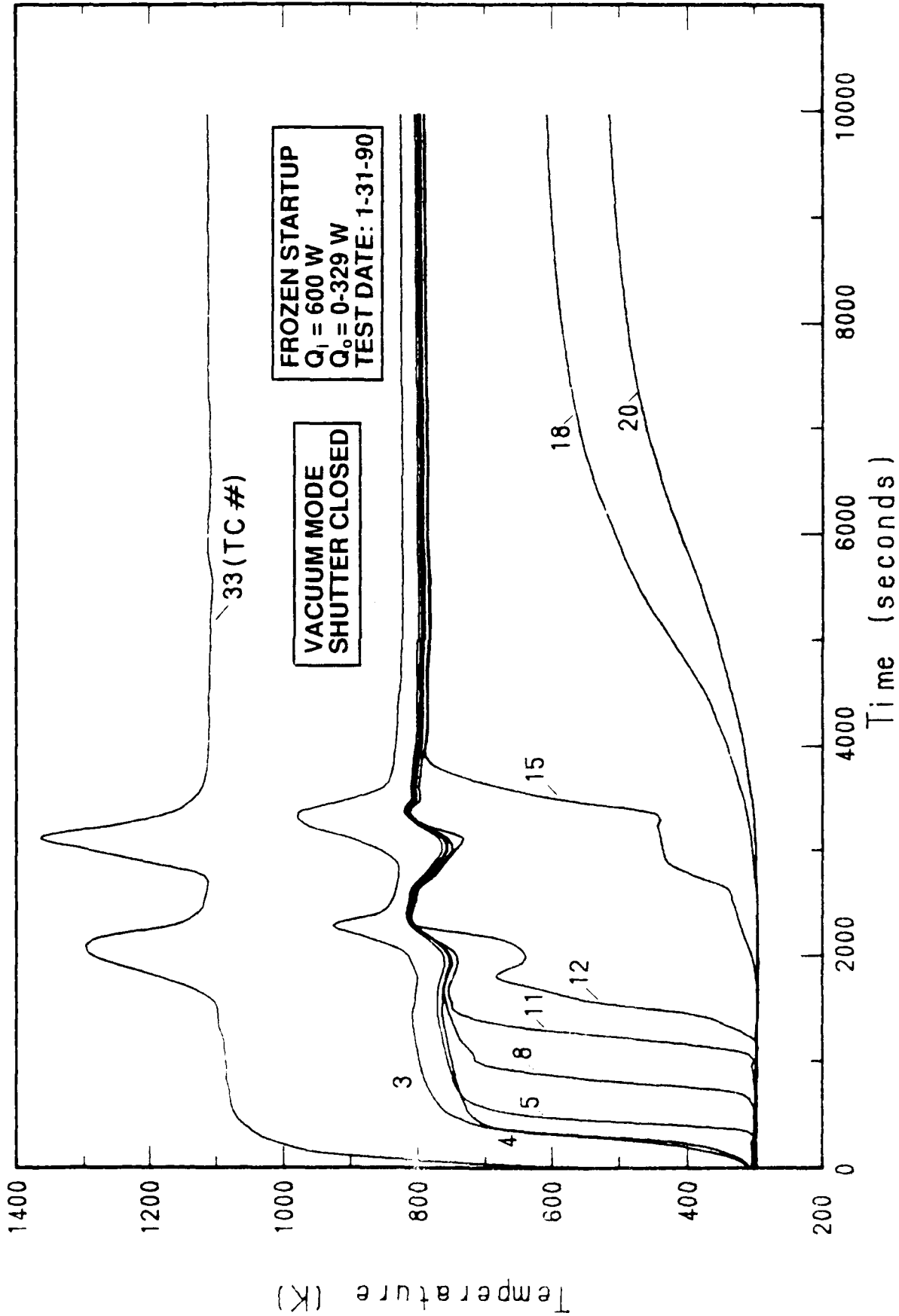
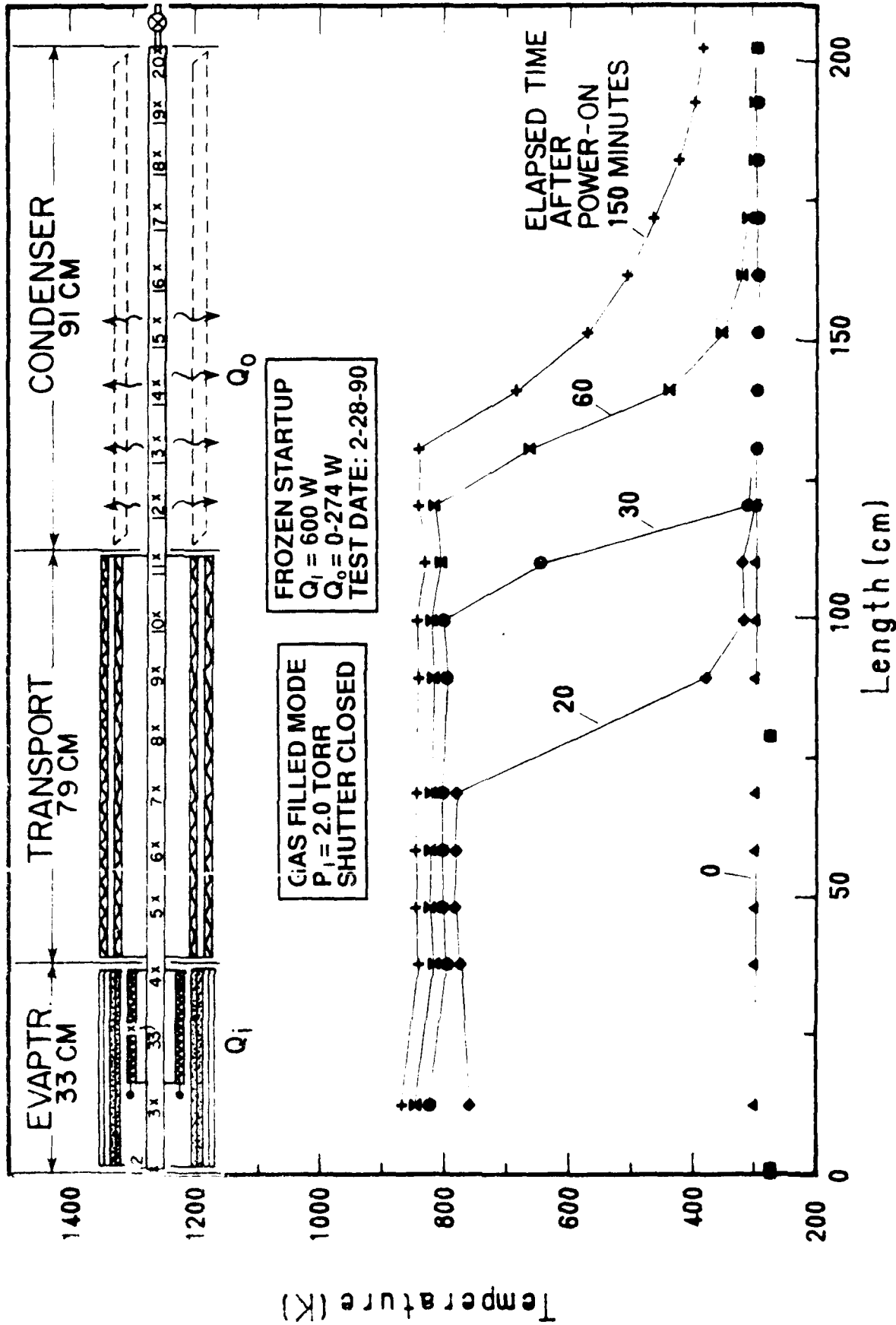


Figure 25. Transient Temperature Profile at Specified Axial Locations ($Q_1 = 600$ W; Vacuum Mode).



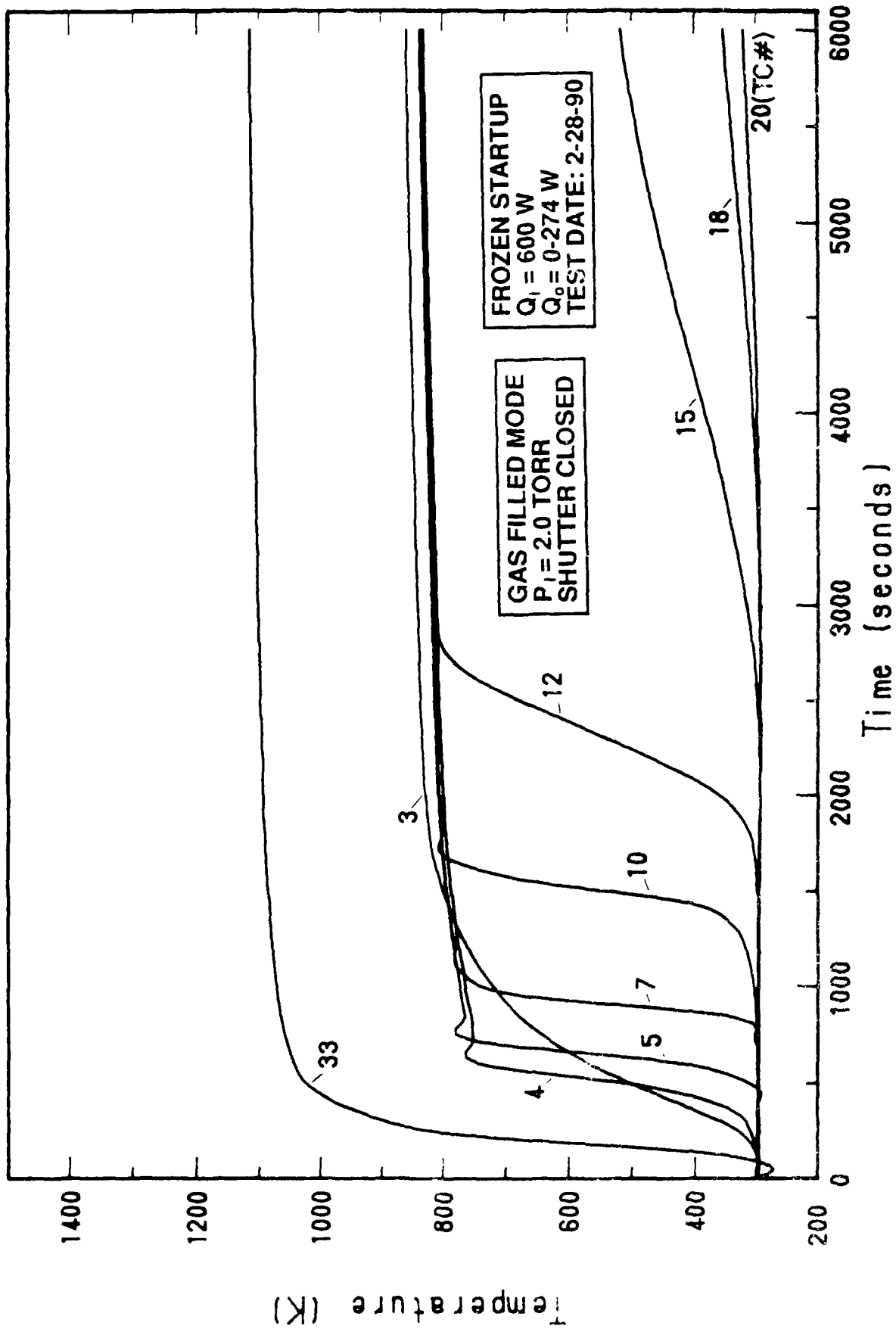


Figure 27. Transient Temperature Profile at Specified Axial Locations ($Q_1 = 600$ W; Gas-Filled Mode).

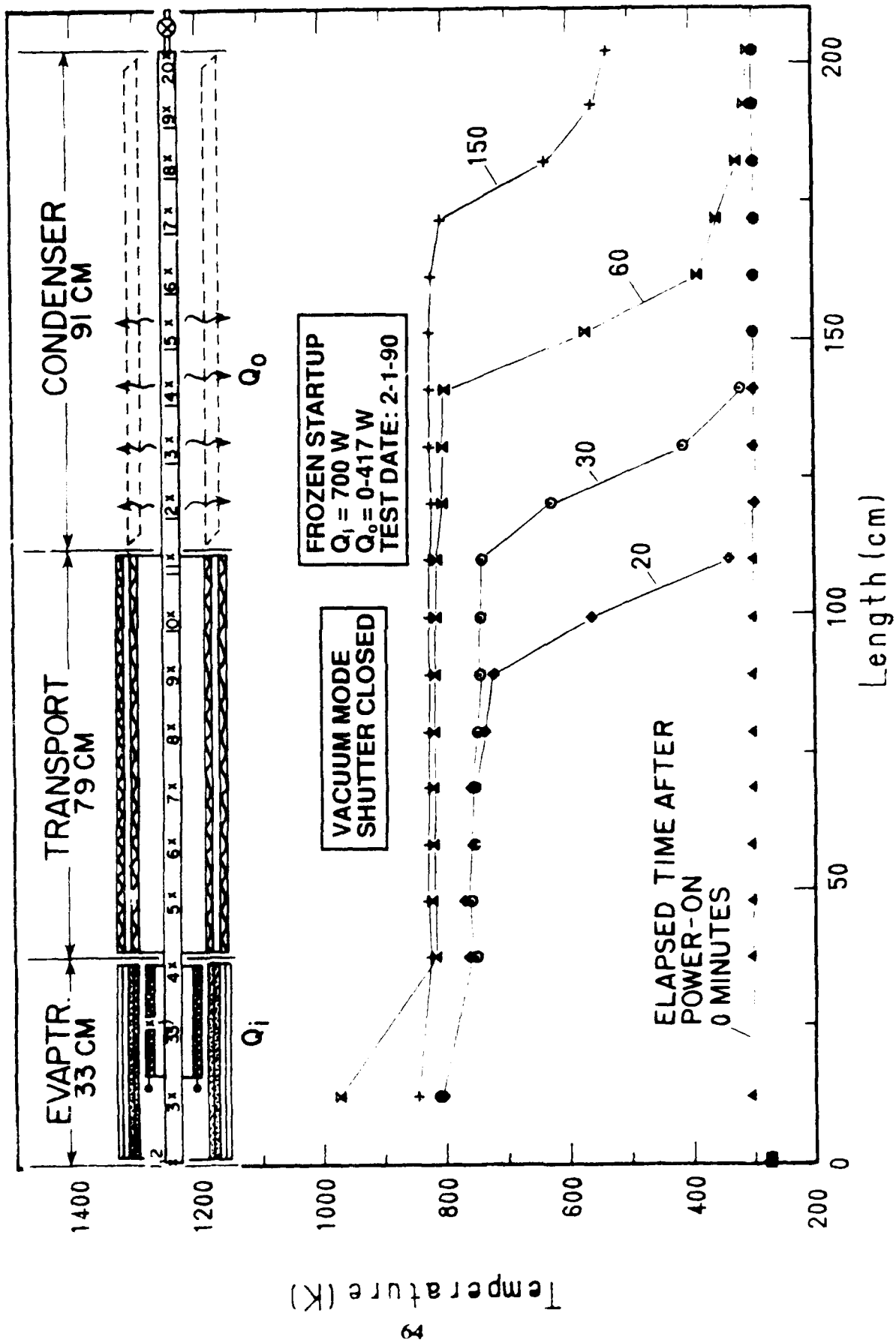


Figure 28. Axial Temperature Profile at Specified Time from 0 150 Minutes After Power Input ($Q_1 = 700 \text{ W}$; Vacuum Mode).

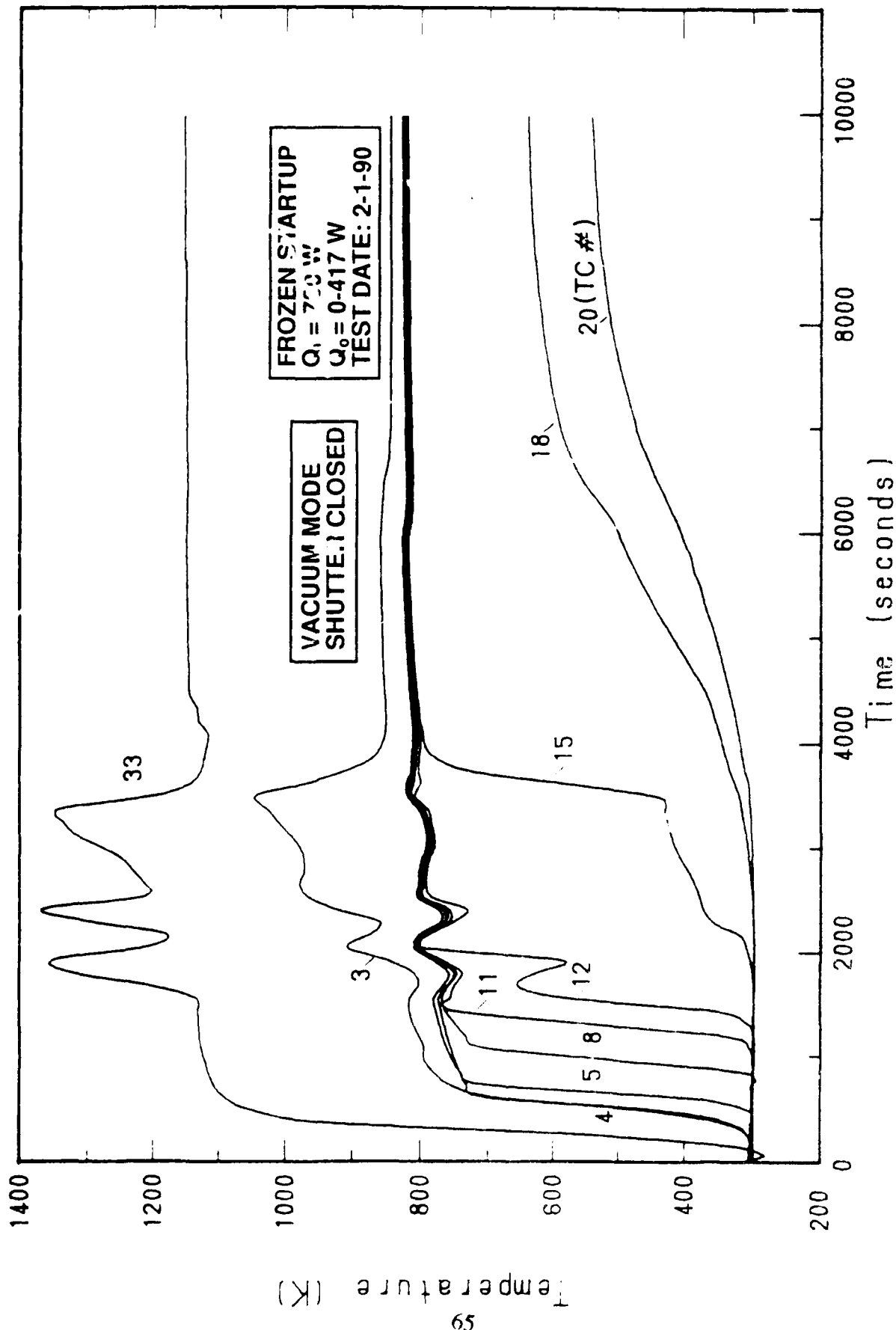


Figure 29. Transient Temperature Profile at Specified Axial Locations ($Q_1 = 700$ W; Vacuum Mode).

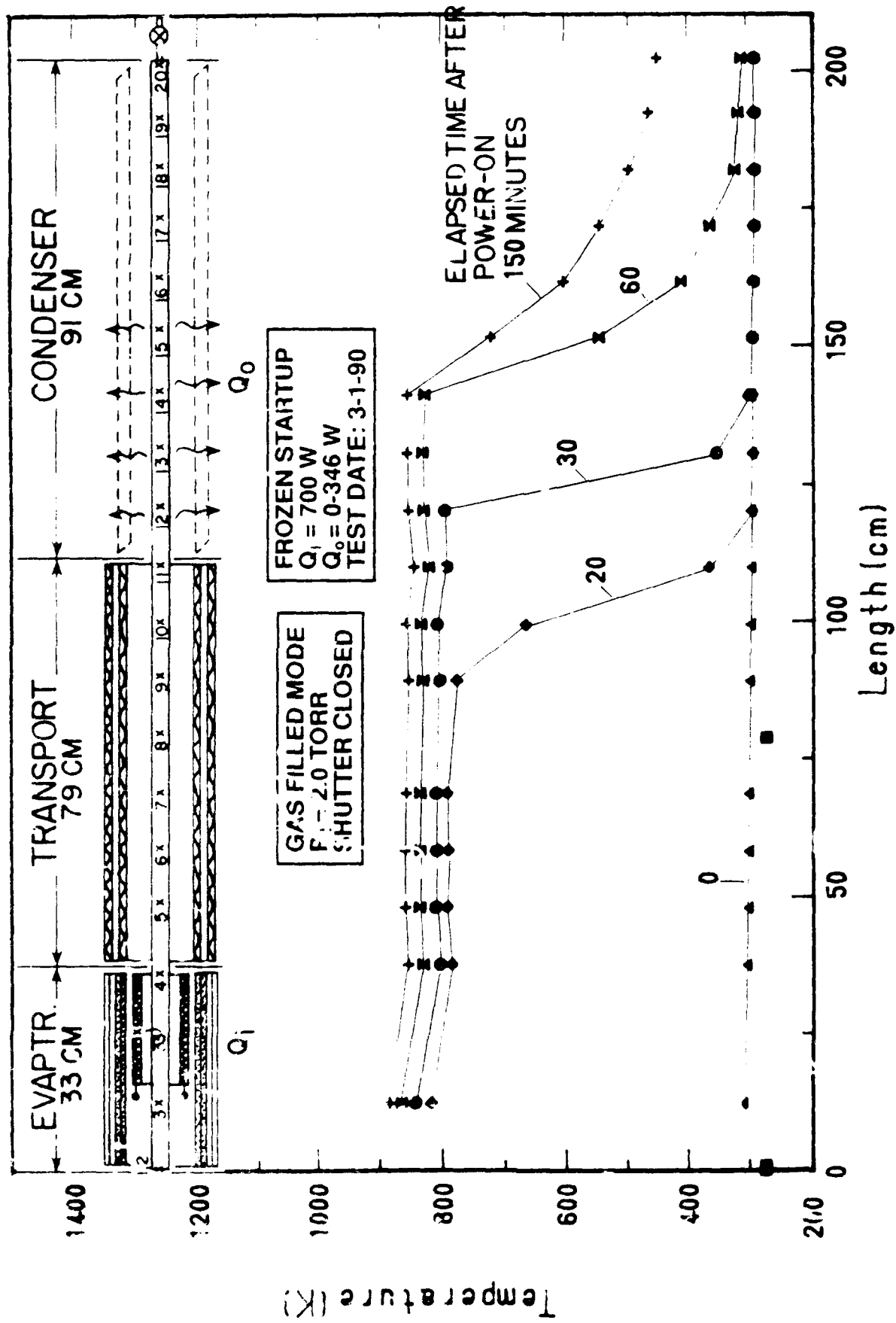


Figure 30. Axial Temperature Profile at Specified Time from 0-150 Minutes After Power Input ($Q_i = 700$ W; Gas-Filled Mode).

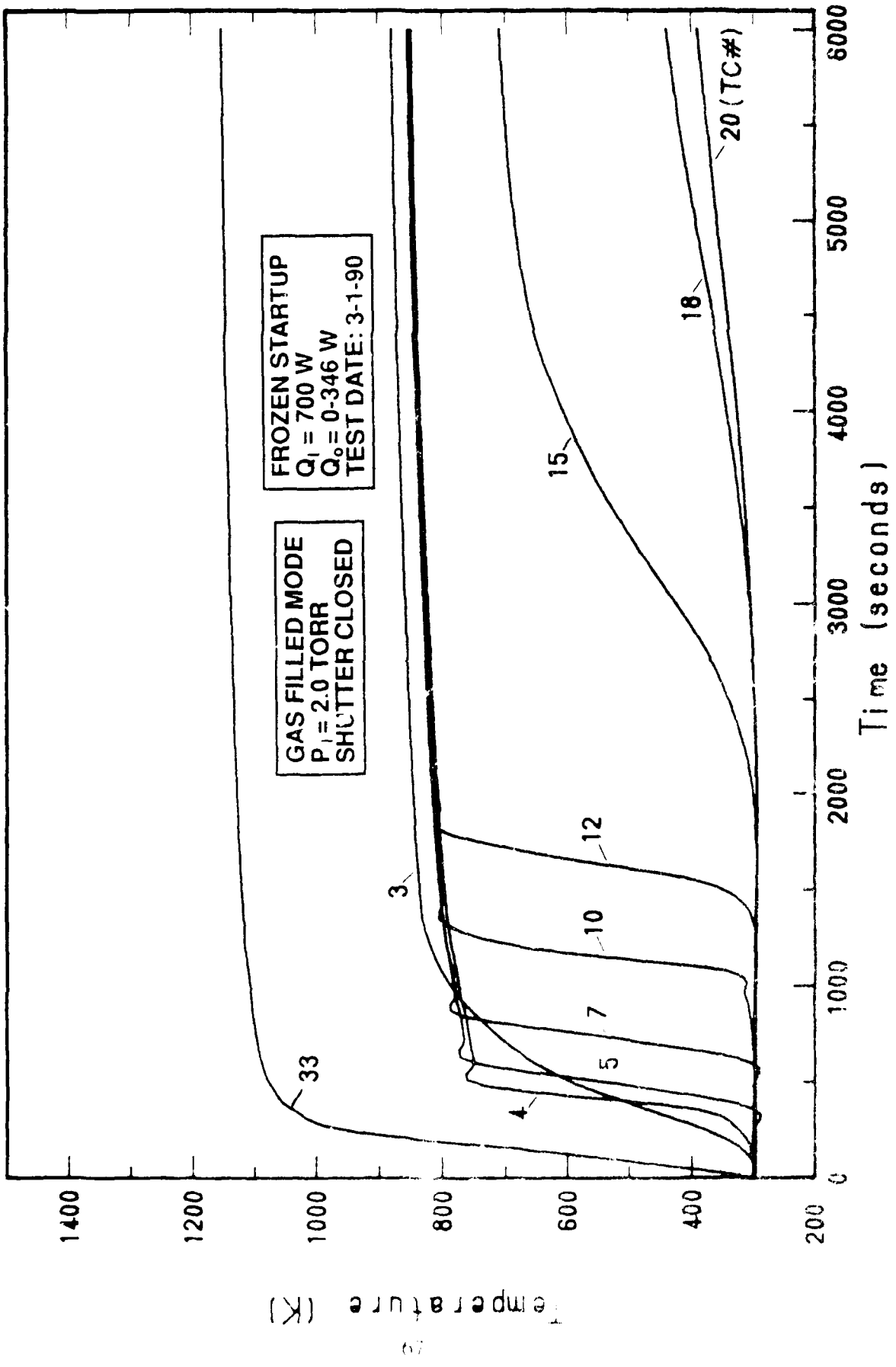


Figure 34. Transient Temperature Profile at Specified Axial Locations ($Q_1 = 700$ W; Gas Filled Mode).

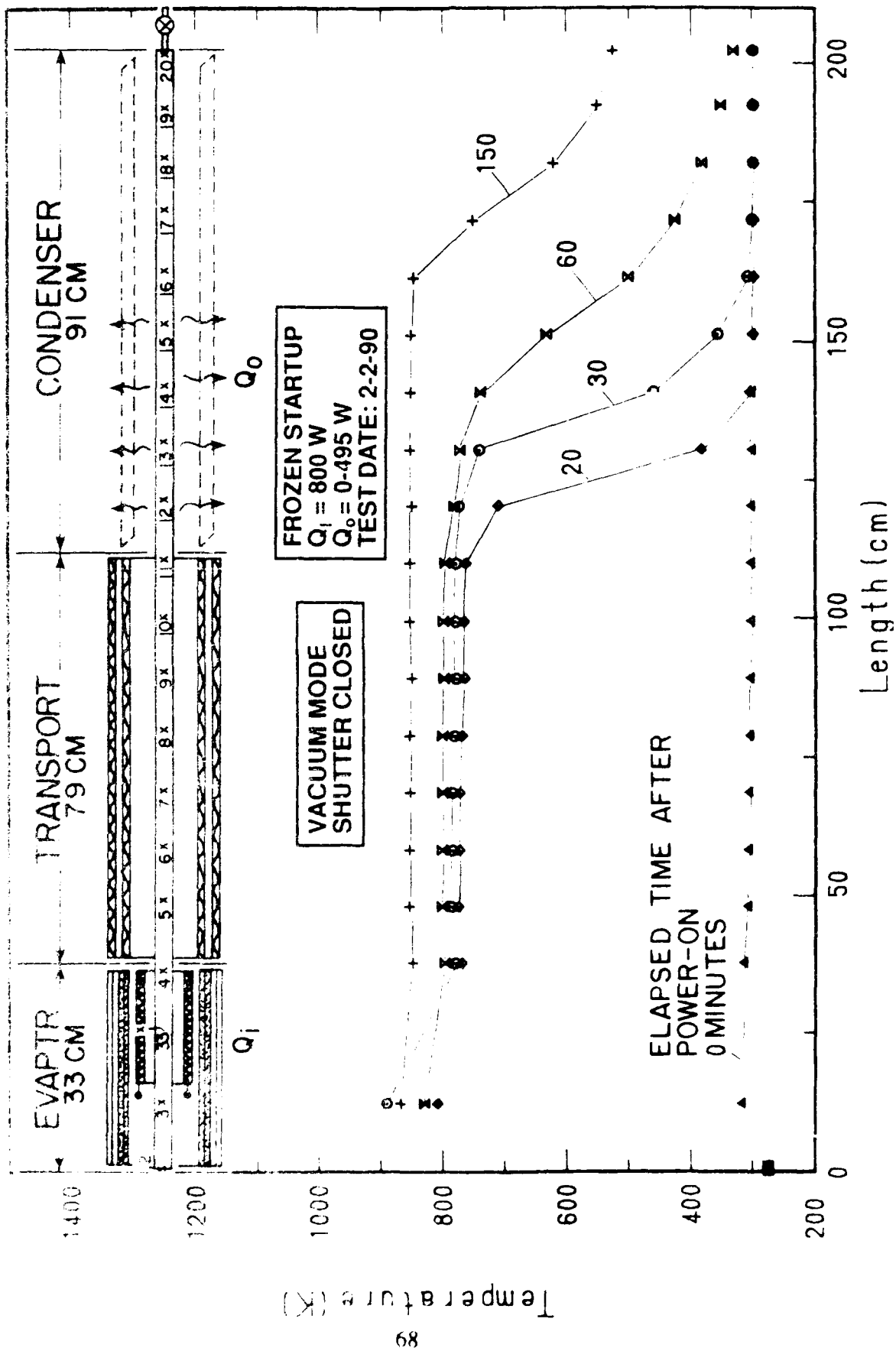


Figure 32. Axial Temperature Profile at Specified Time from 0-150 Minutes After Power Input ($Q_1 = 800 \text{ W}$; Vacuum Mode).

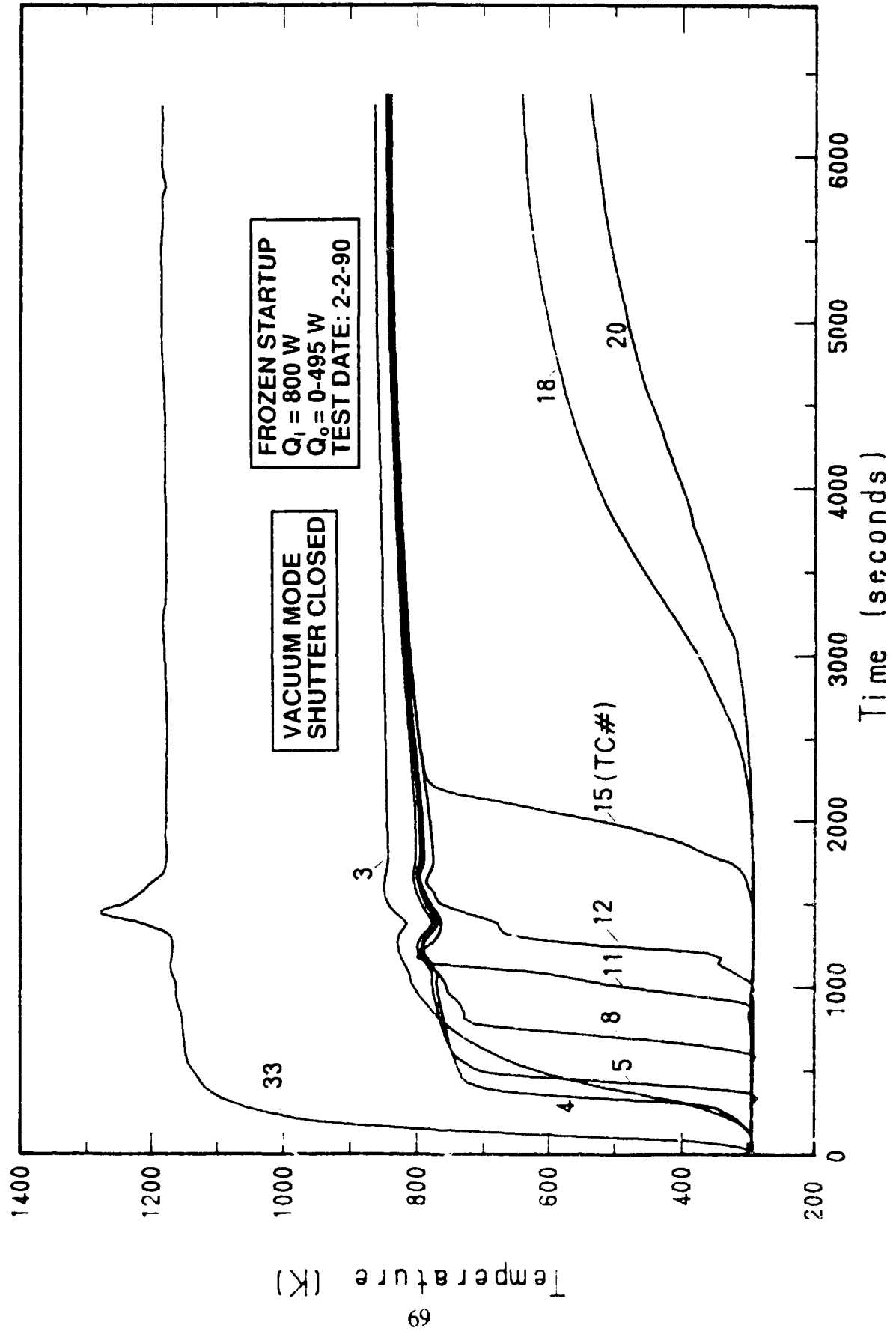


Figure 33. Transient Temperature Profile at Specified Axial Locations ($Q_1 = 800 \text{ W}$; Vacuum Mode).

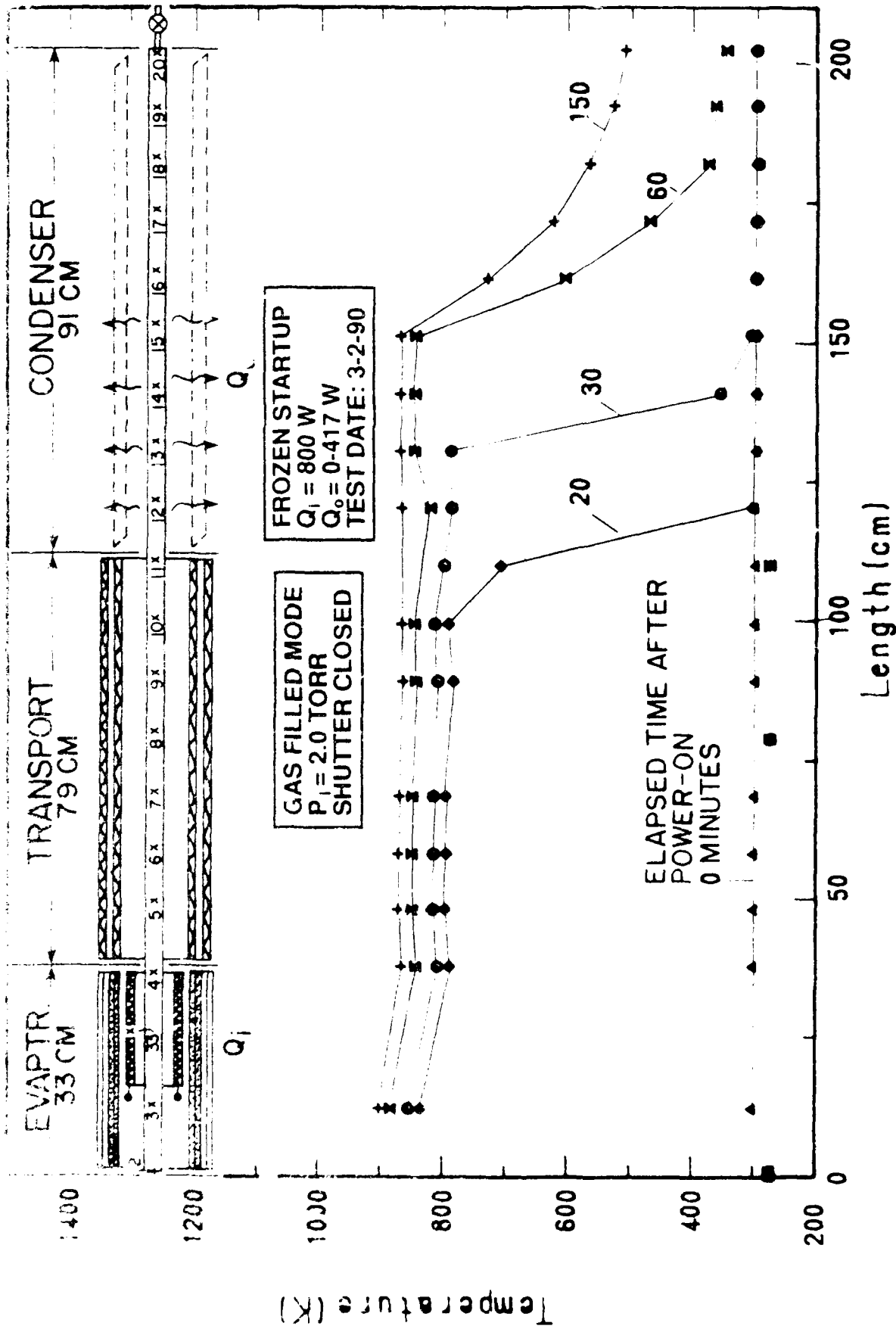


Figure 34. Axial Temperature Profile at Specified Time from 0-150 Minutes After Power Input ($Q_c = 800$ W; Gas-Filled Mode).

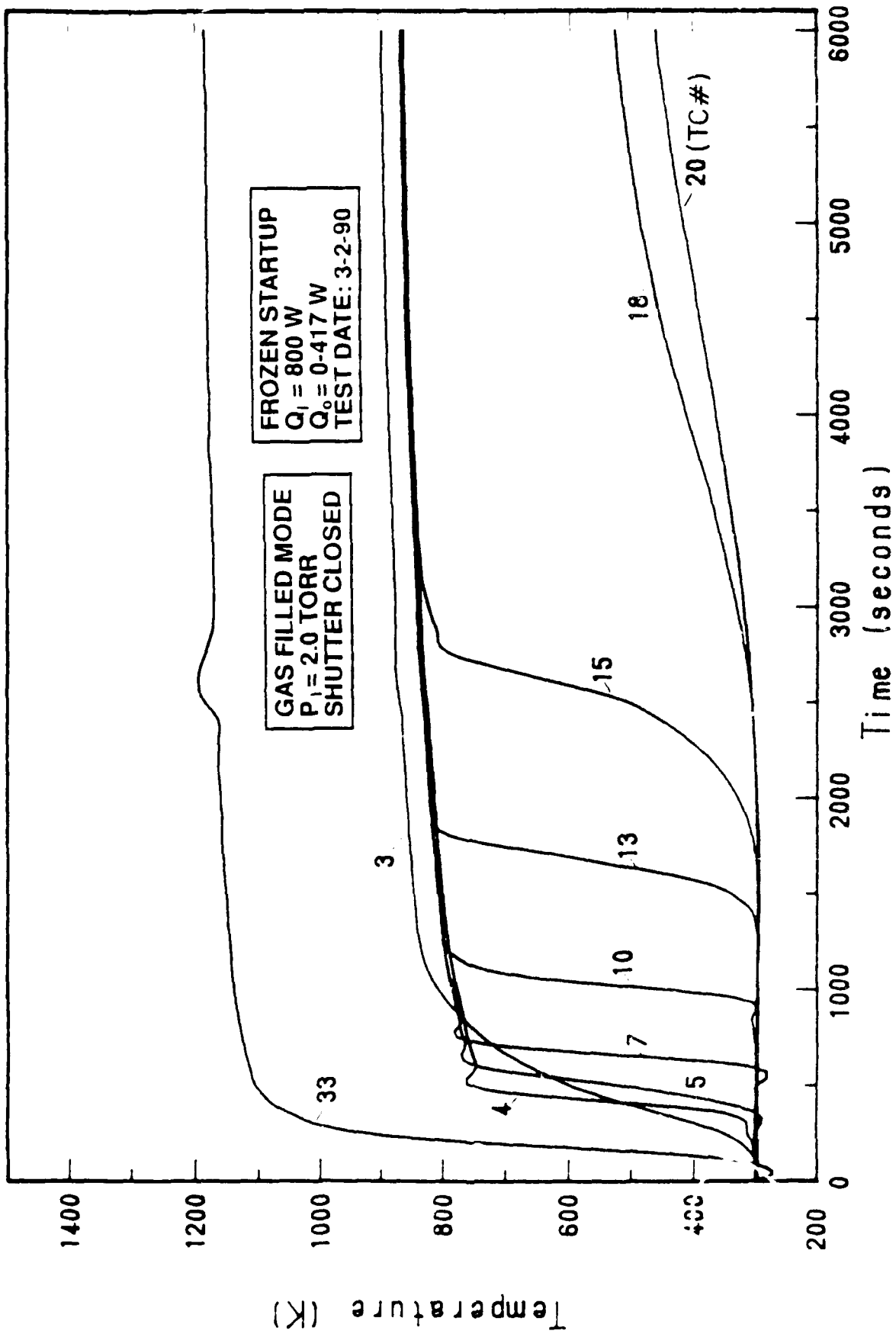


Figure 35. Transient Temperature Profile at Specified Axial Locations ($Q_1 = 800$ W; Gas-Filled Mode).

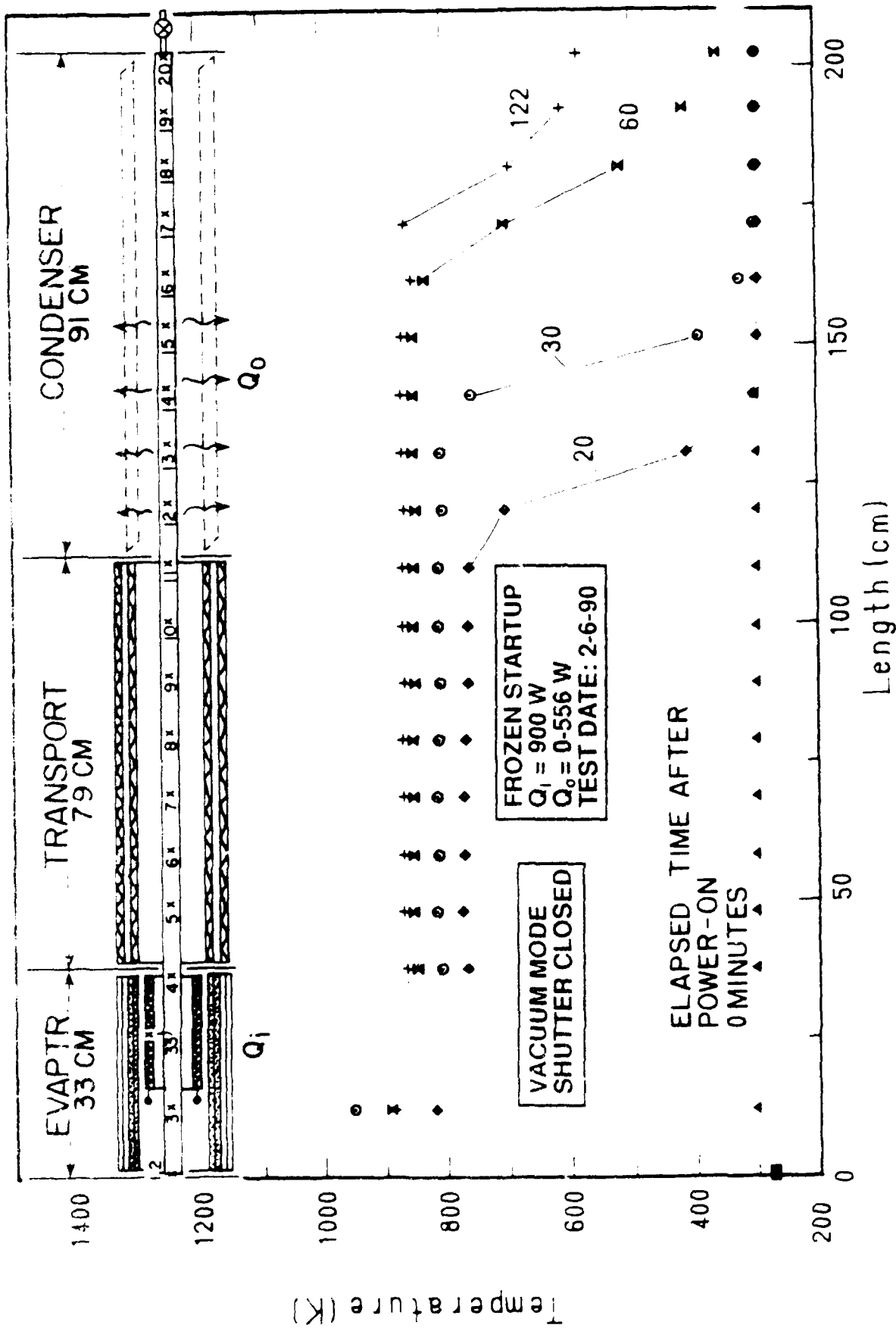


Figure 36. Axial Temperature Profile at Specified Time from 0-150 Minutes After Power Input ($Q_i = 900 \text{ W}$; Vacuum Mode).

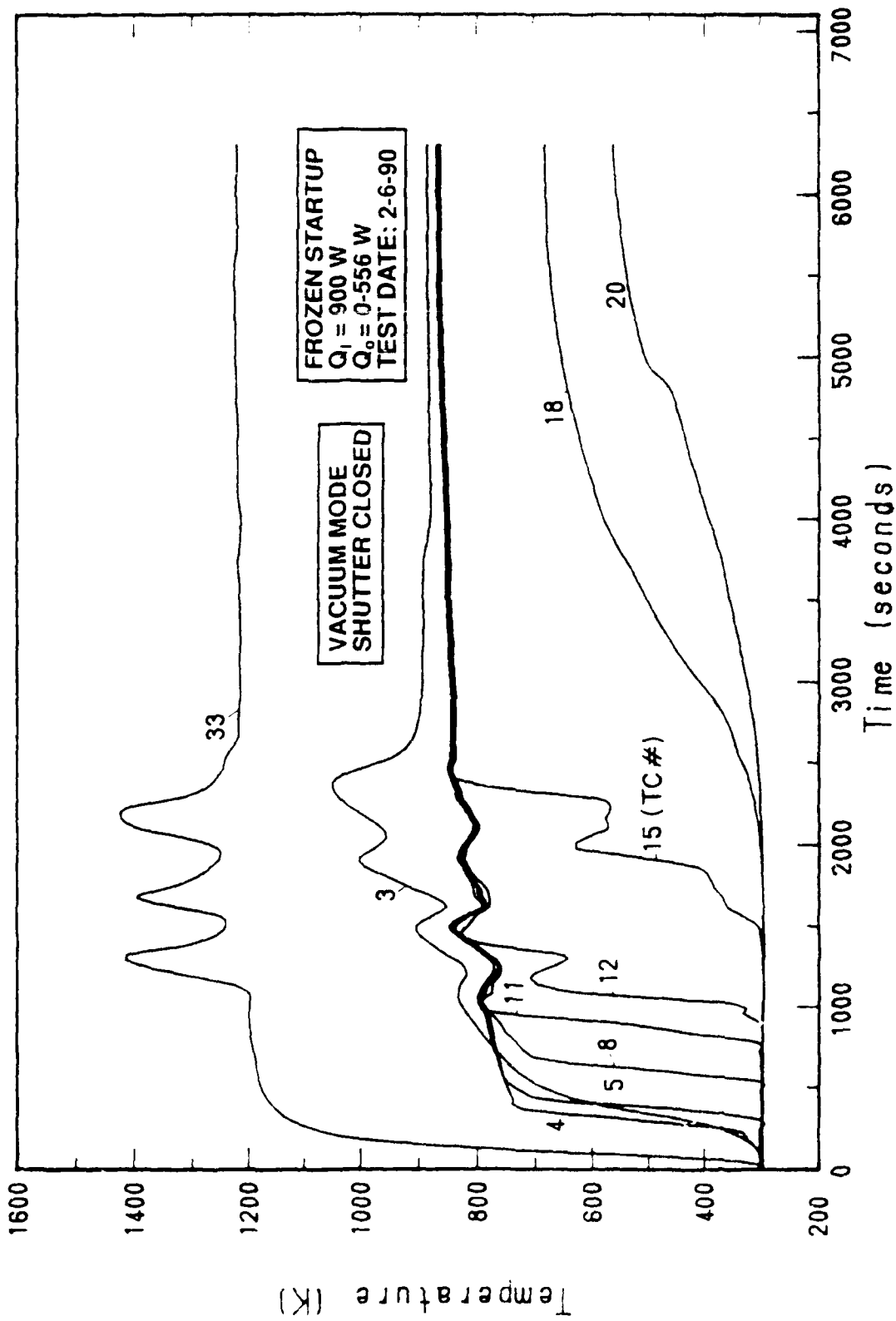


Figure 37. Transient Temperature Profile at Specified Axial Locations ($Q_1 = 900$ W; Vacuum Mode).

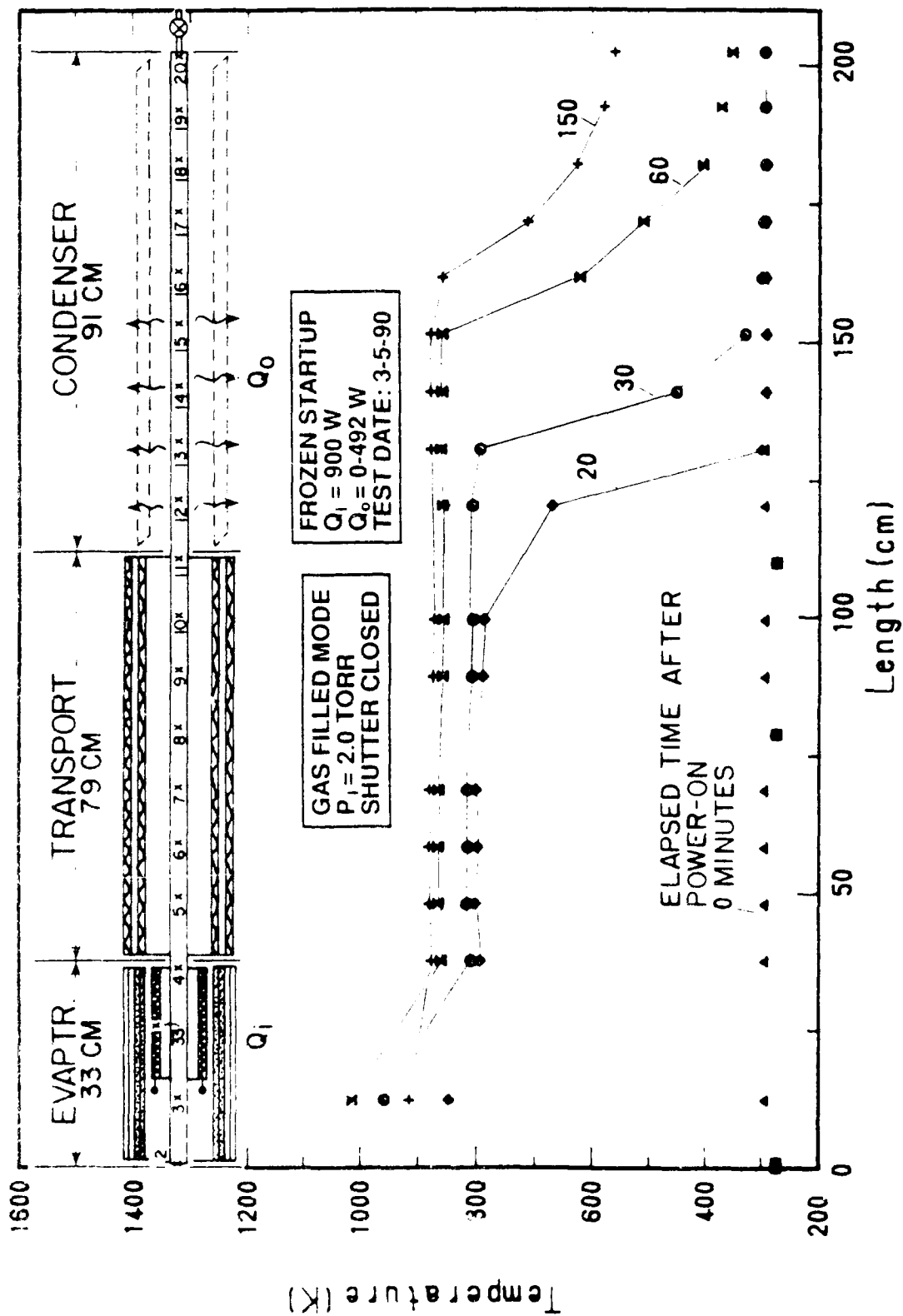


Figure 38. Axial Temperature Profile at Specified Time from 0-150 Minutes After Power Input ($Q_i = 900$ W; Gas-Filled Mode).

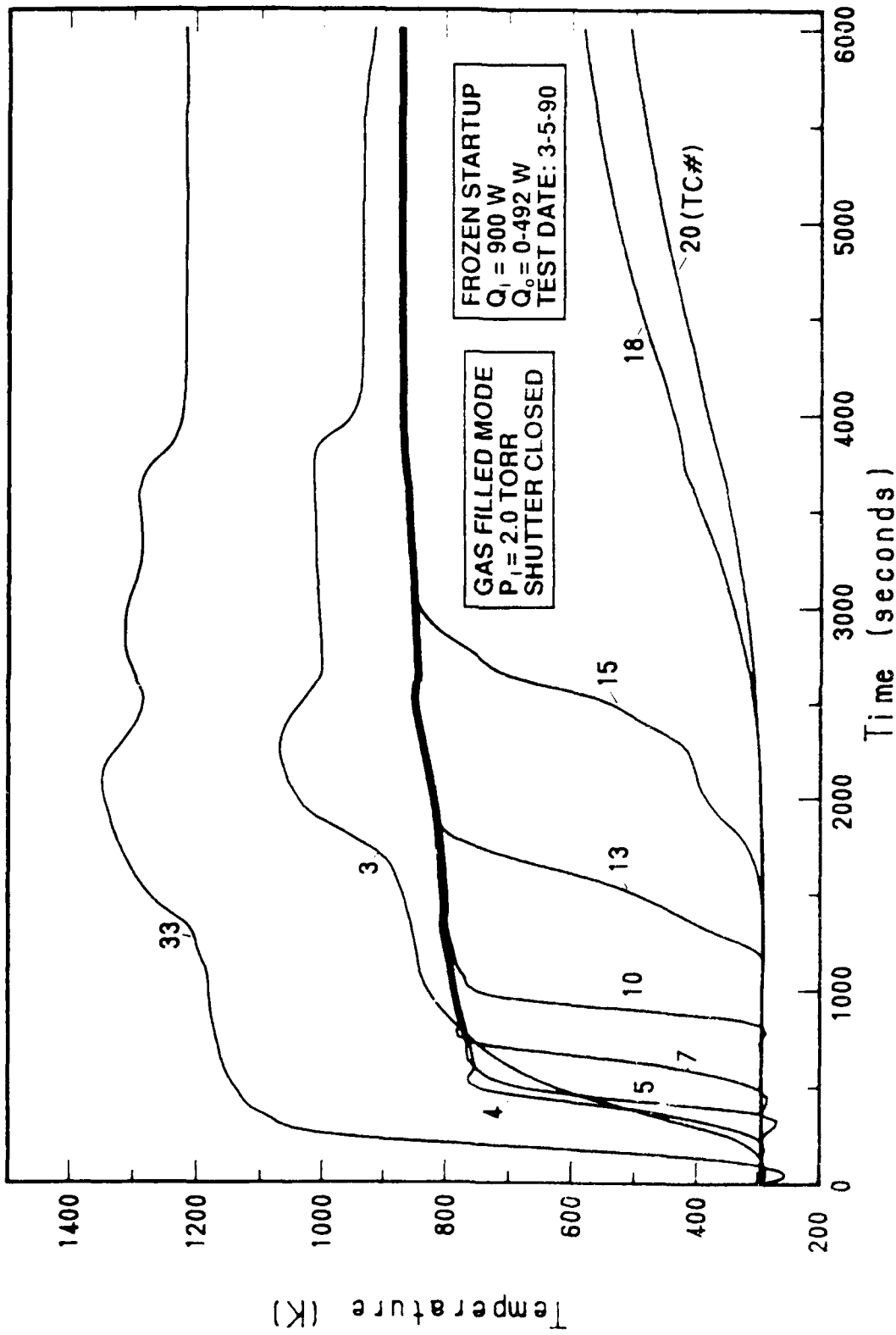


Figure 39. Transient Temperature Profile at Specified Axial Locations ($Q_1 = 900$ W; Gas-Filled Mode).

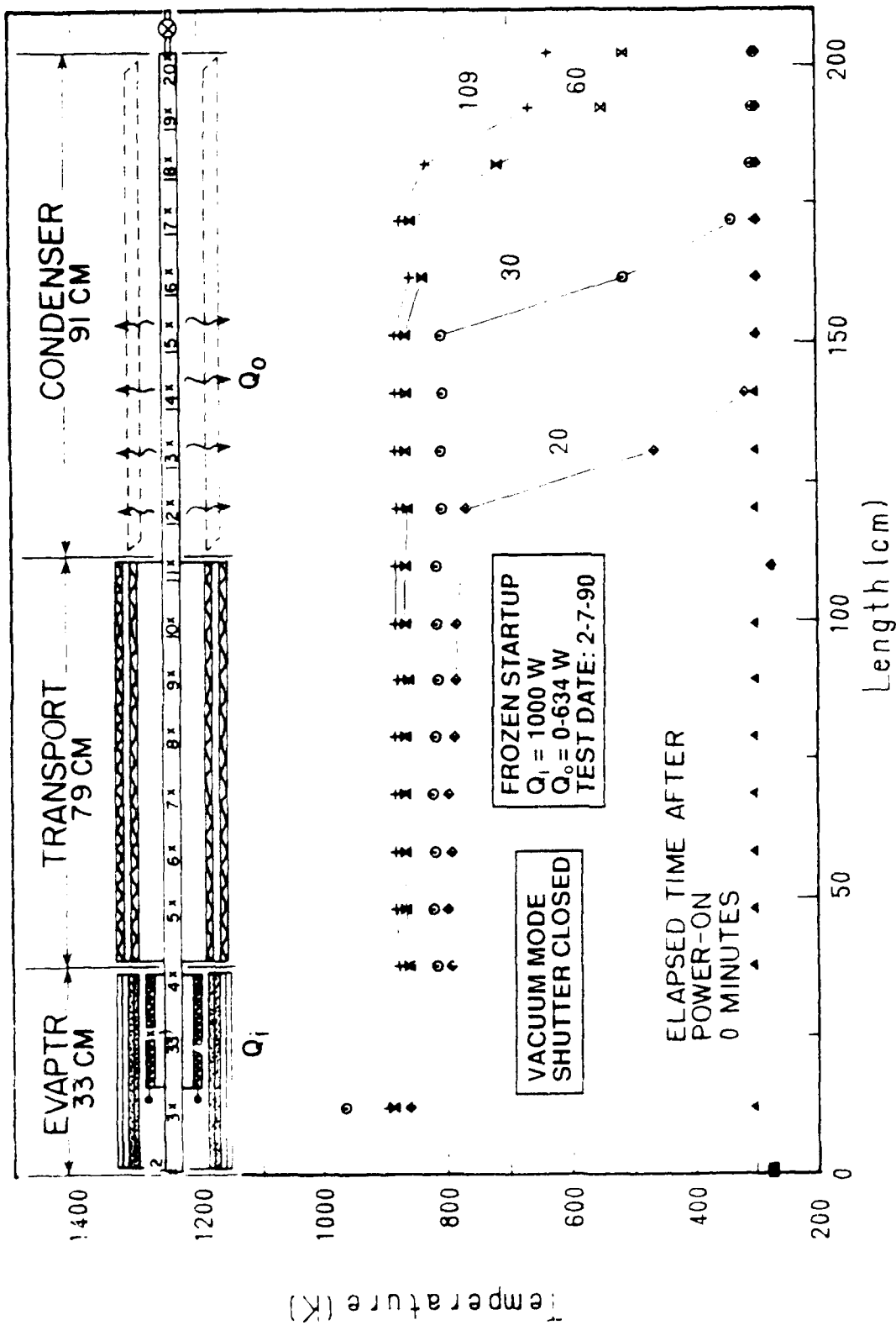


Figure 40. Axial Temperature Profile at Specified Time from 0-150 Minutes After Power Input ($Q_1 = 1000 \text{ W}$; Vacuum Mode).

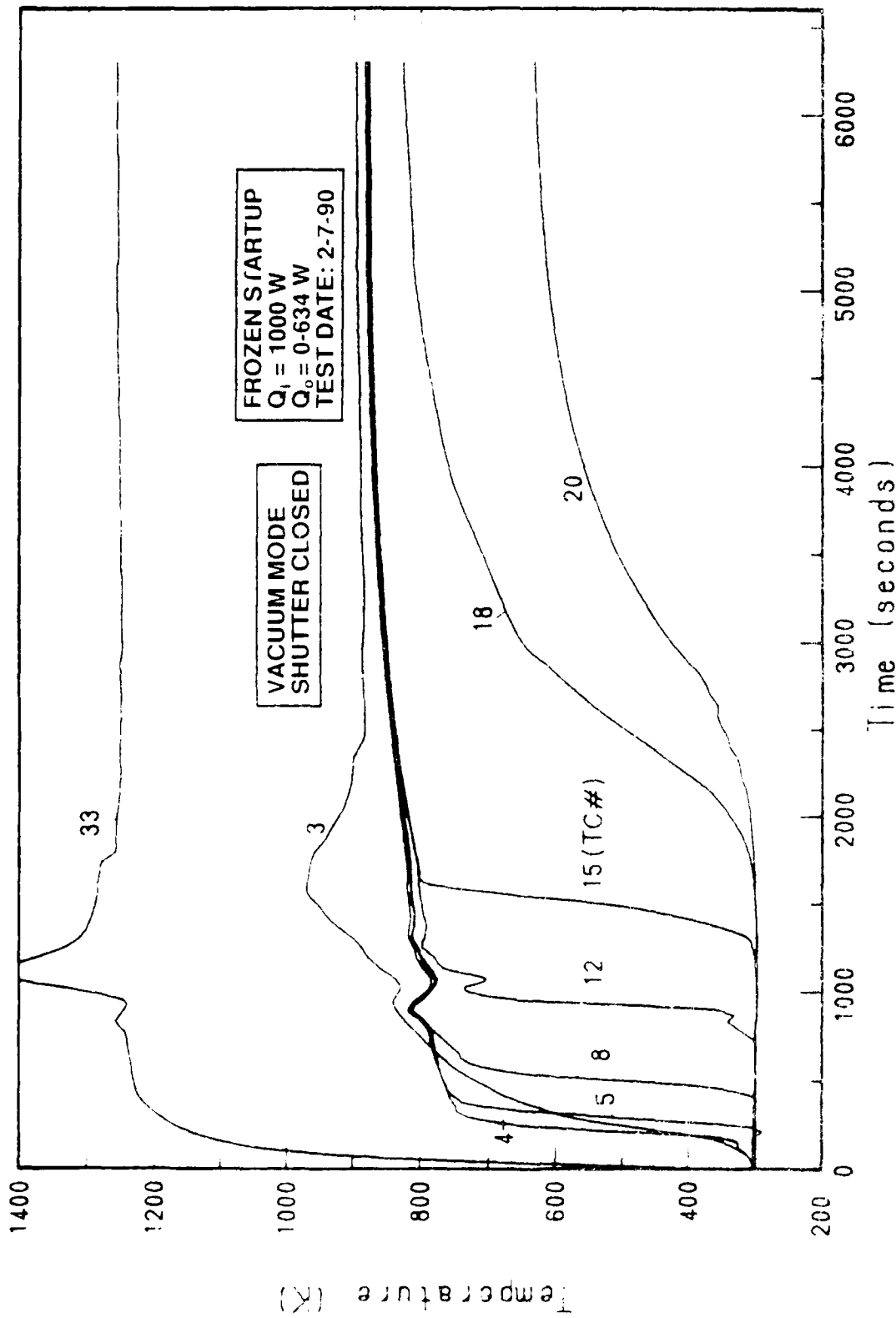


Figure 41. Transient Temperature Profile at Specified Axial Locations ($Q_1 = 1000$ W; Vacuum Mode).

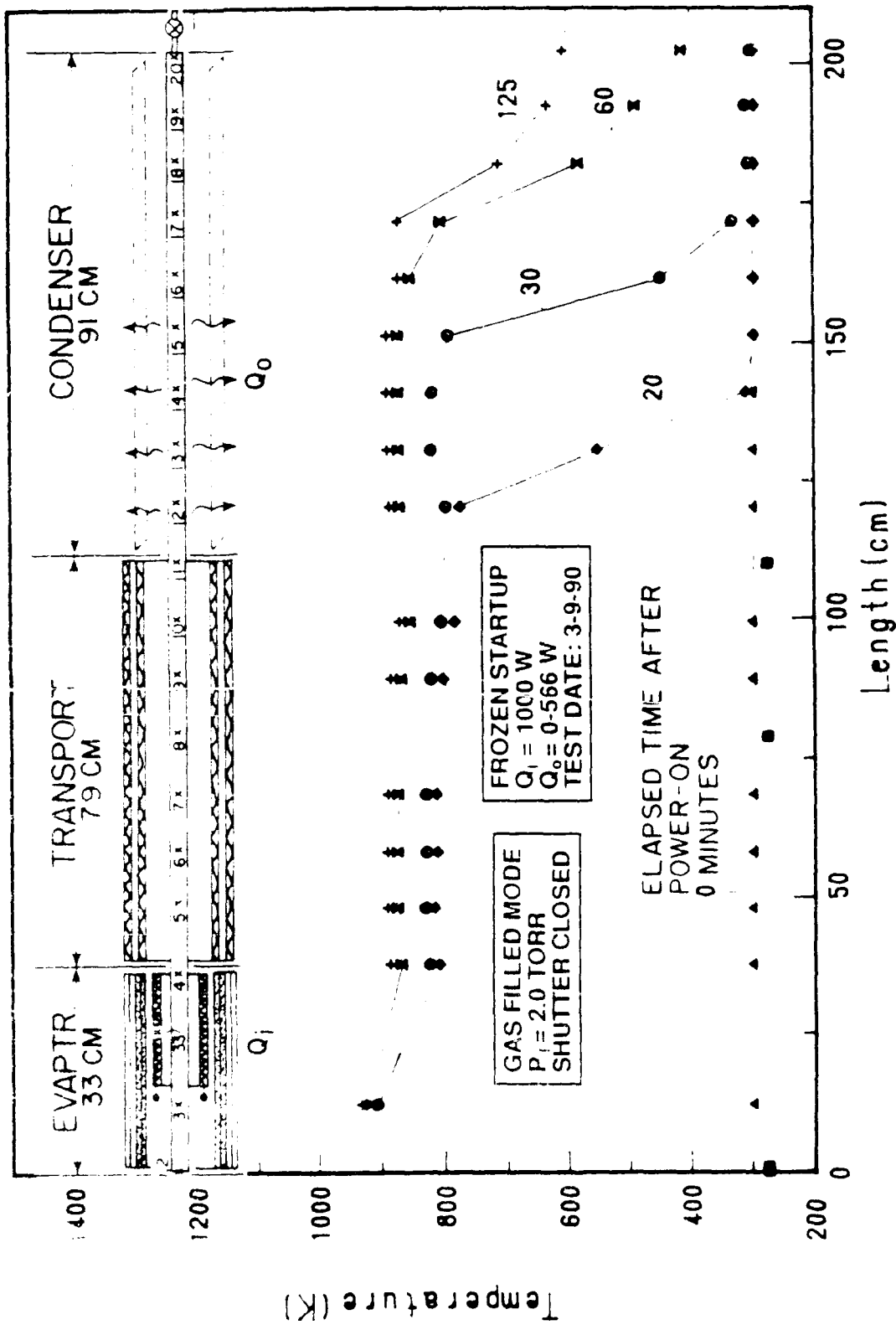


Figure 42. Axial Temperature Profile at Specified Time from 0-150 Minutes After Power Input ($Q_i = 1000$ W; Gas-Filled Mode).

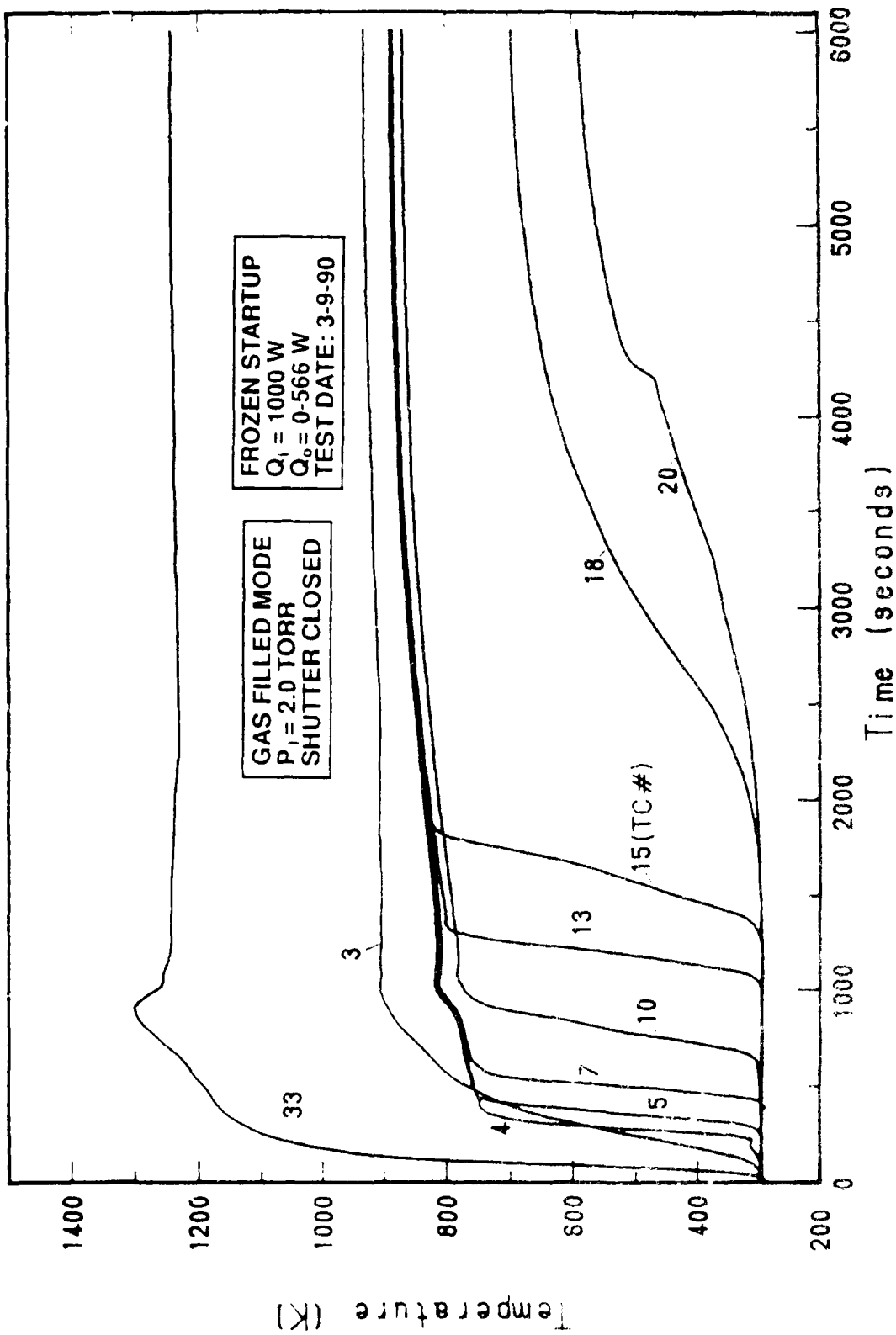


Figure 43. Transient Temperature Profile at Specified Axial Locations ($Q_1 = 1000 \text{ W}$; Gas-Filled Mode).

Other important information obtained from the transient temperature profiles is the comparison of the startup time for both modes. The heat pipe is supposed to have started successfully if the hot front has crossed T.C. #11 (adiabatic region). As seen from these figures, the vacuum mode startup times are shorter than those for the gas mode.

3.4.6 Liquid Startup Behavior

In order to verify the liquid startup behavior, the pipe was uniformly heated to nearly 200 ± 25 °C using both main and trace heaters for about 30 minutes. This was to make sure that there was no frozen slug of sodium anywhere inside the pipe and to ensure wick saturation with liquid. Then the startup test was started (just as the frozen startup) by applying the step power input to the main heater and switching the trace heater off. Figures 44 and 45 show the axial and transient temperature profiles of the liquid startup for the vacuum mode. Similarly, Figures 46 and 47 show those of gas-filled mode. A power input of 1200 W was chosen as the power level at which the frozen startups failed. As can be seen in these figures, the startups were smooth in both the cases as expected.

3.4.7 Startup Failure

The input power was increased to 1200 W after successful startup with 1100 W in gas mode. But this time the temperatures of T.C. #3 and #33 kept rising until the alarm limits were reached. This test was repeated several times with the same outcome. Hence, it was concluded that 1100 W was the maximum limit this LMHP could be started from frozen state successfully. Figure 48 shows the startup failure in both modes for 1200 W input.

3.4.8 Transient Input Power and Evaporator Temperature Variation

There were certain doubts about the stability of the input power during the startup tests. Due to the resistance variation of the heater element with temperature, it was necessary to manually control the input power until the temperature of the heater stabilized. Unfortunately,

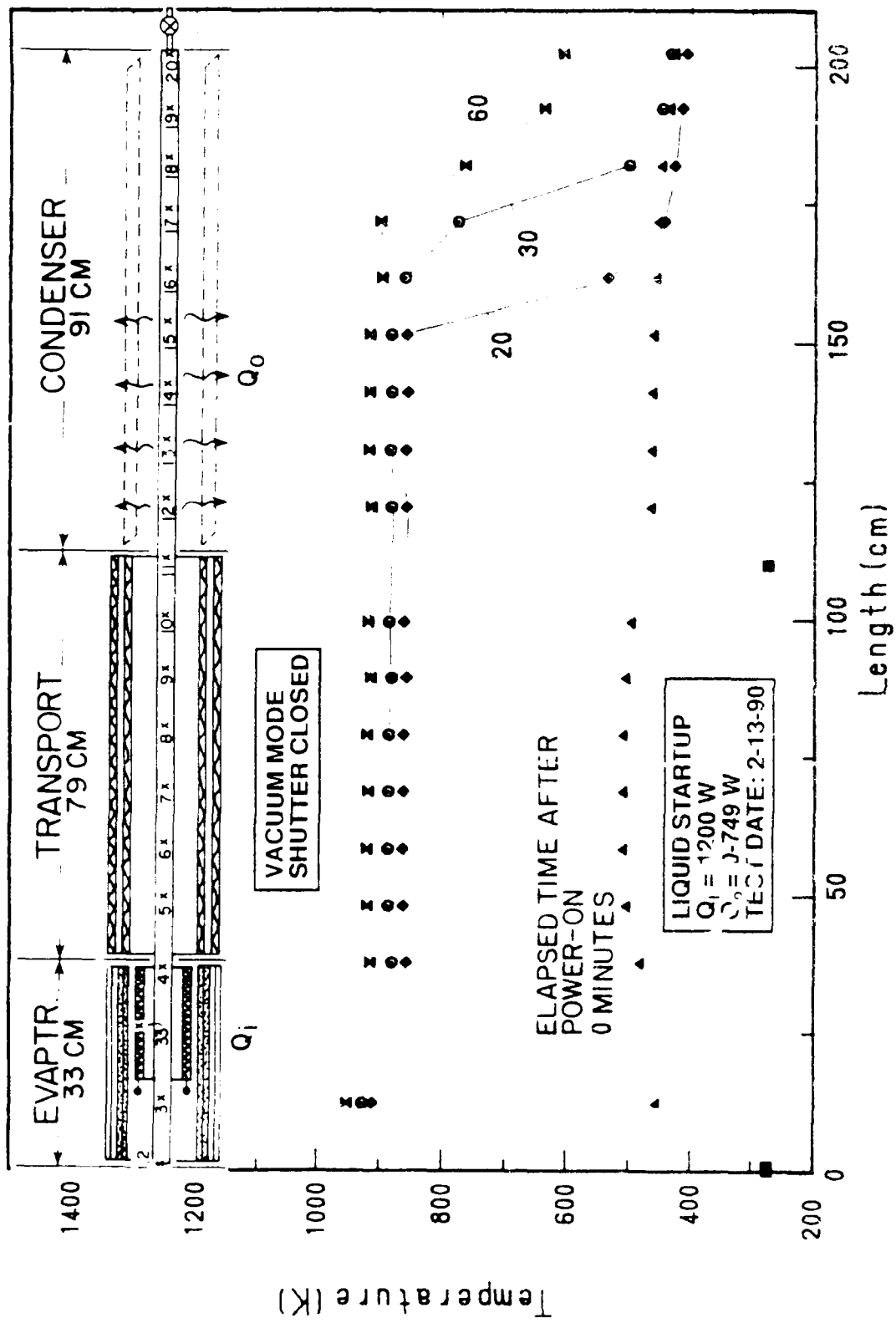


Figure 44. Axial Temperature Profile at Specified Time From 0-150 Minutes After Power Input ($Q_1 = 1200$ W; Vacuum Mode; Liquid Startup).

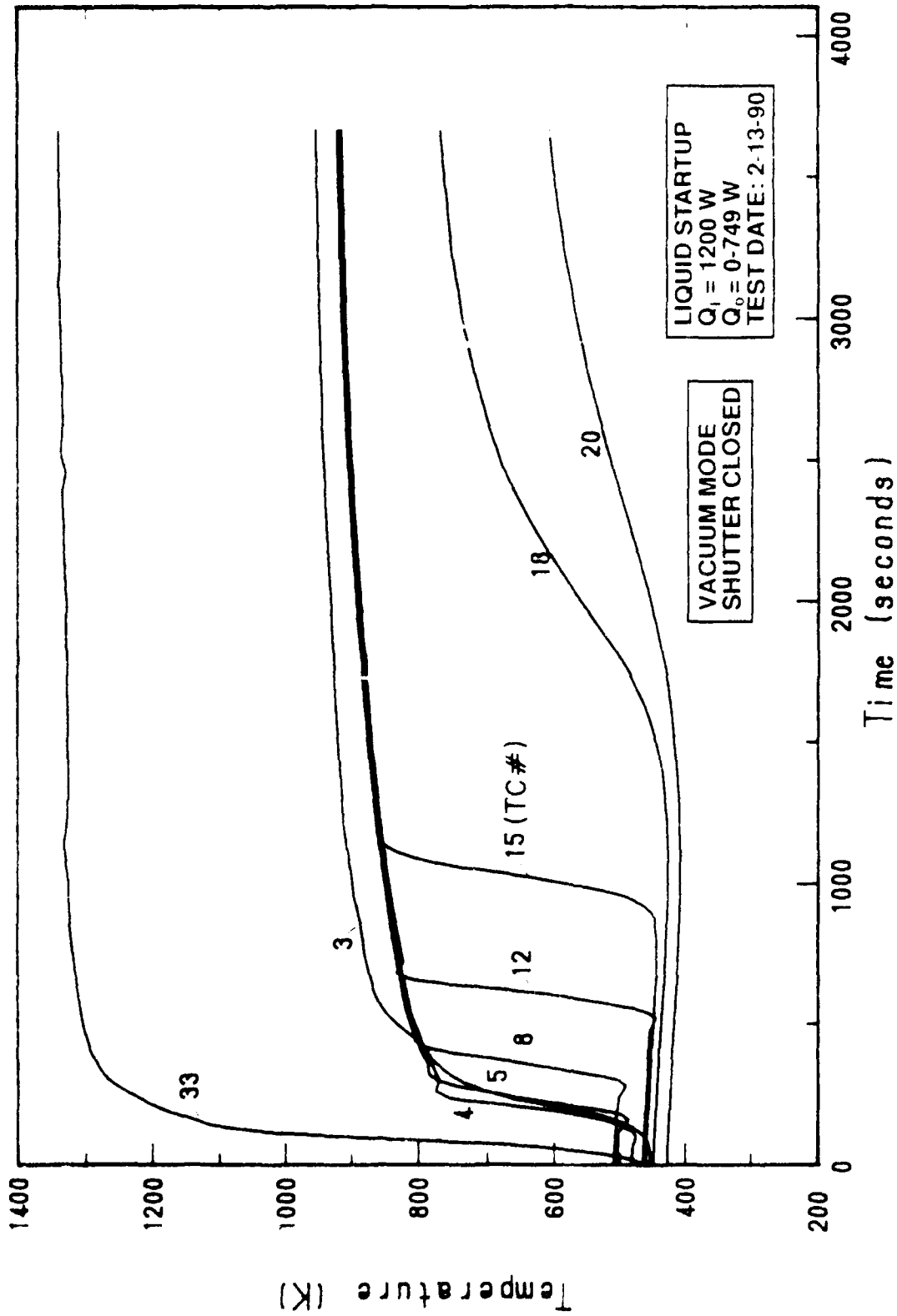


Figure 45. Transient Temperature Profile at Specified Axial Locations ($Q_i = 1200 \text{ W}$, Vacuum Mode; Liquid Startup).

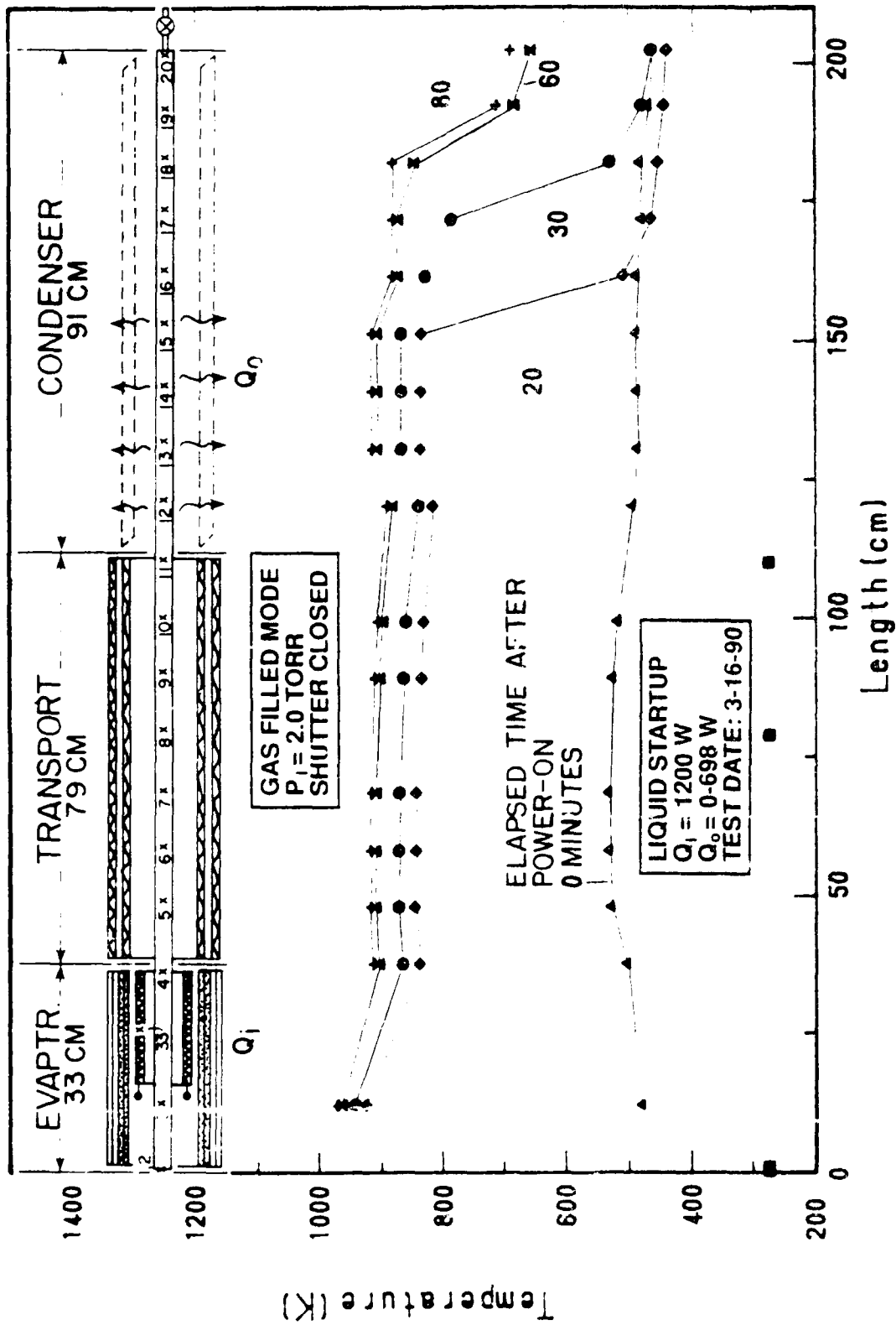


Figure 46. Axial Temperature Profile at Specified Time From 0-150 Minutes After Power Input ($Q_i = 1200$ W; Gas-Filled Mode; Liquid Startup).

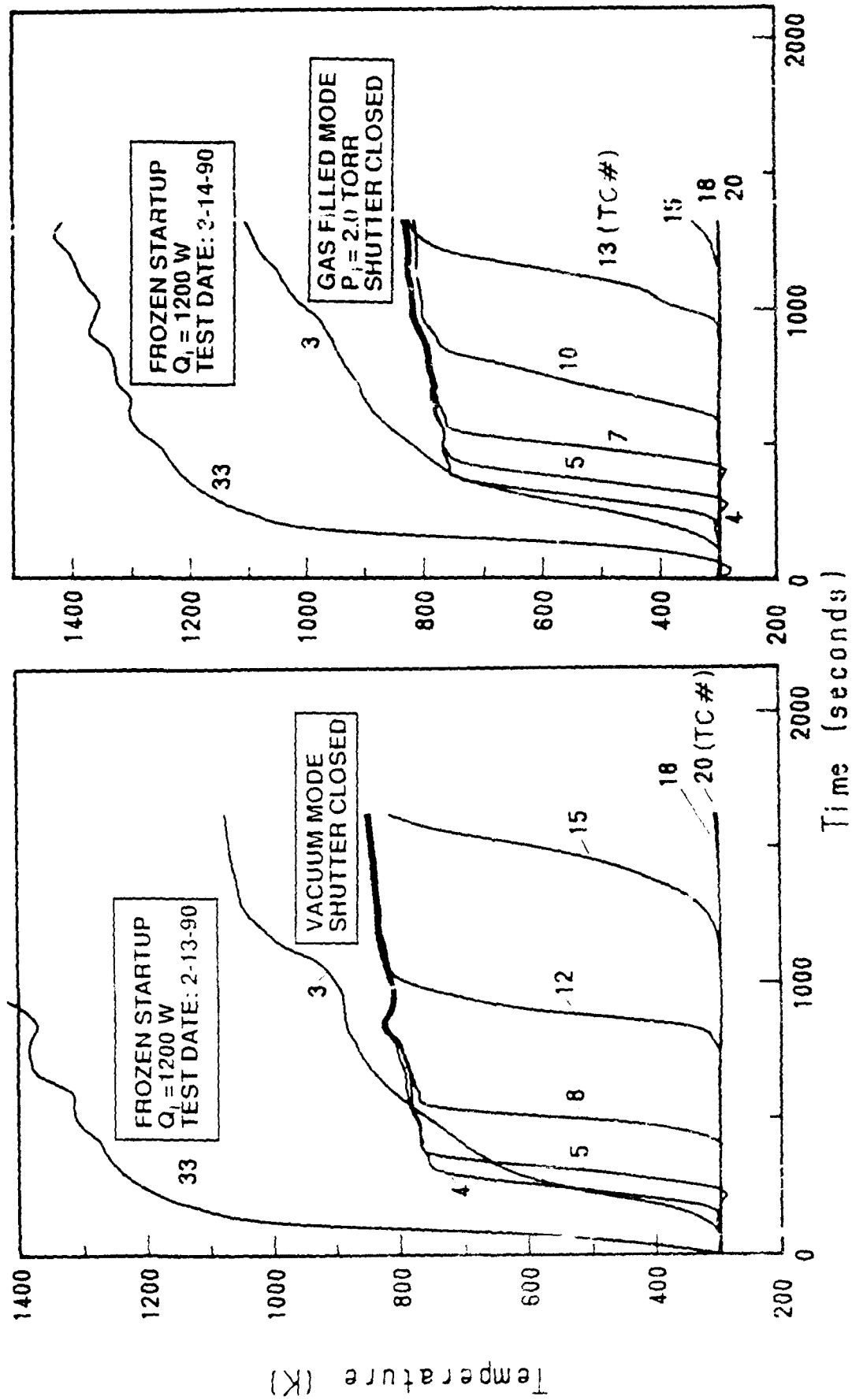


Figure 48. Evaporator and Heater Temperature "Run-Away" Condition During 1200-W Input (Vacuum and Gas-Fill'd Modes).

TABLE 4. Vacuum-Mode Steady-State Test Results

TEST DATE	HEAT INPUT, Q, [W]		Q _E		Q _A		Q _O		AVG OPERATING TEMP [°C] T.C.#8	HOT FRONT LOCATION		INACTIVE CONDENSER LENGTH [CM]
	MEASURED (SHUNT)	CALLORI-METER	[W]	% Q _i	[W]	% Q _i	[W]	% Q _i		T.C.#	L [CM]	
01-29-90	404	401	123	30.7	90	22.4	188	46.9	486	14	141	59
	501	482	134	27.8	90	19.7	253	52.5	502	16	161.6	38.4
	610	587	153	26.1	104	17.7	329	56.0	517	17	172	28
01-30-90	703	695	165	23.7	114	16.4	417	60.0	538	18	182	18
	811	809	183	22.6	130	16.1	495	61.2	557	19	192	8
01-31-90	899	894	197	22.0	142	15.9	556	62.2	579	19,20	197	3
	1005	1009	220	21.8	155	15.4	634	62.8	598	20	200	0
02-01-90	1105	1083	227	21.0	169	15.6	637	63.4	622	20	200	0
	1209	1185	248	20.9	188	15.5	749	63.2	638	20	260	0
02-02-90	1317	1288	264	20.5	206	16.0	818	63.5	661	20	200	0
	1406	1364	276	20.2	217	15.9	871	63.8	670	20	200	0
02-05-90	1504	1471	295	20.0	233	15.8	942	64.0	685	20	200	0
02-07-90	1604	1573	310	19.7	247	15.7	1014	64.5	697	20	200	0

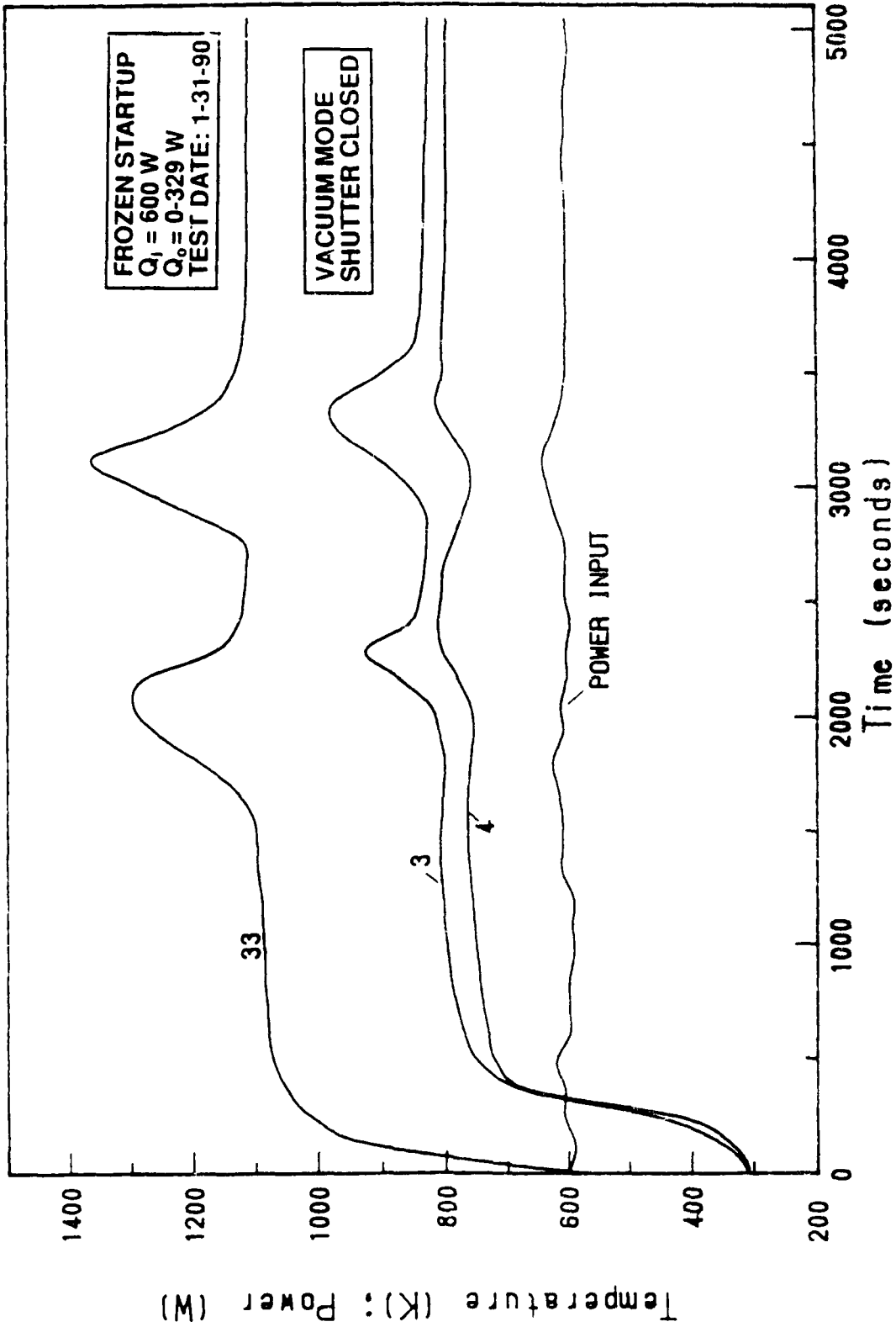


Figure 49. Transient Input Power and Evaporator Temperature Variations ($Q_1 = 600 \text{ W}$; Vacuum Mode).

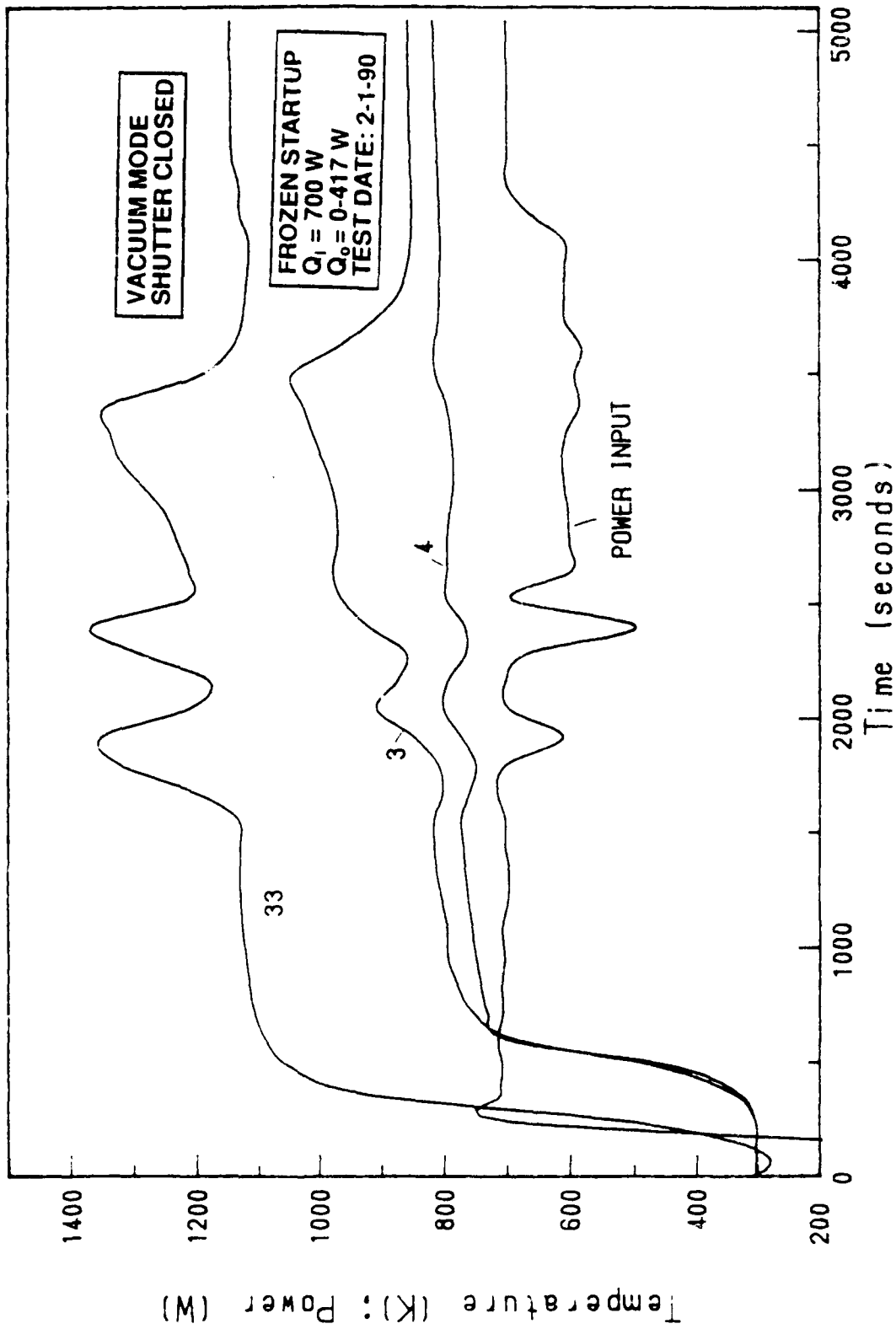


Figure 51. Transient Input Power and Evaporator Temperature Variations ($Q_1 = 700$ W; Vacuum Mode).

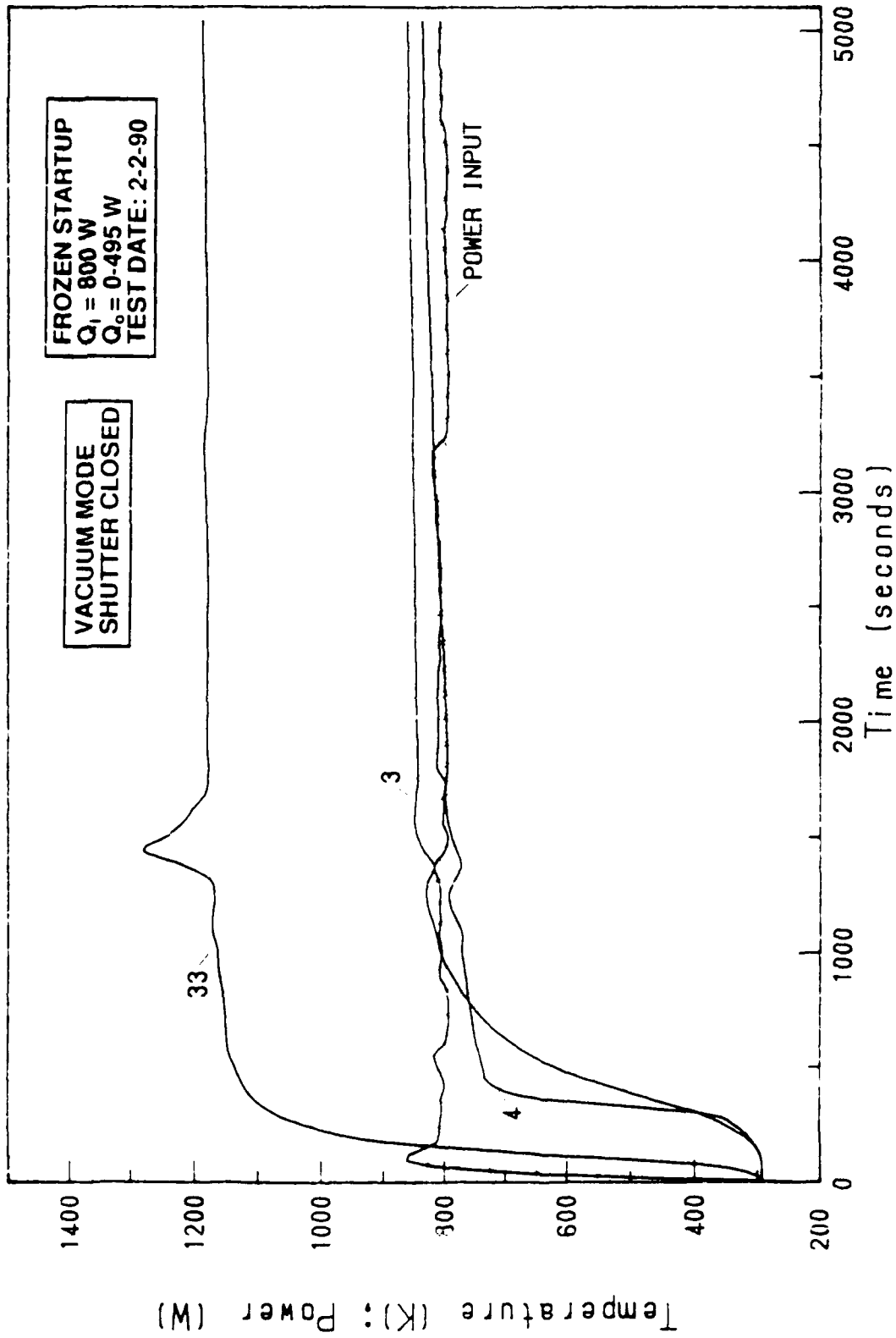


Figure 53. Transient Input Power and Evaporator Temperature Variations (Q_i = 800 W; Vacuum Mode).

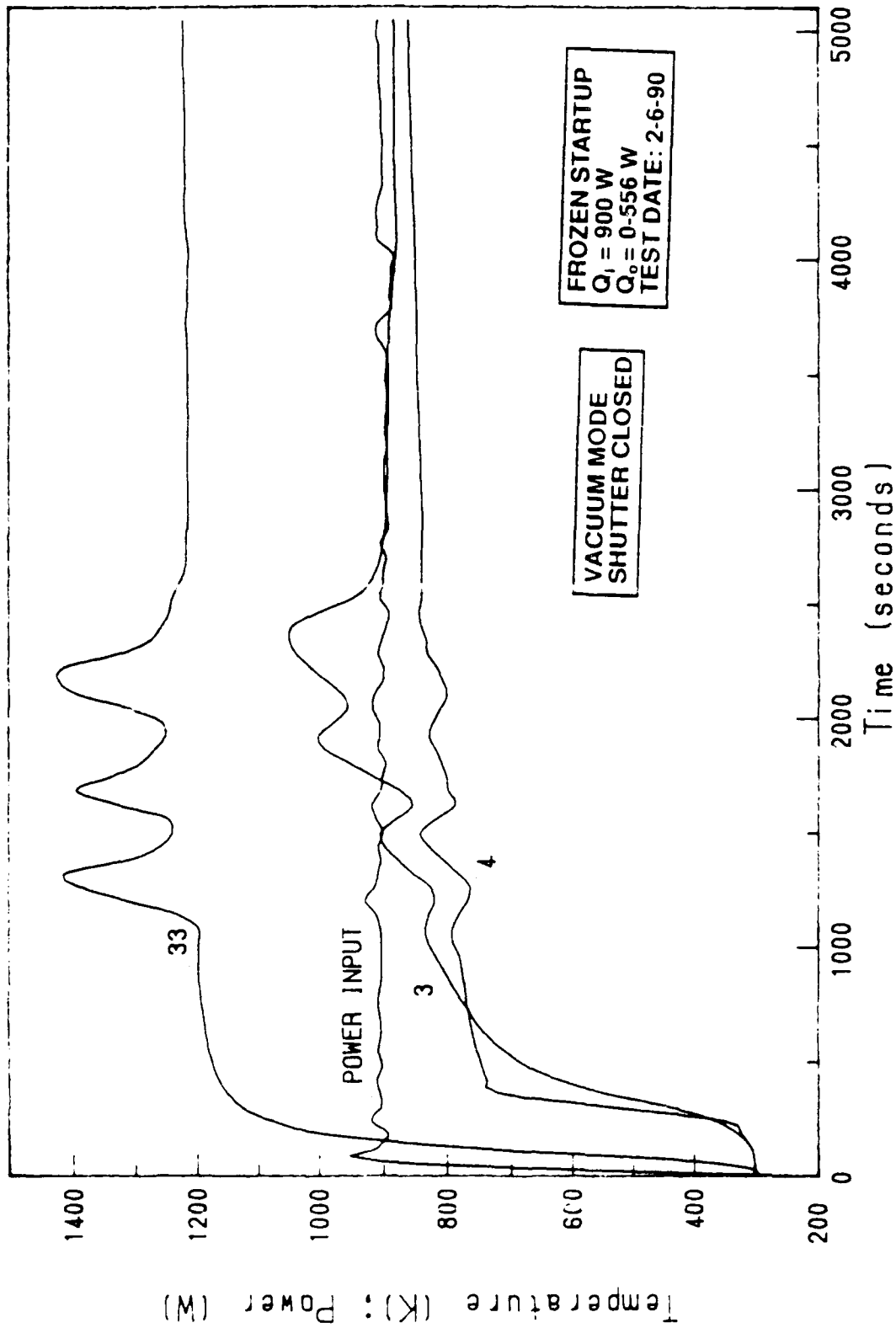


Figure 55. Transient Input Power and Evaporator Temperature Variations (Q₁ = 900 W; Vacuum Mode).

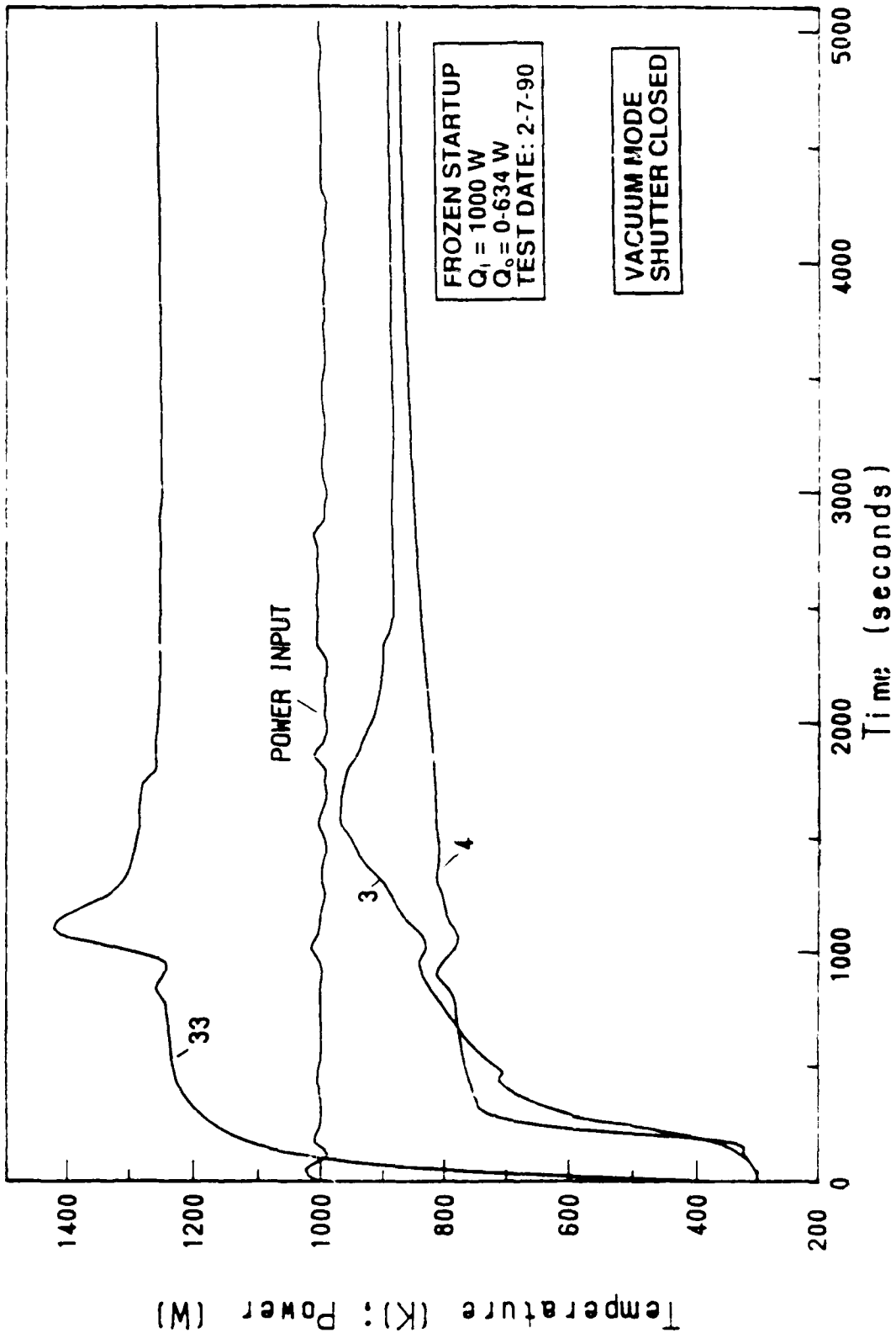


Figure 57. Transient Input Power and Evaporator Temperature Variations ($Q_i = 1000 \text{ W}$; Vacuum Mode).

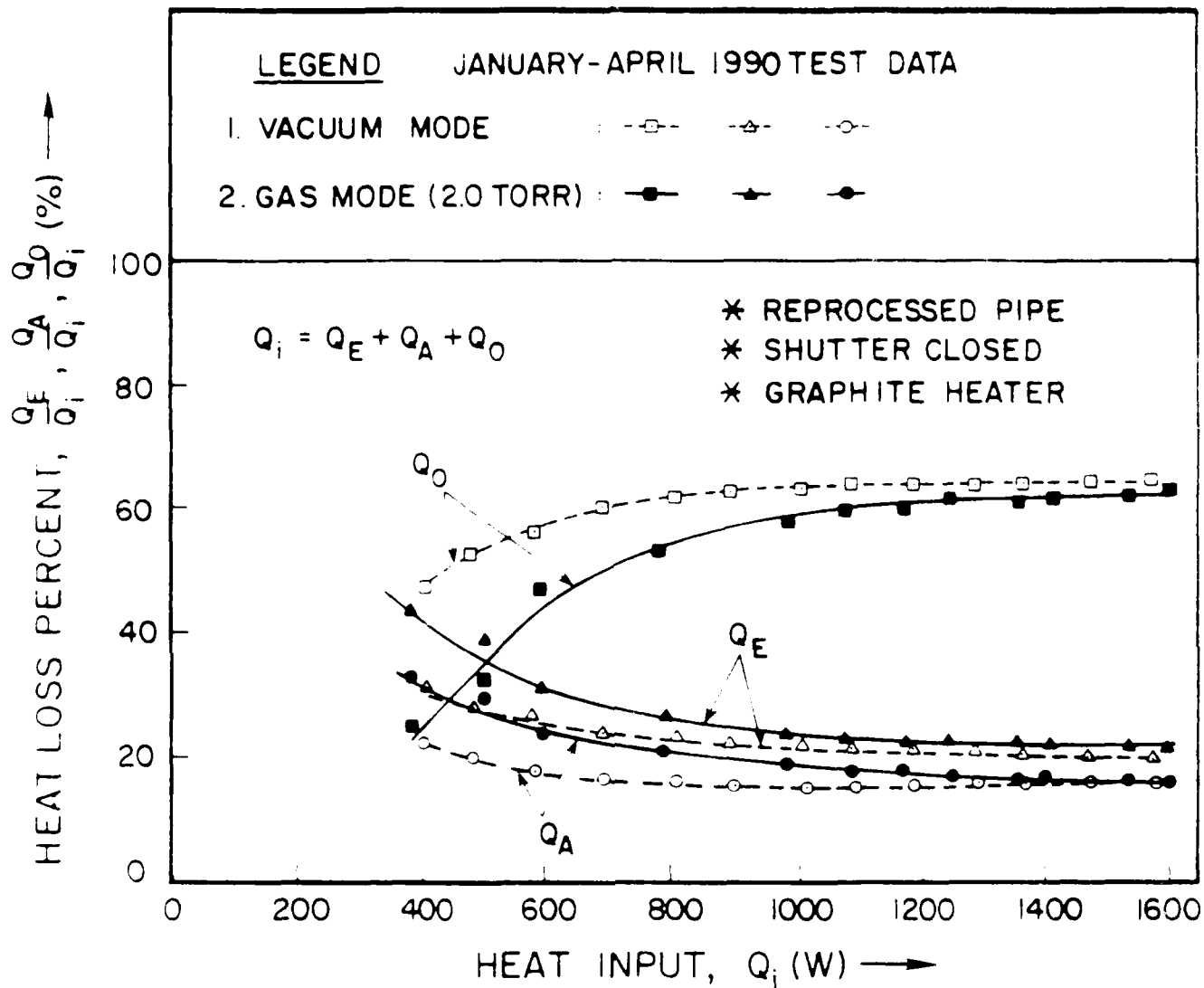


Figure 59. Steady-State Calorimetric Test Data.

TABLE 6. Steady-State Tilt Test Results (2.0 Torr Gas Filled Mode)

DATE	Q (Q _{in}) [W]	TILT [ARC DEG]	Q _i [W]	Q _A [W]	Q _o [W]	T _{in} [C]	ΔT _{in} T.C. #7 [C]	REMARKS		
15 MAR 90	1190 (1089)	0	241	185	663	643	54	No Dryout		
	1190 (1123)	0.5	254	192	677	645	59			
	1193 (1135)	-1.0	261	190	683	645	62			
	1201 (1147)	-1.5	272	194	681	644	65			
	1196 (1147)	-2.0	284	192	671	643	63			
22 MAR 90	1201 (1154)	0	294	225	636	677	58	At - 2.5" Heater Overtemperature, Test Shut Down		
	1197 (1150)	-2.0	303	223	624	679	66			
	1200	-2.5	-	-	-	650	108			
26 MAR 90	1209 (1143)	0	292	236	615	685	59	At - 3.0" Heater Overtemperature, Test Shut Down		
	1199 (1167)	-0.5	307	234	626	685	62			
	1204 (1166)	-1.0	309	241	617	686	65			
	1203 (1155)	-1.5	304	238	613	686	68			
	1200 (1159)	-2.0	313	236	610	686	69			
	1199 (1159)	-2.5	310	239	608	686	71			
	1195 (1161)	-2.75	317	239	605	686	72			
	1206	-3.0	-	-	-	657	114			
	16 MAR 90	1504 (1303)	0	309	227	857	682		66	At - 1.5" Heater Overtemperature, Test Shut Down
		1500 (1399)	-0.5	317	222	859	683		68	
1503 (1393)		1.0	315	222	857	683	71			
1505		-1.5	-	-	-	672	103			
21 MAR 90	1505 (1463)	0	332	241	891	688	68	At - 2.5" Heater Overtemperature, Test Shut Down		
	1505 (1457)	-0.5	332	241	884	688	71			
	1503 (1459)	-1.0	336	243	879	687	73			
	1505 (1452)	-1.5	338	241	873	686	76			
	1507 (1457)	-2.0	343	243	870	687	76			
	1510	-2.5	-	-	-	661	105			
	1709 (1624)	0	379	303	941	733	76			
27 MAR 90	1698 (1612)	-0.5	372	305	934	734	78	No Dryout		
	1701 (1619)	-1.0	372	313	934	734	79			
	1700 (1598)	-1.5	361	308	929	733	80			
	1695 (1608)	-1.75	372	312	924	732	81			
	1703 (1605)	-2.0	372	307	925	732	81			
	1701 (1606)	-2.25	371	314	920	731	82			
	1696 (1538)	-2.5	353	295	890	730	82			
	1711 (1570)	-2.75	360	304	906	730	82			
	1694 (1569)	-3.0	357	304	908	730	82			
	1707 (1571)	0	355	293	919	726	80			

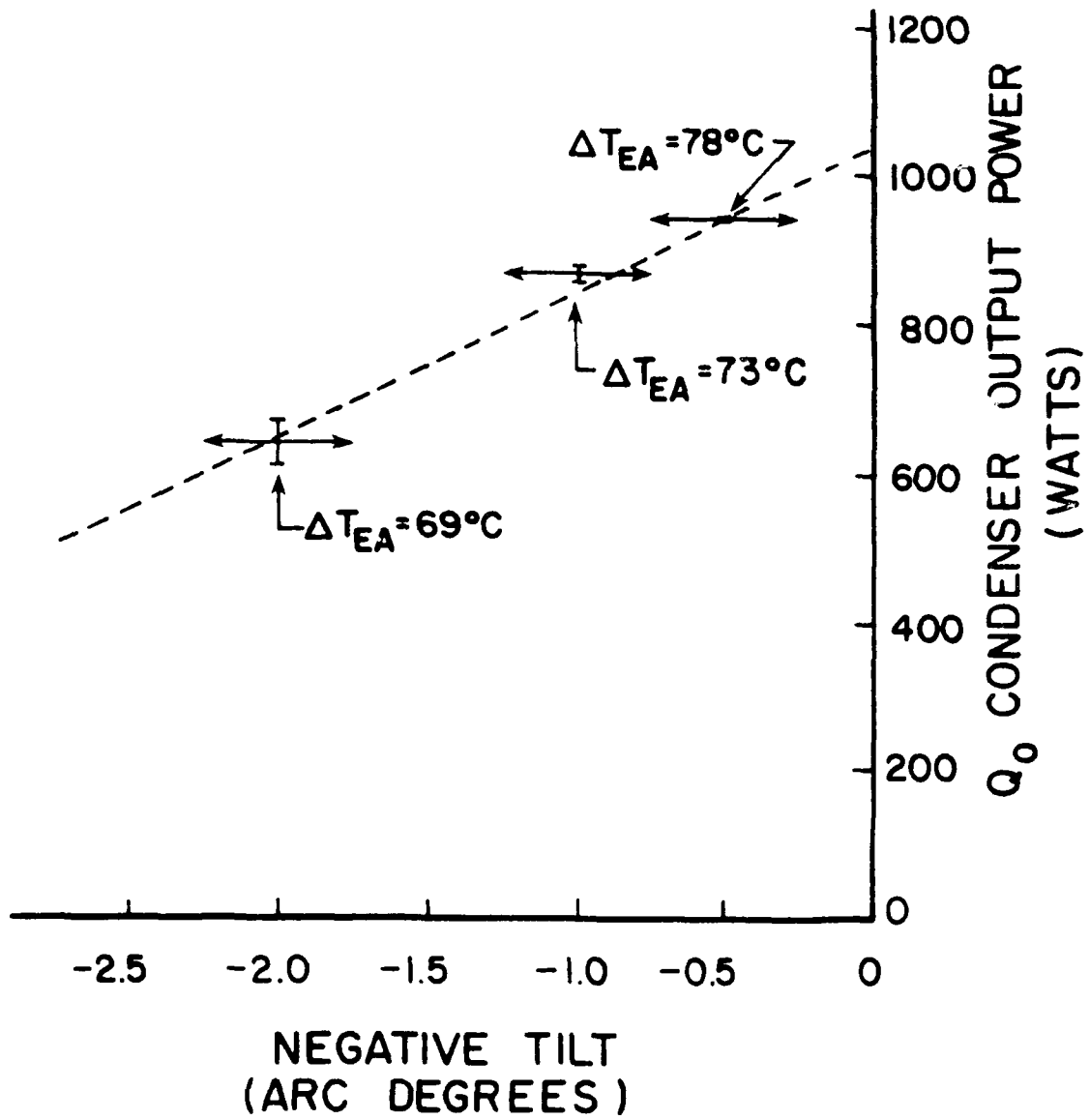


Figure 60. Adverse Tilt Test Results.

5. For the same transport capacity variation of 500-1000 W, the pipe operating temperature varied 130 K in vacuum mode and 90 K in gas mode.

6. The evaporator to adiabatic temperature difference dropped with increase in transported power for vacuum mode while it increased for the gas mode. The vacuum mode characterized the lean evaporator behavior of the double wick while the gas mode characterized the nucleate boiling phenomenon in an inert gas environment.

7. The frozen startup tests were smooth and successful in the gas-filled mode up to a transport of 640 W (Q_o) which is 35.5% of the designed transport capacity. For the vacuum mode, the frozen startups were rough and successful up to the same transport. However, the LMHP could not be started from frozen state for power inputs ≥ 1200 W in both modes.

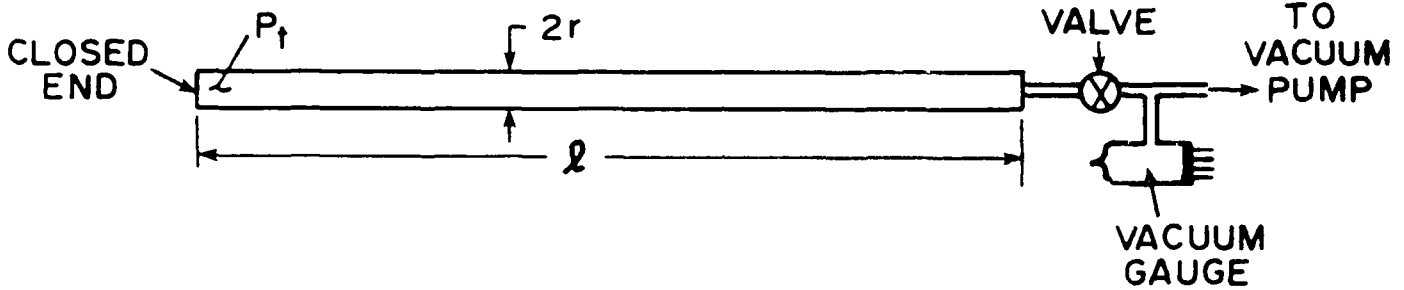
As a follow-up, the existing 2-m sodium heat pipe should be tested for gas generation by suitable mass spectroscopic measurements. Hydrogen permeation through the heat pipe wall during red-hot temperature tests is suspected. This should be quantitatively measured to explain the loss of vacuum in the heat pipe after a few performance tests.

8. Ponnappan, R., Beam, J.E., and Mahefkey, E.T., Performance Test Results of the 2m DWHP with Artery Priming Enhancement, Sixth International Heat Pipe Conference, Grenoble, France, May 25-28, 1987.
9. Ponnappan, R., M.L. Ramalingam, Beam, J.E., and Mahefkey, E.T., Remedial Measures for Condenser Quenching in a Long Water Heat Pipe, 22nd AIAA Thermophysics Conference, Honolulu, Hawaii, June 8-10, 1987.
10. Ponnappan, R., Ramalingam, M.L., Beam, J.E., and Mahefkey, E.T., Response of a Double Wall Artery Heat Pipe to Pulsed Heat Loads, International Symposium on Thermal Problems in Space Based Systems, December 13-18, 1987, Boston, MA. ASME-HTD-Vol. 83, Ed. F. Dobrau and M. Imber, pp. 55-62.
11. Ponnappan, R., Ramalingam, M.L., J.E. Johnson, and Mahefkey, E.T., Analysis of Evaporator Critical Heat Flux in the Double Wall Artery Heat Pipe, AIAA-88-0356. AIAA 26th Aerospace Sciences Meeting, Reno, Nevada, January 11-14, 1988.
12. Ponnappan, R. and Mahefkey, E.T., Development of a Double-Wall Artery High Capacity Heat Pipe, Spacecraft Thermal Control, Design, and Operation. Edited by P. E. Bauer and H. E. Collicott, Vol. 86, pp. 202-221.
13. Ponnappan, R., Beam, J.E., and Mahefkey, E.T., Improved Double Wall Artery High Capacity Heat Pipe, J. Spacecraft and Rockets, Vol. 22 No. 6, Nov-Dec. 1985 pp. 592-597.
14. Ponnappan, R., Ramalingam, M.L., Johnson, J.E., and Mahefkey, T., Evaporator Critical Heat Flux in the Double Wall Artery Heat Pipe, Experimental Thermal and Fluid Science, Int. J. of Experimental Heat Transfer, Thermodynamics and Fluid Mechanics, Vol.2, No.4, October 1989, pp. 450-464.

24. Ferrell, J.K., and Johnson, H.R., The Mechanism of Heat Transfer in the Evaporator Zone of the Heat Pipe, Presented at the ASME Space Technology and Heat Transfer Conference, Los Angeles, Paper No. 70-HT/SP T-12, 1970.
25. Ponnappan, R., Ramalingam, M.L., Beam, J.E., and Mahefkey, E.T., Remedial Measures for Condenser Quenching in a Long Water Heat Pipe, Presented at the AIAA, 22nd Thermophysics Conference, Honolulu, Paper No. AIAA-87-1546, 1987.
26. Ivanovskii, M.N., Sorokin, V.P., and Yagodkin, I.V., The Physical Principles of Heat Pipes, Translated by R. Berman and Girice, Clarendon Press, Oxford, 1982.
27. Brost, O., Groll, M., and Mack, H., Development of a High Temperature Furnace with Variable Conductance Heat Pipe, Proceedings of the 6th International Heat Pipe Conference, Grenoble, France, May 25-29, 1987, pp. 697-702.
28. Tolubinsky, V.I., Shevchek, E.N., and Kudritskaya, L.V., "Study of Vapor-Gas Front Temperature Characteristics in Sodium Coaxial Heat Pipes," Ibid, pp. 326-329.
29. Merrigan, M., Los Alamos National Laboratory. Private Communications.
30. Ponnappan, R., Boehman, L.I., and Mahefkey, E.T., Diffusion Controlled Startup of a Gas-Loaded Liquid Metal Heat Pipe, Paper No. 89-1707, AIAA 24th Thermophysics Conference, Buffalo, NY, June 12-14, 1989.
31. Ponnappan, R., Studies on the Startup Transients and Performance of a Gas Loaded Sodium Heat Pipe, Technical Report for Period June 1987 - November 1988. WRDC-TR-89-2046. U.S. Air Force, Wright-Patterson Air Force Base, OH, June 1989.

APPENDIX - A

Determination of the pressure at the closed end of a long tube when the other end is connected to a vacuum pump.



Pressure P_i at the closed end is given by the following equation. [Ref. Handbook of High Vacuum Engineering by H.A. Steinherz, Reinhold Publishing Corp. 1963.]

$$P_i = q \left[\frac{1}{s} (2\pi r l + \pi r^2) + \frac{3}{2V_a} \frac{l}{r} \left(1 + \frac{l}{r} \right) \right] \quad (1)$$

where,

- l = length of tube, cm
- r = radius of tube, cm
- P_i = pressure at closed end, torr
- q = outgassing rate, torr. cm³/sec.cm²
- V_a = arithmetic mean molecular velocity, cm/sec
- s = pumping speed of pump, cm³/sec

APPENDIX - B

High Temperature Heater Details

- Figure B.1 Heater Assembly over the Heat Pipe
 - Figure B.2 Heater Constructional Details
 - Figure B.3 Manufacturers' Specifications of the Heater
-
- Table B.1 Temperature vs Resistance Values

TUBULAR HEATER

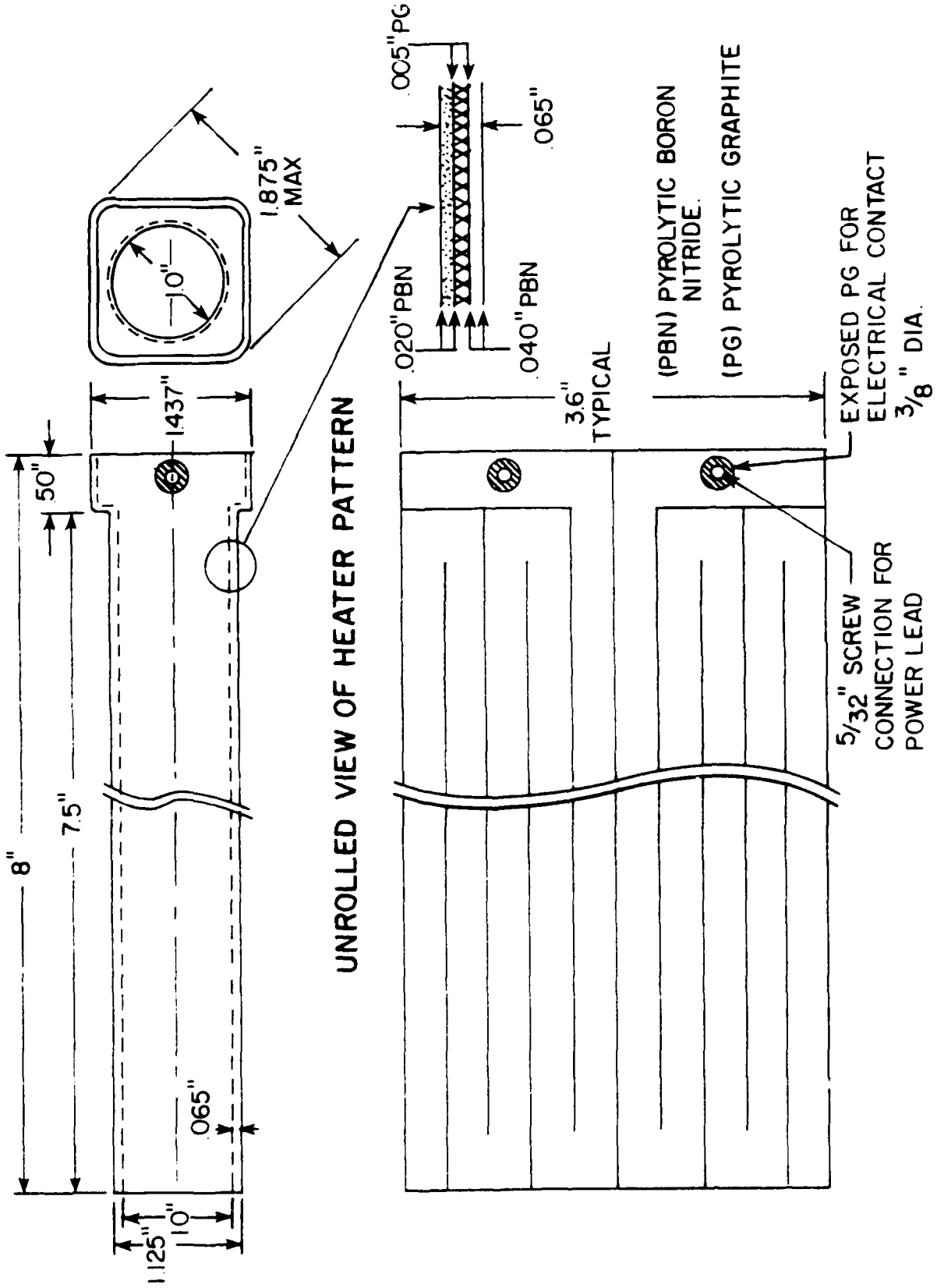


Figure B.2

TABLE B.1 Temperature vs Resistance Values for the Boralectric Heater

Temperature (°C)	Voltage (Volt)	Current (Amp)	Resistance (Ohm)	Remarks
25	—	—	55.1	Multimeter
748	109	3.7	29.5	Heat Pipe Test Circuit
837	131.9	4.62	28.5	
944	157.84	5.69	27.7	
1041	180.57	6.69	27.0	
1162	205.55	7.80	26.4	

APPENDIX - C

Zirconia Insulating Cylinders used in the Evaporator Heat Shield

ZIRCONIA INSULATING CYLINDERS

Suggested Applications

- Type ZYC Zirconia Cylinders are used in top and bottom loading resistance heated and induction furnaces. They are particularly suited for insulation in hot pressing, crystal growing and annealing furnaces.
- Zirconia Cylinders provide excellent insulation for pipes or molten metal transporting and feed tubes.
- Zirconia Cylinders are used as radiation shielding in vacuum furnaces, replacing five or six metal shields without loss of insulation value. In processes where carbon contamination cannot be tolerated, ZIRCAR products are used instead of graphite felts and carbon black as insulation.
- Zirconia Cylinders, as well as other ZIRCAR flexible and rigid insulating products, find use in a variety of research and development high temperature applications.

Sizes Available

Inside Diameter: 1" to 12" in 1" increments
Wall Thickness: 1/2"
Length: 6", 12" and 20"
Tolerances: $\pm 1/16"$ I.D. and O.D.

be made. Larger cylinders may be made in sections with lap joints on special order. All cylinders are machined on the outside surface with tolerances of $\pm .030"$ possible.

Non-standard sizes are available by special request.

Wall thicknesses as thin as 1/4" or as thick as 1 1/2" can

Special shapes can also be manufactured including curved boards, or troughs, truncated cones, rectangular sleeves, and oblong tubes.

APPENDIX - D

```

program gas
real lb,ncg
dimension t(10),pv(10),ta(10)
do 30 ifile=11,16
read(ifile,*) qin,qout,pi
read(ifile,*) (t(i),i=1,10)
do 10 i=1,10
ta(i)=t(i)+273.16
tsq=ta(i)**.5
td=5567.0/ta(i)
coff=2.29e+11
td=coff/(10.**td)
pv(i)=td/tsq
10 continue

av=1.2667e-4
lb=10.3e-2
ru=8.3143
c av -- area of vapor core (m**2)
c lb -- distance between condenser thermocouples (m)
c ru -- universal gas constant (J/g mole K)

const=av*lb/ru
sum=0.0
do 20 j=1,10
pvd=(pv(1)-pv(j))/ta(j)
sum=sum+pvd
20 continue

ncg=sum*const
c ncg -- noncondensable gas in gram moles

caseno=ifile-10
write(3,*) ' case number ',caseno
write(3,*)
write(3,*) '      Qin          Qout          PI'
write(3,*) qin,qout,pi
write(3,*)
write(3,*) ' T input : '
write(3,*) t
write(3,*)
write(3,*)
write(3,11) qin,qout,pi
11 format(/,3x,' power input          =',f15.5,' Watts',
1      /,3x,' power output          =',f15.5,' Watts',
2      /,3x,' ncg initial pressure =',f15.5,' Torr',/)

write(3,21) ncg
21 format(/,3x,' noncondensable gas   =',e12.6,' g moles',/)

30 continue
stop
end

```